High-Spin Spectroscopy of Octupole Structures in Radon and Radium Isotopes Using Multinucleon Transfer Reactions

Thesis submitted in accordance with the requirements of the University of Liverpool for the degree of Doctor in Philosophy, by

James Francis Charles Cocks

Oliver Lodge Laboratory Liverpool

October 1996

This thesis is dedicated to my Mom and Dad

ABSTRACT

Octupole-deformed nuclei in the light-actinide mass region have been populated using multinucleon transfer reactions involving thick ^{232}Th targets and heavy-ion beams. Yield measurements for nuclei populated in the reactions ^{56}Fe + ^{232}Th, ^{86}Kr + ^{232}Th and ^{136}Xe + ^{232}Th indicate that the transfer of nucleons by deep-inelastic processes is dictated by mass and charge equilibration. The population distributions also suggest that ^{136}Xe is the most effective of the three projectiles for populating octupole-deformed nuclei in the light-actinide region.

The ^{136}Xe + ^{232}Th reaction was repeated in order to study radon (A = 218, 220, 222) and radium (A = 222, 224, 226) isotopes. In these nuclei, interleaving bands of opposite parity have been observed to high angular momenta ($I \geq 20\hbar$). Strong alignment effects are observed in the radon isotopes. No such effects are observed in the radium isotopes, nor indeed in previously-studied isotopes of radium and thorium in this region. The value of $|D_0/Q_0|$ measured for the radium isotopes remains constant with angular momentum. This suggests that the reflection-asymmetric charge distribution is not affected appreciably by rotation for these isotopes. A very small value of $|D_0/Q_0|$ has been observed for ^{224}Ra throughout the measured range.

ACKNOWLEDGEMENTS

I would like to thank Professor P. J. Twin for allowing me to pursue this research at the University of Liverpool. I would also like to express my gratitude to
Dr. P. A. Butler for providing me with such an interesting research project and for his supervision and support during the last three years. Thanks also go to Dr. G. D. Jones for his assistance during this work.
I would like to thank everyone at the University of Jyväskylä, and particularly Professor R. Julin, for making us feel so welcome on our trips to Finland. I'd also like to acknowledge everyone who helped set-up and run the experiments.
Many thanks to everyone at the Institute of Nuclear Physics at Kraków for their hospitality during May 1995, and particularly Professor R. Broda and Dr. B. Fornal for their extensive help and advice.
I'd like to thank Dr. J. F. Smith for his help and advice during the last three years. Thanks also to Dr. P. M. Jones for all his help with computer problems.
I would like to thank the computer support staff at Liverpool and particularly Janet Sampson for her assistance with data translation. Thanks also to Dr. D. M. Cullen and Duncan Appelbe for additional help with computing.
Many thanks to Dr. D. M. Cullen, Dr. A. T. Semple and Dr. E. S. Paul for proof-reading parts of this work, and to Dr. J. F. Smith and Kev Cann for proof-reading all of it.
Thanks go to Mr. A. Gent and Mr. I. Grainger for their help and enthusiasm.
Finally, I'd like to thank Martin Smith, Roger Allatt, Kev Cann, Paul Greenlees and everyone else who tried to play football during the last three years.

Contents

INTRODUCTION

The region of the nuclear chart which has shown the best evidence for octupole instability in the nuclear ground state is around $Z = 88-90$ and $N \approx 134$ [Butler 96], [Ahmad 93], [Nazarewicz 84]. These nuclei have low-lying negative parity states and relatively strong $B(E1)$ values for the transitions between the bands of opposite parity; for the single case of ^{226}Ra large $B(E3)$ values have been measured consistent with its interpretation as a rotating pear shape [Wollersheim 93]. The inaccessibility of these nuclei has, however, meant that there are large gaps in our knowledge of octupole effects in heavy nuclei. Complete measurements of the high-spin behaviour of the yrast octupole band only exist for the isotopes of thorium. For the radium isotopes such measurements are only available for ^{218,220}Ra and ^{226}Ra; there is only a limited amount of data on ^{224}Ra and virtually no information exists for ^{222}Ra. The scarce data do, however, suggest cancellation effects for the electric dipole moment for ^{224}Ra [Poynter 89a] which does not occur in the thorium isotopes. This effect is not properly established as the spin-dependent behaviour for ^{222}Ra has not yet been measured. There are almost no data on the octupole structures for the radon isotopes. The motivation for the systematic measurement of the octupole bands in these lower-Z nuclei is that particle alignment effects may be revealed which are not observed for the higher-Z systems, across a wide range of neutron number. This observation would give an indication to the strength of the octupole interaction between the different orbitals occupied by the neutron and the proton, as it has been established that alignment effects are washed out by strong octupole coupling.

This provided the necessary motivation for this work. Here, a new method for studying high-spin states in octupole-deformed light-actinides is presented, whereby multinucleon transfer reactions are used involving heavy-ion beams and thick ^{232}Th targets. Initially, three heavy-ion reactions were performed using arrays of twelve germanium detectors to collect gamma-ray coincidence data. These were ^{56}Fe + ^{232}Th, ^{86}Kr + ^{232}Th and ^{136}Xe + ^{232}Th. Production yield values extracted for the three reactions indicated that the population of light-actinide nuclei by deep-inelastic transfer

is dictated by mass and charge equilibration processes. The population distributions also revealed that the ^{136}Xe + ^{232}Th reaction would provide the best opportunity for accessing high-spin states in nuclei such as ^{222}Ra, ^{220}Rn and ^{222}Rn. These experiments, analyses and results are described in chapter 5. The ^{136}Xe + ^{232}Th reaction was repeated using the GAMMASPHERE array. The acquired statistics enabled the study of previously-unknown high-spin states in ^{218,220,222}Rn and ^{222,224,226}Ra. Chapter 6 concentrates on this experiment and its results and conclusions. The earlier chapters provide an introduction to some of the theory and techniques used in this work. Chapter 1 highlights some nuclear models which have been used, with a leaning towards the physics of octupole shapes. The shell model has been successful in describing nuclear properties, particularly near closed shells. Away from closed shells, the coherence of single-particle effects can lead to collective effects therefore the influence of nuclear deformation on the single-particle orbits must be investigated. The Nilsson model, which is described in chapter 1, can be used study the effect of deformation on the single-particle orbitals. The model can also be used to calculate the total potential energy of a nucleus and thus predict the existence of stable deformed shapes. Centrifugal and Coriolis forces, which act when the nucleus rotates, also perturb the single-particle orbitals. The cranked shell model can be used to calculate these effects. This model is also described in the first chapter. Chapter 2 concerns the origins of octupole deformation and outlines some of the spectroscopic features which are characteristic of an octupole-deformed nucleus. A map of octupole-deformed light-actinide nuclei is also given in this chapter. Chapter 3 begins with an outline of the different types of heavy-ion interaction and then describes the important features of deep-inelastic reactions. Chapter 4 is devoted to gamma-ray spectroscopy, covering topics such as gamma-ray interactions, detection techniques, large arrays of germanium detectors and data-analysis methods.

Chapter 1

Introductory Theory

1.1 Deformation Parameters

The surface of a non-spherical nucleus can be parameterised in terms of a spherical harmonic expansion [Bohr 52], [Hill 53]. This is written as

$$R = R(\theta, \phi) = c(\alpha) R_0 \left[1 + \sum_{\lambda=2}^{\lambda_{max}} \sum_{\mu=-\lambda}^{\lambda} \alpha_{\lambda\mu} Y^*_{\lambda\mu}(\theta, \phi) \right] \tag{1.1}$$

where $R(\theta, \phi)$ is a radius vector, R_0 ($=r_0 A^{1/3}$) is the radius of a sphere having the same volume as the nucleus, $Y_{\lambda\mu}(\theta, \phi)$ are spherical harmonics and $\alpha_{\lambda\mu}$ are their corresponding expansion coefficients. The parameter $c(\alpha)$ is determined from the volume-conservation condition. For axially-symmetric shapes, the $\alpha_{\lambda\mu}$ coefficients with $\mu \neq 0$ vanish. The remaining parameters $\alpha_{\lambda 0}$ are usually called β_λ and are used to quantify nuclear deformation.

Quadrupole deformation, represented by the parameter β_2, describes a reflection-symmetric, spheroidal shape and is dominant in most nuclei. A nucleus which has a non-zero β_3 parameter is *octupole deformed* and takes on a *reflection-asymmetric* shape.

1.2 Nuclear Rotation

Rotations of a spherical nucleus about an axis of symmetry are quantum-mechanically indistinguishable, but in deformed nuclei rotation becomes a possible mode of excitation. A deformed nucleus can generate angular momentum by collective motion (rotation), in which all the nucleons rotate collectively about an axis perpendicular to the symmetry axis (called the rotation axis), and by the alignment of the intrinsic angular momenta of individual nucleons with the rotation axis. The total angular momentum of a rotating axially-deformed nucleus, $\vec{I}$, can be written as

$$\vec{I} = \vec{R} + \vec{J} \tag{1.2}$$

where $\vec{R}$ is the angular momentum generated by the collective motion of the core and $\vec{J}$ is the sum of the intrinsic angular momenta of the unpaired valence nucleons. This is illustrated schematically in figure 1.1. As the collective rotational angular

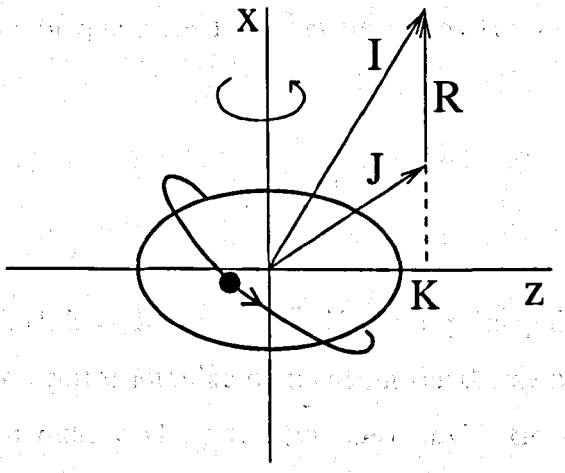

Figure 1.1: A schematic representation of angular momentum coupling. The x-axis is the axis of rotation and the z-axis is the symmetry axis.

momentum, $\vec{R}$, is perpendicular to the symmetry axis, the projection of $\vec{I}$ and $\vec{J}$ onto the symmetry axis is the same, and is denoted by K. The projection onto the symmetry axis of the intrinsic angular momentum of a single valence nucleon, $\vec{j}$, is known as Ω. That is, $\vec{J} = \sum_i \vec{j}_i$ and $K = \sum_i \Omega_i$.

1.3 The Nilsson Model

The Nilsson model can be used to calculate the effect which a deformed nuclear potential has on single-particle orbits. The Nilsson single-particle Hamiltonian is based on a harmonic-oscillator potential and includes a strong spin-orbit ($\vec{l}.\vec{s}$) force and an $\vec{l}^2 - \langle l^2 \rangle_N$ term which simulates the flattening of the potential at the centre of the nucleus. The Hamiltonian is written as

$$H_{nil} = \frac{-\hbar^2}{2m} \nabla^2 + V_{osc} - 2\kappa\hbar\omega_0[\vec{l}.\vec{s} - \mu(l^2 - \langle l^2 \rangle_N)] \tag{1.3}$$

where κ and μ are constants which determine the strengths of the spin-orbit and $l^2 - \langle l^2 \rangle_N$ terms. The oscillator potential can be written as

$$V_{osc} = \frac{m}{2}(\omega_x^2 x^2 + \omega_y^2 y^2 + \omega_z^2 z^2) \tag{1.4}$$

where ω_x, ω_y and ω_z are one-dimensional oscillator frequencies in Cartesian coordinates. The following set of quantum numbers describes the orbitals in the Nilsson model:

$$\Omega^\pi[Nn_z\Lambda] \tag{1.5}$$

where Ω is the projection of the single-particle angular momentum on the symmetry axis, π is the parity which is equal to $(-1)^N$, N is the principal quantum number, Λ is the projection of the orbital angular momentum on the symmetry axis and n_z is the number of oscillator quanta along the symmetry axis. Hence, $\Omega = \Lambda + \Sigma$ where $\Sigma(\pm\frac{1}{2})$ is the projection of the intrinsic spin of the nucleon on the symmetry axis.

When deformation is introduced, each (2j+1)-fold degenerate j-state is split into j+$\frac{1}{2}$ two-fold degenerate levels. This can be seen in the Nilsson diagram for neutrons with N=82–126 which is shown in figure 1.2. The Pauli principle forbids any two levels having the same quantum numbers (N, Ω and π) to cross. One may observe that levels labelled with the same N, Ω and π do not cross but interact. The interaction causes a change in the trajectories of these orbitals. The nuclear force is attractive so an orbital

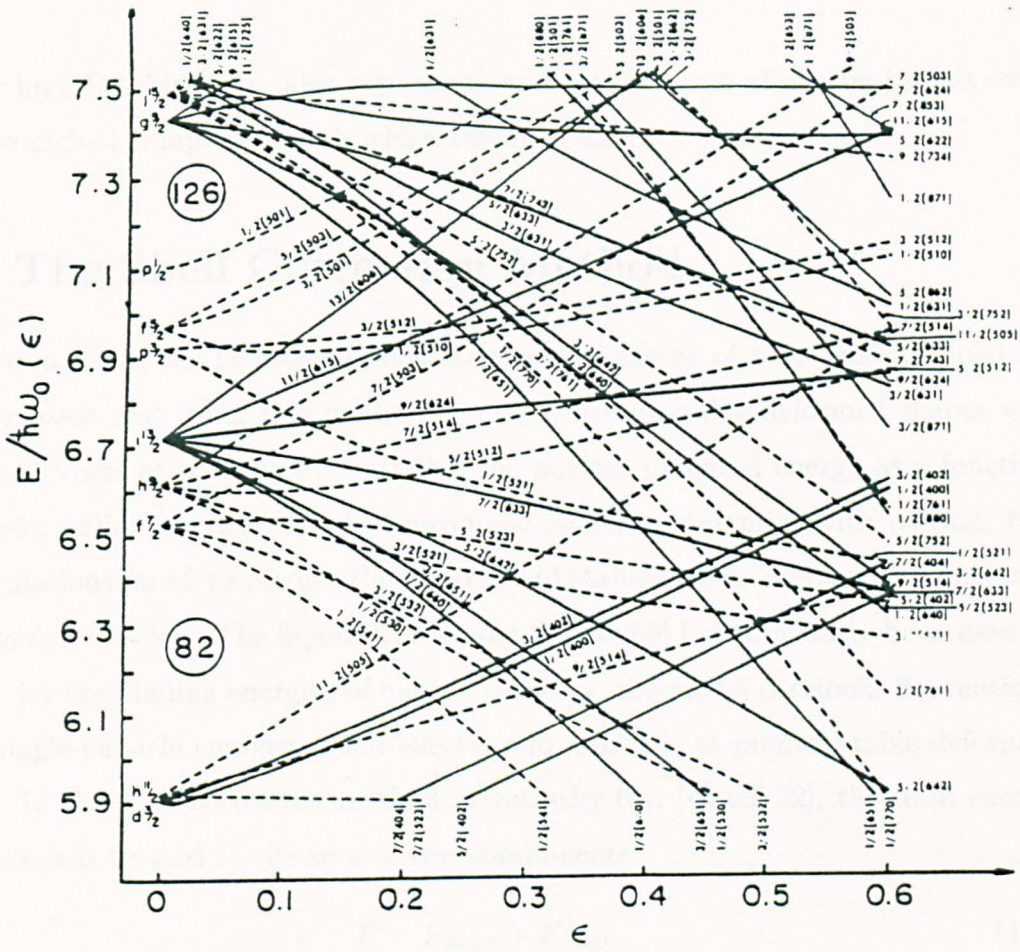

Figure 1.2: Nilsson diagram for neutrons, N=82–126. Solid lines represent positive parity states and dashed lines represent negative parity states. The deformation parameter $\epsilon \approx 0.95\beta$. Taken from [Casten 90].

which lies close to the core nuclear matter will have a lower energy than one which lies further away. The result is that in a nucleus with prolate deformation, orbitals with low-Ω values have lower energies than those with high-Ω values. Also, high-Ω orbitals have smaller values of n_z therefore orbitals with small n_z values have higher energies. This means that as one moves to larger prolate deformations the high-Ω, low-n_z orbitals slope upwards and the low-Ω, high-n_z orbitals slope downwards. The negative-parity orbitals such as $i_{13/2}$ are lowered by the strong spin-orbit interaction into the region of positive-parity orbitals. As the interaction of states of opposite parity is not allowed, the trajectories of these levels are unperturbed. The trajectories

of many high-Ω orbitals are also very straight due to the lack of nearby j-shells with the same high-Ω component with which they can mix.

1.4 The Shell Correction Method

The Nilsson model can be used to calculate the total energy of a nucleus as a function of deformation and using this method the existence of stable deformed shapes was predicted. Vogel *et al.* [Vogel 68] studied the nuclear potential energy as a function of β_3 deformation using a modified harmonic-oscillator potential with pairing, but the calculations failed to predict the existence of stable nuclear shapes with non-zero octupole deformation. The liquid-drop model [Myers 69] has previously been used to account for the binding energies of nuclei. However, the model overlooks fluctuations in the single-particle energies (shell effects) and also fails to predict stable deformed shapes. In the shell correction method [Strutinsky 67], [Brack 72], the total energy of a nucleus is treated as the sum of two components:

$$E = E_{macr} + E_{shell} \tag{1.6}$$

where E_{macr} is the macroscopic energy, which is smoothly dependent upon the number of nucleons, and E_{shell} is the shell-correction term which fluctuates with particle number. The macroscopic part is determined using the liquid-drop model and the shell-correction term is calculated using the deformed independent-particle model. Moller and Nix [Möller 81] used calculations based on the folded-Yukawa deformed potential to deduce the shell-correction and a Yukawa-plus-exponential macroscopic energy which is more sensitive to higher-order deformations than the liquid-drop model. These predicted the existence of stable shapes with ground state octupole instability. Nazarewicz *et al.* [Nazarewicz 84] applied a similar model using a Woods-Saxon potential to analyse medium mass and heavy nuclei. The octupole deformation energy curves for even-even isotopes of radon, radium, thorium and uranium which were obtained in reference [Nazarewicz 84] are shown in figure 1.3. Several radon and radium isotopes which are the focus of this thesis are expected to be octupole

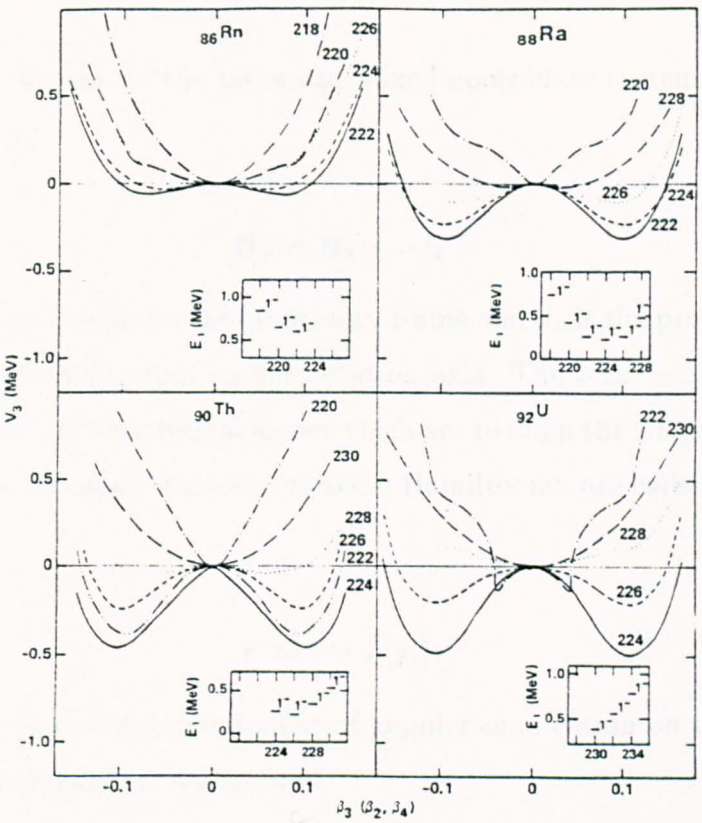

Figure 1.3: The octupole deformation energy curves for even-even isotopes of radon, radium, thorium and uranium obtained using the shell-correction method with a Woods-Saxon potential. The insets are the experimental energies of the lowest 1^- states in these isotopes. Taken from [Nazarewicz 84].

deformed. The calculations predict that ^{222}Ra possesses the largest octupole deformation of the radium isotopes, and ^{222}Rn of the radon isotopes.

1.5 The Cranked Shell Model

The cranked shell model [Inglis 54], [Inglis 56] describes the effect of rotation upon the single-particle nuclear states. More specifically, the model provides a way of studying the effect of Coriolis and centrifugal forces on these orbitals. The model uses a body-fixed coordinate system which has a fixed orientation with respect to the nuclear potential. The coordinate system is rotated (or "cranked") at a rotational

frequency ω with respect to the laboratory-fixed coordinate system. The cranking Hamiltonian is

$$H_\omega = H_0 - \omega J_x \tag{1.7}$$

where H_0 is the Hamiltonian in the laboratory frame and J_x is the projection operator of the total angular momentum on the rotation axis. The term $-\omega J_x$ describes the effect of the Coriolis and centrifugal forces which act to align the single-particle orbits. The eigenvalues of the single-particle cranking Hamiltonian are called Routhians and are defined as

$$e' = e - \omega\langle j_x\rangle. \tag{1.8}$$

The expectation value of the component of angular momentum on the rotation axis is called the aligned angular momentum,

$$i_x = \langle j_x\rangle = -\frac{de'}{d\omega}. \tag{1.9}$$

Hence, if the Routhian is plotted as a function of rotational frequency, $\hbar\omega$, the negative slope of the Routhian gives the amount of aligned spin i_x. The Nilsson quantum numbers are no longer valid under rotation and in a reflection-symmetric nucleus the single-particle Routhians are labelled with parity π and signature α. In a reflection-asymmetric nucleus the Routhians are labelled with the simplex quantum number. The simplex operator is discussed in the next chapter.

Pairing and Quasiparticles

There is a large body of experimental evidence supporting the existence of pairing correlations in nuclei. Examples of such evidence are:

- All known even-even nuclei have ground state spins of $0\hbar$ suggesting that the nucleons are in time-reversed orbits and their angular momenta cancel out;

- The ground-state spins of odd-A nuclei are determined by the spin of the last (unpaired) nucleon;
- The energy spacing between the ground state and the first non-rotational excited state is consistently above 1 MeV in even-even nuclei, while the spacing is much smaller in odd-A nuclei;
- The moments of inertia measured for rotating nuclei are approximately 30% of the rigid-body value [Bardeen 57].

Paired nucleons in time-reversed orbits interact (collide) twice per orbit and subsequently scatter into different time-reversed orbits. This means that a state near the Fermi surface may or may not be occupied and the surface is no longer sharply-defined. In the vicinity of the smeared Fermi surface it is appropriate to discuss the population of excited states in terms of particle and hole occupation probabilities. Here it is useful to introduce the concept of *quasiparticles.* Quasiparticles are linear combinations of particle and hole wavefunctions. They describe a state in terms of the probability of being occupied by a particle, V_j, and the probability that is it not, U_j (or, equivalently, that is it occupied by a hole). Far below the Fermi surface all states are occupied, $V_j = 1$ and $U_j = 0$. As one approaches the Fermi surface the probabilities become mixed.

The cranking Hamiltonian can be modified to accommodate pairing interactions. The resultant Hamiltonian is called the cranked Hartree-Fock-Bogolyubov Hamiltonian [Bengtsson 85],

$$H = H_0 - \omega J_x - \Delta(P^+ - P) - \lambda N. \tag{1.10}$$

The parameter Δ is known as the pair-gap parameter and is half the energy required to break a pair of nucleons in an even-even nucleus. The parameters P^+ and P are the quasiparticle creation and annihilation operators and the λN term keeps the number of nucleons in the system constant. In the course of this work, quasiparticle Routhians have been calculated with an axially-deformed Woods-Saxon potential [Dudek 79] us-

ing the computer code WSBETA [Ćwiok 87]. In order to determine the Woods-Saxon potential six parameters for protons and neutrons are required. These are:

- Depth of the central potential, V;
- Radius parameter of the central potential, r_0;
- Diffuseness parameter of the central potential, a;
- Strength of the spin-orbit potential, λ;
- Radius parameter of the spin-orbit potential, $(r_0)_{so}$;
- Diffuseness parameter of the spin-orbit potential, a_{so}.

The depth of the central potential is given as

$$V = V_0[1 \pm \kappa(N - Z)/(N + Z)] \tag{1.11}$$

with the plus sign for protons and the minus sign for neutrons. The quantities V_0 and κ are constants which vary for different parameter sets. The "universal" parameter set was optimised using the high-spin spectra of ^{204}Pb and ^{212}Ra [Dudek 81]. This parameter set, listed in table 1.1, was used for the calculations described later in this work. The deformation parameters of the nucleus to be studied must also be input in the WSBETA code.

Particles	V_0 (MeV)	κ	r_0 (fm)	a (fm)	λ	$(r_0)_{so}$	a_{so}
Neutrons	−49.6	0.86	1.347	0.70	36.0	1.30	0.70
Protons	−49.6	0.86	1.275	0.70	36.0	1.30	0.70

Table 1.1: The parameters of the "universal" Woods-Saxon potential.

The results of Routhian calculations for some of the nuclei whose properties addressed in this work can be found in section 6.6.2.

Alignment effects

As the nucleus rotates, the Coriolis and centrifugal forces compete with the pairing force. The forces act in different directions on the paired nucleons acting to break the pair. When the pair is broken the angular momenta of the individual nucleons add constructively to the total angular momentum of the nucleus. Figure 1.4 shows an example of a quasiproton Routhian plot for ^{218}Ra. The plot was obtained using a deformed Woods-Saxon potential with "universal" parameterisation and is taken from reference [Nazarewicz 87]. In the vacuum configuration, or ground state of the nucleus, the levels with negative energy are occupied. As one rotates the nucleus (increases the rotational frequency) the angular momentum increases until the aligned configuration is reached at $\hbar\omega \approx 0.18$ MeV. The lowest-lying Routhian slopes downwards and has a minimum at $\hbar\omega \approx 0.18$ MeV. The process of pair-breaking in nuclei is known as *quasiparticle alignment* and rotational bands may be built on aligned configurations.

Observing Alignments In Experimental Data

In classical mechanics the rotational frequency is defined as

$$\omega = \frac{dE}{dI} \tag{1.12}$$

where E is the total energy of the body and I is its angular momentum. The quantum-mechanical analogue of this expression is

$$\hbar\omega = \frac{dE}{d\sqrt{I(I+1)}} = \frac{E_I - E_{I-2}}{\sqrt{I(I+1)} - \sqrt{(I-2)(I-1)}}. \tag{1.13}$$

For a rotational band of stretched E2 transitions at $I \gg 1$ the rotational frequency is

$$\hbar\omega \approx \frac{E_\gamma}{2} \tag{1.14}$$

where E_γ is the energy of a gamma-ray transition. The aligned angular momentum on the axis of rotation is given as

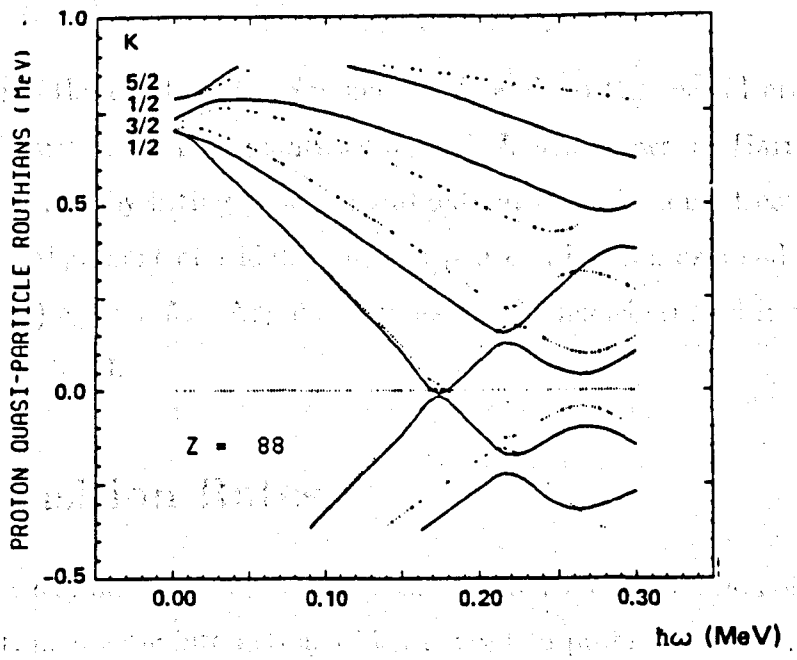

Figure 1.4: Proton quasiparticle plot as a function of rotational frequency. The deformation parameters used correspond to the yrast configuration of ^{218}Ra. States of positive simplex are represented by solid lines and dashed lines label states of negative simplex. Taken from reference [Nazarewicz 87].

$$I_x = \sqrt{I(I+1) - K^2}, \tag{1.15}$$

and for a K=0 rotational band this can be written as

$$I_x(I_a) = I_a + \frac{1}{2} \tag{1.16}$$

where I_a is the average spin of the initial and final states.

In order to probe the alignment properties of quasiparticles in nuclear systems the component of I_x attributed to the rotation of the nuclear core must be subtracted. The aligned angular momentum of the valence nucleons can be written as

$$i(\omega) = I_x(I_a) - I_{rot}(\omega) \tag{1.17}$$

where $I_{rot}(\omega)$ is the rotational component of I_x and, to the second order, $I_{rot}(\omega) = J_0\omega + J_1\omega^3$ [Harris 65]. The quantities J_0 and J_1 are known as Harris parameters and can be deduced by fitting experimental data at low rotational frequencies, where $i(\omega) = 0$. The alignment of a high-j nucleon pair can be seen as a sudden increment in a plot of $i(\omega)$ against $\hbar\omega$. Alignment plots for the nuclei studied in this thesis are given in section 6.5.3.

1.6 Transition Rates

The strong nuclear interaction establishes the distribution and motion of nucleons, but it is the electromagnetic interaction which is used to probe the nucleus. The charge and current distributions in the nucleus are described by the electric and magnetic multipole moments, respectively [Blatt 52], [Davydov 65], [De Shalit 74], [Ring 80].

1.6.1 Single-Particle Transition Rates

Simple estimates for gamma-ray emission probabilities can be obtained if the transition is assumed to be due to a single proton changing from one shell-model state to another. They can be written as [Ring 80], [Krane 88]

$$\lambda(EL) \cong \frac{8\pi(L+1)}{L[(2L+1)!!]^2}\frac{e^2}{4\pi\epsilon_0\hbar c}\left(\frac{E}{\hbar c}\right)^{2L+1}\left(\frac{3}{L+3}\right)^2 cR^{2L} \tag{1.18}$$

and

$$\lambda(ML) \cong \frac{8\pi(L+1)}{L[(2L+1)!!]^2}\frac{e^2}{4\pi\epsilon_0\hbar c}\left(\mu_p - \frac{1}{L+1}\right)^2\left(\frac{\hbar}{m_p c}\right)^2\left(\frac{E}{\hbar c}\right)^{2L+1}\left(\frac{3}{L+2}\right)^2 cR^{2L-2}. \tag{1.19}$$

The quantities $\lambda(EL)$ and $\lambda(ML)$ are the electric and magnetic transition rates, respectively. The multipolarity of the radiation is given the quantity L, E is the gamma-ray energy in MeV, μ_p is the magnetic moment of the proton and m_p is the

mass of the proton. By setting $R=r_0A^{1/3}$ in equation 1.18 one can obtain the following estimates for some of the lower order electric multipoles:

$$\lambda(E1) = 1.0 \times 10^{14}A^{2/3}E^3$$
$$\lambda(E2) = 7.3 \times 10^{7}A^{4/3}E^5$$
$$\lambda(E3) = 34A^2E^7$$
$$\lambda(E4) = 1.1 \times 10^{-5}A^{8/3}E^9$$

where λ is in s^{-1} and E is in MeV. The $(\mu_p - \frac{1}{L+1})^2$ term in equation 1.19 is usually replaced by 10, which gives the following estimates for the magnetic multipoles:

$$\lambda(M1) = 5.6 \times 10^{13}E^3$$
$$\lambda(M2) = 3.5 \times 10^{7}A^{2/3}E^5$$
$$\lambda(M3) = 16A^{4/3}E^7$$
$$\lambda(M4) = 4.5 \times 10^{-6}A^2E^9.$$

These estimates of the transition rates are known as *Weisskopf estimates.* They are not exact, but provide a relative comparison of transition rates.

1.6.2 Collective Transition Rates

Electric and magnetic transition probabilities have been calculated in terms of rotating multipoles by Bohr and Mottelson [Bohr 75]. For $E1$ and $E2$ transitions these are

$$B(E1; I_i \rightarrow I_f) = \frac{3}{4\pi}e^2D_0^2 < I_iK_i10|I_fK_f >^2 \tag{1.20}$$

and

$$B(E2; I_i \rightarrow I_f) = \frac{5}{16\pi}e^2Q_0^2 < I_iK_i20|I_fK_f >^2 \tag{1.21}$$

where K is the projection of the total nuclear angular momentum on the symmetry axis, D_0 is the intrinsic electric dipole moment and Q_0 is the intrinsic electric quadrupole moment. The $B(EL)$ and $B(ML)$ values are reduced transition probabilities which are given by the reduced matrix elements:

$$B(EL; I_i \rightarrow I_f) = \frac{1}{2I_i + 1} | < f \| \hat{Q}_L \| i > |^2 \quad . \tag{1.22}$$

and

$$B(ML; I_i \rightarrow I_f) = \frac{1}{2I_i + 1} | < f \| \hat{M}_L \| i > |^2. \tag{1.23}$$

Expressions for the transition probabilities in terms of the $B(ML)$ and $B(EL)$ values are given below [Ring 80]:

$\lambda(\mathrm{E1}) = 1.59 \times 10^{15}\ \mathrm{B(E1)E^3}$
$\lambda(\mathrm{E2}) = 1.22 \times 10^{9}\ \mathrm{B(E2)E^5}$
$\lambda(\mathrm{E3}) = 5.67 \times 10^{2}\ \mathrm{B(E3)E^7}$
$\lambda(\mathrm{E4}) = 1.69 \times 10^{-4}\ \mathrm{B(E4)E^9}$

and

$\lambda(\mathrm{M1}) = 1.76 \times 10^{13}\ \mathrm{B(M1)E^3}$
$\lambda(\mathrm{M2}) = 1.35 \times 10^{7}\ \mathrm{B(M2)E^5}$
$\lambda(\mathrm{M3}) = 6.28\ \mathrm{B(M3)E^7}$
$\lambda(\mathrm{M4}) = 1.87 \times 10^{-6}\ \mathrm{B(M4)E^9}.$

The transition rates λ(EL) and λ(ML) are expressed in s^{-1}. The units of $B(EL)$ and $B(ML)$ are $(\mathrm{e}^2(\mathrm{fm})^{2L})$ and $(\mu_N^2(\mathrm{fm})^{2L-2})$ respectively. The energies are in MeV. The $E1$ and $E2$ transition rates can be written as

$$\lambda(E1) = \frac{\lambda(total)}{I_{total}} I_{E1} \tag{1.24}$$

and

$$\lambda(E2) = \frac{\lambda(total)}{I_{total}} I_{E2} \tag{1.25}$$

where I_{E1} and I_{E2} are the intensities of the $E1$ and $E2$ gamma-ray transitions respectively, $\lambda(total)$ is the total transition rate and I_{total} is the total intensity of the depopulating transitions. Using equations 1.24 and 1.25 and the expressions for $\lambda(E1)$ and $\lambda(E2)$ in terms of $B(E1)$ and $B(E2)$, one obtains

$$\frac{B(E1)}{B(E2)} = 7.70 \times 10^{-7} \frac{E_{E2}^5}{E_{E1}^3} \frac{I_{E1}}{I_{E2}} \tag{1.26}$$

where E_{E1} and E_{E2} are the energies of the $E1$ and $E2$ transitions and $B(E1)/B(E2)$ is in fm^{-2}. Dividing equation 1.20 by equation 1.21 gives

$$\frac{B(E1; I_i \rightarrow I_f)}{B(E2; I_i \rightarrow I_f)} = \frac{12}{5} \left(\frac{< I_i K_i 10 | (I_i - 1) K_f >}{< I_i K_i 20 | (I_i - 2) K_f >} \right)^2 \left(\frac{D_0}{Q_0} \right)^2 . \tag{1.27}$$

For transitions with $K_i = K_f = 0$ this is equivalent to

$$\frac{B(E1; I_i \rightarrow I_f)}{B(E2; I_i \rightarrow I_f)} = \frac{16}{5} \frac{(2I_i - 1)}{(2I_i - 2)} \left(\frac{D_0}{Q_0} \right)^2 . \tag{1.28}$$

1.7 Selection Rules

When gamma rays are emitted following transitions between excited states in a nucleus, the recoil momentum imparted to the nucleus is negligible. This means that the energy of the emitted gamma ray corresponds to the difference in energy of the excited states. That is,

$$E_\gamma = E_i - E_f \tag{1.29}$$

where E_i and E_f are the energies of the initial and final states respectively. There are some *selection rules* for transitions between excited states. The angular momentum selection rule states that

$$|I_i - I_f| \leq L \leq (I_i + I_f) \qquad \forall \;\; L \neq 0 \tag{1.30}$$

where L is the multipolarity of the emitted gamma ray and I_i and I_f are the angular momenta of the initial and final states respectively. A multipolarity of 0 is forbidden because the photon has an intrinsic spin of 1. If the gamma ray carries an amount of angular momentum that is equal to the difference in angular momenta of the initial and final states then the transition is said to be *stretched.* The parity selection rule states that

$$\pi_i \pi_f = \pi_L \tag{1.31}$$

where π_i, π_f and π_L are the parities of the initial state, final state and the gamma ray, respectively. Even-multipole electric and odd-multipole magnetic transitions have π_L=+1 and odd-multipole electric and even-multipole magnetic transitions have π_L=−1. That is, M1, E2, M3 and E4 transitions have π_L=+1 and E1, M2, E3 and M4 transitions have π_L=−1.

Chapter 2

Reflection-Asymmetric Nuclei

2.1 The Origins of Octupole Deformation

Figure 2.1 shows the sequence of single-particle levels for a modified harmonic-oscillator potential for a spherical nucleus. Octupole correlations arise when states with $\Delta j = \Delta l = 3$ lie close enough to interact [Ahmad 93], [Butler 96]. This occurs when a subshell (l, j) is lowered into the shell below by the $\vec{l}^2$ and $\vec{l}.\vec{s}$ terms and, as a result, is in close proximity with a normal-parity subshell $(l-3, j-3)$. Pairs of $\Delta j = \Delta l = 3$ orbitals lie just above all the major shell gaps, thus the tendency for octupole deformation occurs just above closed shells. Nuclei which have their neutron and proton Fermi surfaces close to these 'octupole-driving' states are most susceptible to octupole deformation. These nuclei have N or Z close to 34 (interaction between $g_{9/2}$ and $p_{3/2}$), 56 ($h_{11/2}$ and $d_{5/2}$), 90 ($i_{13/2}$ and $f_{7/2}$) or 134 ($j_{15/2}$ and $g_{9/2}$). The largest octupole interactions exist in nuclei which have both N and Z close to one of these values. Also, the interacting states are closer together for larger particle numbers (for example, the $j_{15/2}$ and $g_{9/2}$ states are closer than the $i_{13/2}$ and $f_{7/2}$ states) so the heaviest nuclei have the largest octupole correlations. For these reasons, the light-actinide nucleus $^{224}_{90}\mathrm{Th}_{134}$ is predicted to have the largest octupole deformation and neighbouring nuclei will therefore exhibit strong octupole effects [Sheline 87]. Nuclei with similar values of N and Z to $^{146}_{56}\mathrm{Ba}_{90}$ are also susceptible to octupole deformation

and weaker effects are also expected in nuclei such as $^{112}_{54}Xe_{58}$ and $^{96}_{40}Zr_{56}$.

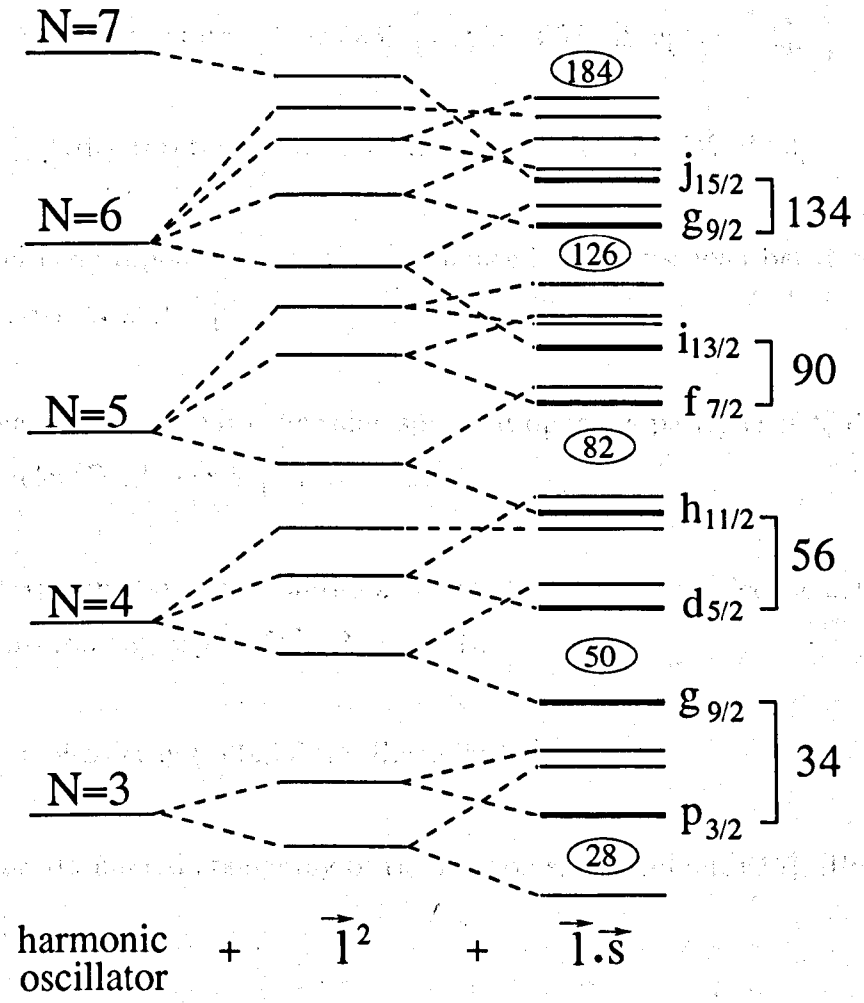

Figure 2.1: Energy level sequence for a modified harmonic-oscillator potential. High-j subshells are lowered into the shell below by the $\vec{l}^2$ and $\vec{l}.\vec{s}$ terms of the modified potential. Pairs of orbitals with $\Delta j = \Delta l = 3$ are shown, as are the nucleon numbers which give rise to strongest octupole correlations.

2.2 Spectroscopic Characteristics

There is a large body of experimental evidence supporting reflection asymmetry in nuclei. Nuclei which possess these shapes and symmetries display the following spectroscopic features:

- Low-lying 1^- and 3^- states [Asaro 53], [Stephens 54], [Stephens 55];
- Alternating-parity rotational bands [Fernández-Niello 82], [Ward 83];
- Intrinsic electric dipole moments and enhanced E1 transitions between positive- and negative-parity states [Butler 91];
- Near-degenerate states with the same spin and opposite parity (*parity doublets*) in odd-mass nuclei [Dahlinger 88], [Hughes 90];
- Large B(E3) transition probabilities associated with intrinsic electric octupole moments [Rohoziński 88], [Spear 90], [Raman 91];
- Enhanced alpha-decay probabilities [Leander 84];
- Inverted or attenuated staggering of the isotope shift [Aufmuth 87], [Borchers 87], [Ahmad 88].

The first three features are discussed in this section. The other characteristics are of less importance in the context of this work.

2.2.1 Low-lying 1^- and 3^- states

Low-lying, collective 1^- and 3^- states were first identified in radium and thorium isotopes with N $\approx$ 136 in the 1950s using alpha spectroscopy [Asaro 53], [Stephens 54], [Stephens 55]. The insets in figure 1.3 show that the minimum energies of the negative parity states in radon, radium, thorium and uranium isotopes are very localised in N. These minima lie close to the octupole deformation energy minima. The systematic behaviour of the 1^- and 3^- states in nuclei with $152 \leq A \leq 190$ and the heavy actinides was first described in terms of an octupole-vibrational model [Neergård 70], but this model did not work as well for nuclei in the light-actinide region where the octupole correlations are stronger [Neergård 70a], [Neergård 70b]. As a result, several theoretical models have been developed for nuclei that may be octupole-deformed rather than octupole-vibrational. A comprehensive review of the theoretical approaches to octupole deformation is given in reference [Butler 96].

2.2.2 Alternating-Parity Rotational Bands

A reflection-symmetric nucleus is invariant under space inversion, $\hat{P}$, and a rotation of 180° about an axis perpendicular to the symmetry axis, $\hat{R}$. That is, this nucleus possesses the symmetries of parity and signature. A reflection-asymmetric nucleus breaks these two symmetries and the only remaining symmetry, *simplex*, is a combination of signature and parity,

$$\hat{S} = \hat{P}\hat{R}^{-1}. \tag{2.1}$$

The simplex symmetry is equivalent to a reflection in a plane containing the symmetry axis, as shown in figure 2.2.

The eigenvalue of the simplex operator, s, can be used to label states in a reflection-asymmetric nucleus. The relationship between s, the parity eigenvalue, p, and the spin, I, is

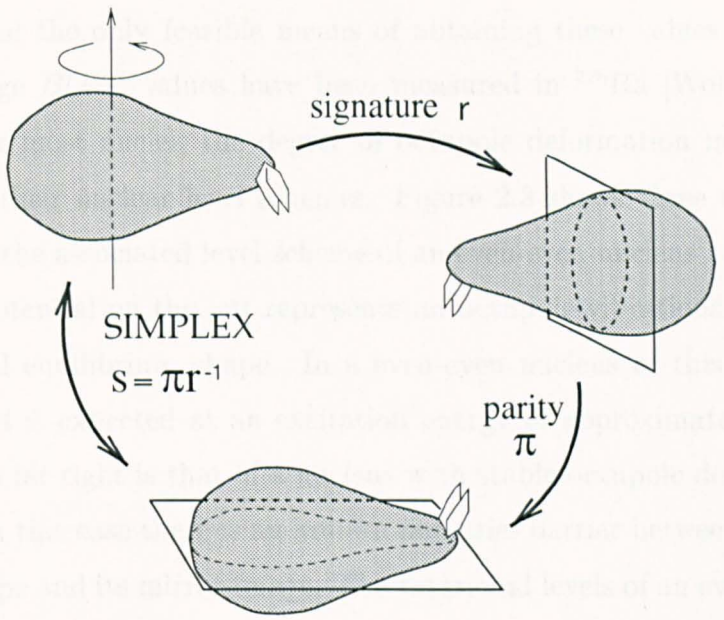

Figure 2.2: A schematic representation of the simplex operation, a combination of the signature and parity operations.

$$p = se^{i\pi I}. \tag{2.2}$$

States of an even-even nucleus have integral values of I, so s = ±1. Alternating-parity rotational bands are expected which are labelled in the following way:

$$\text{s= } +1\text{: } I^\pi = 0^+, 1^-, 2^+, 3^-, 4^+ \ldots$$
$$\text{s= } -1\text{: } I^\pi = 0^-, 1^+, 2^-, 3^+, 4^- \ldots$$

The excited states of an odd-mass nucleus have half-integral spin values and s = ±i. States are labelled thus:

$$\text{s= } +i\text{: } I^\pi = \tfrac{1}{2}^+, \tfrac{3}{2}^-, \tfrac{5}{2}^+, \tfrac{7}{2}^-, \tfrac{9}{2}^+ \ldots$$
$$\text{s= } -i\text{: } I^\pi = \tfrac{1}{2}^-, \tfrac{3}{2}^+, \tfrac{5}{2}^-, \tfrac{7}{2}^+, \tfrac{9}{2}^- \ldots$$

The extent of octupole deformation in nuclei is a difficult quantity to determine. Measurement of electric octupole moments, or $B(E3)$ values, is the most direct assessment but typical $E3$ strengths are 10^4 times weaker than competing $E1$ and

$E2$ strengths and the only feasible means of obtaining these values is by Coulomb excitation. Large $B(E3)$ values have been measured in ^{226}Ra [Wollersheim 93] by this means. For most nuclei, the degree of octupole deformation must be inferred indirectly from their nuclear level schemes. Figure 2.3 shows three octupole potentials along with the associated level scheme of an even-even nucleus and an odd-mass nucleus. The potential on the left represents an octupole-vibrational nucleus which has a spheroidal equilibrium shape. In a even-even nucleus of this kind a $K^{\pi}=0^{-}$ vibrational band is expected at an excitation energy of approximately 1 MeV. The potential on the far right is that of a nucleus with stable octupole deformation in its ground state. In this case there is an infinite potential barrier between the reflection-asymmetric shape and its mirror image. The rotational levels of an even-even nucleus of this type are predicted to be quite similar to those of asymmetric molecules like HCl. That is, one expects a sequence of regularly-spaced alternating-parity states. In an odd-mass nucleus of this kind one would see exactly-degenerate parity-doublet bands. In the intermediate case there is a finite possibility of tunnelling between the reflection-asymmetric shape and the mirror image. The negative-parity states are displaced upwards in energy in this case.

Positive- and negative-parity states in the sequence I^{+}, $(I+1)^{-}$, $(I+2)^{+}$ ... were first observed in ^{218}Ra [Fernández-Niello 82] and ^{222}Th [Ward 83], [Bonin 83]. However, the opposite-parity states in these nuclei only begin to interleave at spins $I > 5\hbar$. Even in the most favourable cases the opposite-parity states only become interleaved at around $5\hbar$ or $7\hbar$ and in no case is the 1^{-} state observed to be below that of the 2^{+} state. It is generally believed that there are no nuclei which have permanent ground-state octupole deformation, and that even the best candidates for octupole deformation behave like the intermediate case in figure 2.3.

In many octupole-deformed nuclei the displacement between the positive- and negative-parity states is reduced to zero, as expected for a reflection-asymmetric rotor, at spins of $10\hbar$ or greater. It appears as though rotation stabilises or even induces the octupole deformation. One explanation for this is that the rotation lowers

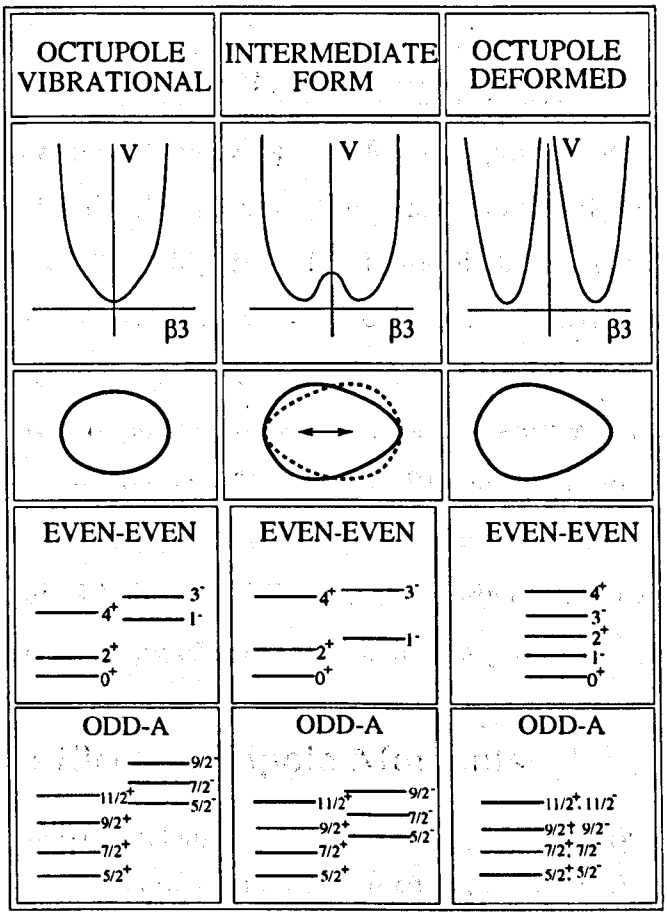

Figure 2.3: The nuclear potentials of an octupole-vibrational nucleus and an octupole-deformed nucleus together with an intermediate case. Also shown are the theoretical level schemes for even-even and odd-mass nuclei.

the intruder states and may bring pairs of octupole-driving orbitals closer together. Nazarewicz and Olanders [Nazarewicz 85] defined two quantities designed to illustrate the behaviour of octupole nuclei at high spins. Parity splitting, δE, is defined as

$$\delta E = E(I)^- - \frac{1}{2}(E(I+1)^+ + E(I-1)^+) \tag{2.3}$$

and is a measure of the displacement between a negative-parity state and the midpoint of the two adjacent positive-parity states. This should be zero for a perfect octupole-rotor. The other quantity, the rotational frequency ratio, is defined as

$$R = \frac{\omega^-(I)}{\omega^+(I)} = 2\frac{E(I+1)^- - E(I-1)^-}{E(I+2)^+ - E(I-2)^+}. \quad (2.4)$$

This quantity should approach unity for a perfect octupole-rotor, that is the positive- and negative-parity bands should have the same rotational frequencies. For an octupole-vibrator, R = (2I − 5)/(2I + 1). Plots of these quantities for the nuclei studied in this thesis are given in section 6.6.4. For detailed theoretical studies of octupole nuclei at high spins, see references [Nazarewicz 87] and [Nazarewicz 87a].

Interleaving states of opposite parity were observed earlier in medium mass nuclei (for example in ^{150}Sm [Sujkowski 77] and ^{150}Gd [Haenni 77]) but the first interpretation of such features in terms of static octupole deformation in this mass region was made by Phillips *et al.* [Phillips 86] following the study of even-even barium isotopes using gamma-ray spectroscopy of spontaneous-fission products.

2.2.3 Intrinsic Electric Dipole Moments

In a reflection-asymmetric nucleus, yrast states of opposite parity are often connected by strong $E1$ transitions. Typical values for $B(E1)$ in octupole-deformed nuclei range from 10^{-4} to 10^{-2} single-particle or Weisskopf units. These $E1$ strengths are only a fraction of the single-particle estimate, but are still a few orders of magnitude larger than those measured in other regions of the nuclear chart. The enhancement of the $E1$ strength in reflection-asymmetric nuclei was proposed [Leander 82], [Bohr 58], [Bohr 57], [Strutinsky 56] to be due to an intrinsic electric dipole moment, induced by a displacement of the centre of charge from the centre of mass. The shift of the centre of charge is caused by the tendency of the protons to gather at the narrow end of the octupole shape, where the radius of curvature of the equi-potential surface is smallest.

Assuming that nucleons are point-like particles, in an axially-symmetric deformed system the intrinsic electric dipole moment can be written as [Butler 91]

$$D_0 = e\frac{NZ}{A}[< z_{p,c.m} > - < z_{n,c.m} >] \quad (2.5)$$

where $< z_{p,c.m} >$ and $< z_{n,c.m} >$ are the centre-of-mass coordinates for protons and neutrons, respectively. In a reflection-asymmetric nucleus intrinsic parity is broken, $< z_{p,c.m} > \neq < z_{n,c.m} >$ and $D_0 \neq 0$. The weakness of the Coulomb force relative to the nuclear force ensures that the nuclear dipole moments are small, yet large enough to account for the $E1$ transition strengths which are observed experimentally.

As well as the macroscopic contribution, a microscopic, shell-correction, contribution to D_0 should also be considered [Leander 86], [Butler 91]. The intrinsic electric dipole moment is then written as

$$D_0 = D_0^{macr} + D_0^{shell}. \tag{2.6}$$

The shell-correction contribution has been calculated [Butler 91] to be roughly the same magnitude as the macroscopic term and the two terms can add constructively or destructively. This means that nuclei with similar shapes can have very different intrinsic electric dipole moments, and the extraction of β_3 deformations from D_0 values is difficult. The calculations of Leander *et al.* used a liquid-drop model to calculate the macroscopic contribution to the dipole moment and a deformed Woods-Saxon potential to obtain the shell-correction. The overall trend of experimental results was reproduced for radium and thorium isotopes using these calculations. The calculations of Butler and Nazarewicz [Butler 91] included higher-order deformations (up to β_8) and used a droplet model [Dorso 86] to calculate the macroscopic term. This model accounts for effects due to neutron skins. The calculations reproduced the experimental systematics for both medium mass and heavy nuclei. The macroscopic and microscopic contributions to D_0 cancelled for ^{224}Ra using these calculations, as seen experimentally [Poynter 89a], [Marten-Tölle 90]. A very small electric dipole moment was also calculated for ^{146}Ba. A compilation of published D_0 values is given in [Butler 96].

2.3 Regions of Octupole Deformation

The strongest octupole correlations appear in two regions of the nuclear chart. These are the light-actinide region (nuclei close to $^{224}_{90}Th_{134}$) and the lanthanide region (nuclei close to $^{146}_{56}Ba_{90}$). Octupole effects have also been observed in other regions, for example in ^{64}Ge [Ennis 91], ^{96}Zr [Hofer 93], [Horen 93] and ^{132}Sn [Fogelberg 94]. A survey of the evidence for reflection-asymmetry in atomic nuclei is given in [Butler 96].

The Light-Actinide Region: Motivation for Further Studies

The first observation of collective low-spin negative-parity states in the decay products of natural radioisotopes prompted much theoretical work concerning the structure of these nuclei. The shaded area in figure 2.4 shows the region of light-actinide nuclei which are predicted to be octupole deformed [Sheline 87], [Nazarewicz 84]. The nuclei which are assigned a reference are those in which an alternating-parity band has been observed. Most of the nuclei on the left in the figure are populated using compound-nucleus reactions with ^{11}B, ^{12,13,14}C and ^{16,18}O beams and ^{208}Pb and ^{209}Bi targets. The thorium isotopes with $225 \leq A \leq 228$ are populated using (α,xn) reactions with ^{226}Ra targets ($t_{1/2}$=1600 years). High-spin spectroscopy of ^{226}Ra and ^{230}Th ($t_{1/2}$= 7.5×10^4 years) has been obtained using Coulomb excitation reactions and ^{224}Ra has been observed up to $I^\pi = 12^+$ using two-neutron transfer from ^{226}Ra. The advent of the third generation of highly-efficient germanium detector arrays [Nolan 95] allowed high-spin studies of nuclei such as ^{222}Th which is produced with a cross-section of the order of tens of millibarns in the ^{208}Pb(^{18}O,4n)^{222}Th reaction [Smith 95]. The absence of a stable target above ^{209}Bi and suitable projectiles means that other nuclei in the octupole (shaded) region are difficult to access. The cross-sections for producing these nuclei using compound-nucleus reactions with presently-available beams and targets are too low for studies involving standard gamma-ray coincidence techniques. Prior to the present work, no high-spin information concerning ^{222}Ra and the radon isotopes with $A \geq 218$ existed. In order to study these nuclei, either channel-selection techniques or alternative population mechanisms must be employed. Thus arises the

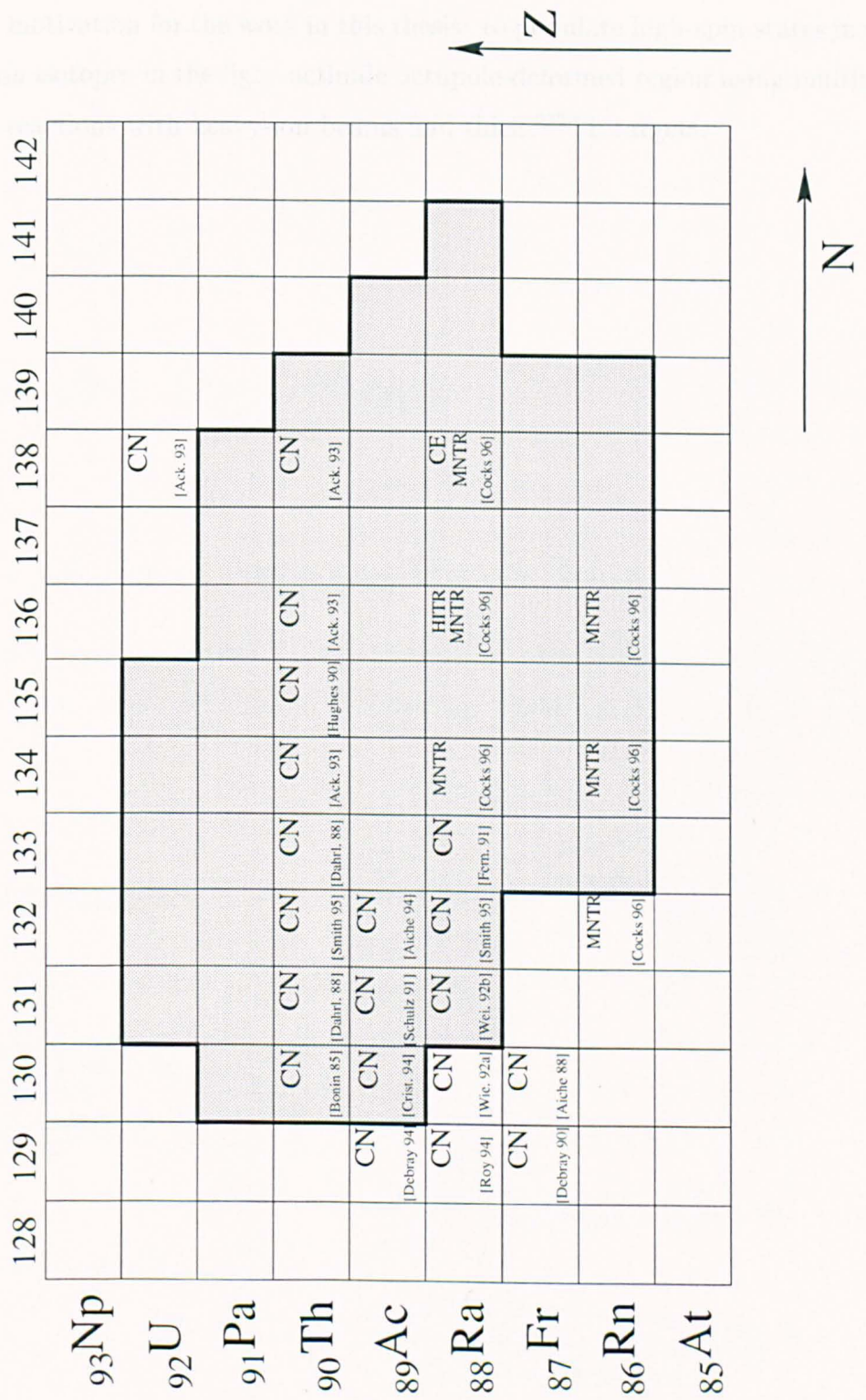

Figure 2.4: The actinide region. The shaded area is the predicted region of octupole deformation [Sheline 87], [Nazarewicz 87]. Nuclei in which alternating-parity bands have been observed are assigned a reference to the most recent experimental work. The mechanisms by which high-spin states in these nuclei were populated are: CN - compound nucleus reactions; CE - Coulomb excitation; HITR - heavy-ion transfer reactions; MNTR - multinucleon transfer reactions.

primary motivation for the work in this thesis: to populate high-spin states in radium and radon isotopes in the light-actinide octupole-deformed region using multinucleon transfer reactions with heavy-ion beams and thick ^{232}Th targets.

Chapter 3

Transfer Reactions

3.1 Collisions Between Heavy Ions

When a heavy-ion projectile of energy less than 10 MeV/nucleon collides with a target nucleus, several types of interaction can occur. These are shown in figure 3.1.

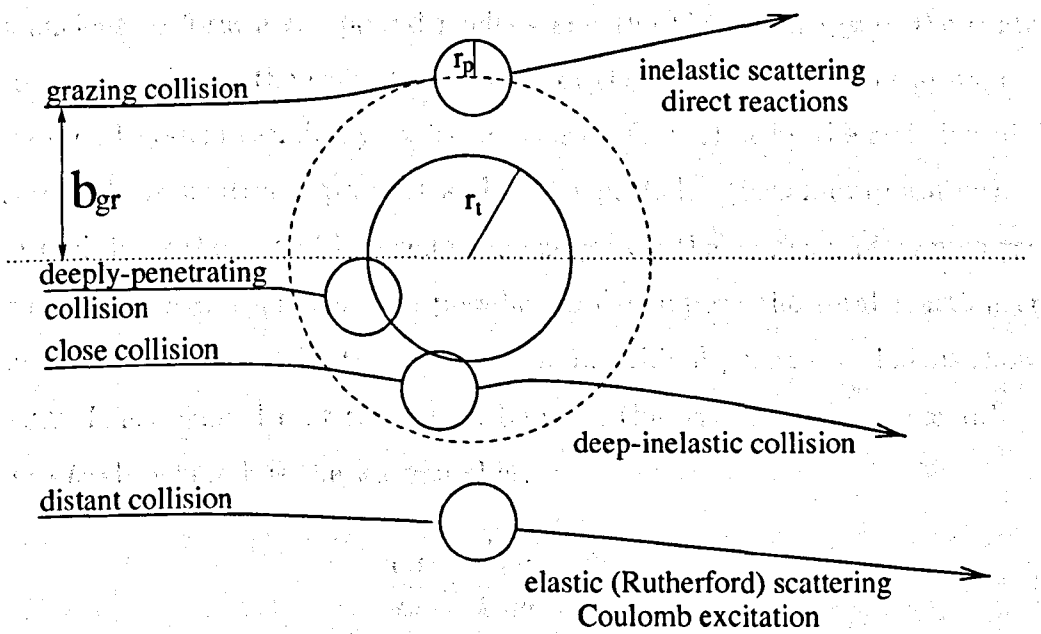

Figure 3.1: A schematic representation of the different categories of heavy-ion collision.

The probability of a certain interaction occurring is dependent upon the centre of mass energy, the impact parameter, b (or angular momentum, l, since $\hbar l = p_p b$ where p_p is the momentum of the projectile), and the nature (mass, charge, shape and softness) of the target and projectile. For impact parameters larger than the grazing impact parameter, $b > b_{gr}$, the interaction between the target and projectile nuclei is negligible and there is no transfer of nucleons between the two heavy ions. These *distant collisions* result in processes such as Coulomb excitation or elastic scattering and their trajectories are determined by the Coulomb potential. *Grazing collisions* occur for $b \approx b_{gr}$. The onset of the nuclear interaction results in processes such as inelastic scattering and the transfer of a few nucleons between the target and projectile. For $b < b_{gr}$ there is significant overlap of nuclear matter. Here it is useful to distinguish between two types of reaction: one where partial memory of the entrance channel is retained and the other where there is complete loss of target and projectile identity. *Deep-inelastic processes* belong to the former category and are discussed in more detail in the next section. The other category includes *deeply-penetrating collisions.* In this type of process the incident particle is captured by the target nucleus to form a compound nucleus and the kinetic energy of the centre of mass is converted into the excitation energy of the compound-nucleus system. The highly-excited system can decay by fission (fusion-fission) or by the emission of light particles such as neutrons, protons and alpha particles (fusion-evaporation). The system then loses the rest of its excitation energy via the emission of gamma rays.

Using a classical approach it is possible to decompose the total reaction cross-section into separate contributions due to the individual processes. This is shown in figure 3.2. It is assumed that the cut off between the reaction types is smooth.

Since l=kb, where k is the wavenumber,

$$\frac{d\sigma}{dl} = \frac{1}{k}\frac{d\sigma}{db} = \frac{2\pi}{k^2}l. \tag{3.1}$$

The linear dependence of $d\sigma/dl$ with l may be observed in the figure. For small angular momenta, $l < l_{crit}$, the reaction cross-section represents compound-nucleus

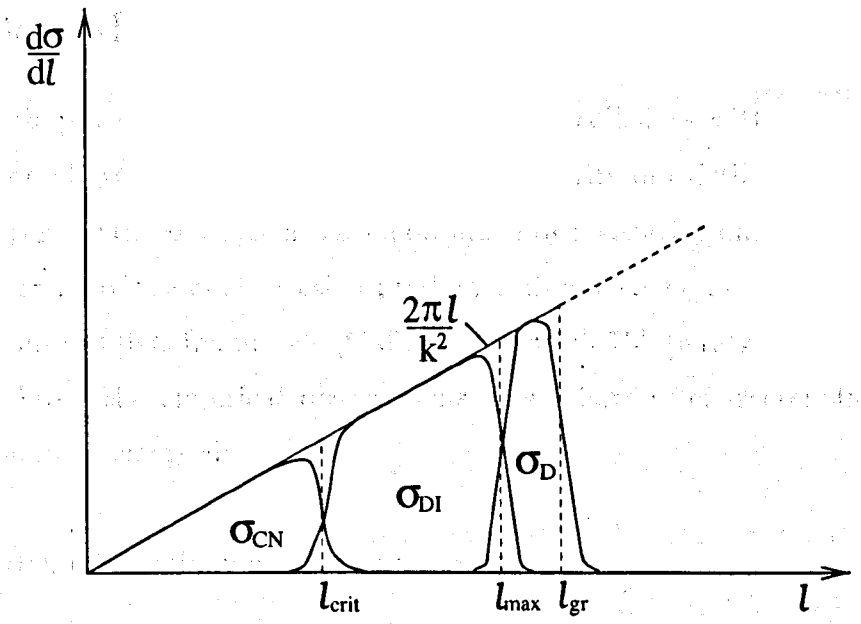

Figure 3.2: Schematic decomposition of the total reaction cross-section into the cross-sections for compound nucleus formation (σ_{CN}), deep inelastic collisions (σ_{DIC}) and direct collisions (σ_D).

formation. The cross-section of deep-inelastic processes is located at $l_{crit} < l < l_{max}$ and direct processes are represented by the cross-section at $l_{max} < l < l_{gr}$. At $l > l_{gr}$, the reaction cross-section is dominated by elastic scattering and Coulomb excitation. The values of the angular momenta l_{crit}, l_{max} and l_{gr} are dependent upon the energy of the collision and the choice of target and projectile.

3.2 Deep-Inelastic Collisions

Deep-inelastic processes dominate in very heavy-ion collisions with energies of a few MeV/nucleon above the Coulomb barrier. The majority of existing information concerning deep-inelastic collisions has been obtained by measuring one or more of the following properties of the final reaction products: kinetic energy, charge, mass and angular distributions [Kaufmann 59], [Galin 70], [Artukh 73], [Kratz 74], [Hanappe 74], [Wolf 74]. From the empirical observations, the following characteristics of deep-inelastic collisions emerged:

- The reaction is essentially a binary process;

- The primary fragments de-excite through the emission of light particles (p, n, α) and/or fission before emitting gamma rays;

- The final kinetic energies of the products range from elastic energies down to those corresponding to the Coulomb repulsion of the final fragments;

- An exchange of nucleons occurs during the interaction leading to mass and charge distributions of the fragments. These distributions have their maxima in the vicinity of the projectile and target mass and charge;

- The mass and charge equilibrate. That is, the average neutron-to-proton ratio (N/Z) of both fragments develops towards that of the intermediate complex;

- The angular distributions are strongly forward-peaked and non-symmetric, indicating that the combined system separates in a time shorter than its rotation period;

- Angular momentum is transferred from relative orbital motion to the intrinsic spin of the two primary fragments. The amount of transferred angular momentum is large

and states up to spin $30\hbar$ have been observed in deep-inelastic reaction products [Broda 96].

3.2.1 Energy Loss

The amount of dissipated kinetic energy in deep-inelastic collisions may be correlated with the amount of mass and charge transfer. Rudolf *et al.* [Rudolf 79] studied projectile-like products of the ^{166}Er + 8.18 MeV/nucleon ^{86}Kr reaction using a large-area position-sensitive ionization chamber. A contour plot of the double differential cross-section $d^2\sigma/d(TKE)dZ$ was constructed (see figure 3.3) assuming the formation of only two fragments in the reaction. The quantity TKE represents the final kinetic

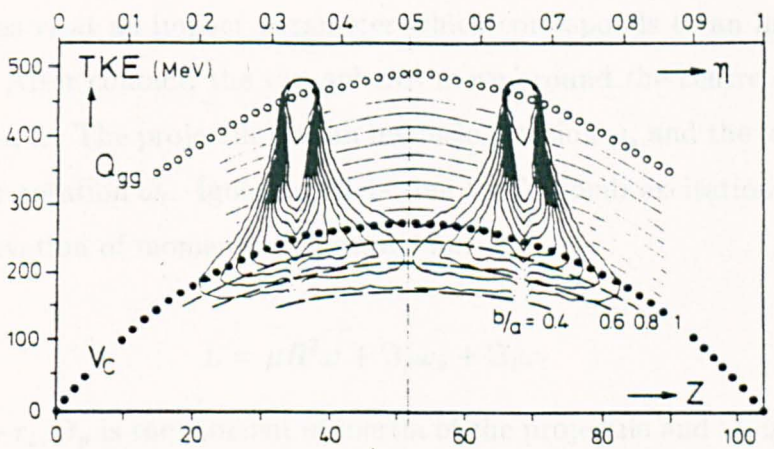

Figure 3.3: Contour diagram of $d^2\sigma/d(TKE)dZ$ for binary products of the ^{166}Er + 8.18 MeV/u ^{86}Kr reaction. The quantity Q_{gg} represents the maximum ground state reaction Q-value. Taken from [Rudolf 79].

energy of the two fragments. The quantity Q_{gg} is the beam energy with the ground state Q-value subtracted. The parameter V_c represents the Coulomb repulsion of two touching spheres. Also shown are the Coulomb energies of touching ellipsoids with axis ratios of 0.4, 0.6 and 0.8. For elastic and quasi-elastic processes the charge

numbers of the products are the same or similar to those of the target and projectile. The TKE of these fragments is close to the centre of mass collision energy and there is very little energy loss (TKE $\approx Q_{gg}$). Collisions which involve charge transfers greater than two or three units are characterised by TKE $< Q_{gg}$. The transition from small to large energy losses corresponds to the gradual onset of deep-inelastic processes and one may observe that TKE ranges from Q_{gg} down to V_c as one moves away from the charge numbers of the projectile and target. In some cases TKE falls below V_c and may be compared to the Coulomb repulsion of two deformed fragments.

3.3 Angular Momentum Dissipation

Consider a spherical projectile nucleus of radius r_p approaching a spherical target nucleus of radius r_t at an impact parameter which corresponds to an initial angular momentum L. After contact, the two spheres move around the centre of mass with an angular speed ω. The projectile has an intrinsic rotation ω_p and the target nucleus has an intrinsic rotation ω_t. Ignoring effcts due to Coulomb excitation and particle transfer, conservation of momentum dictates that

$$L = \mu R^2 \omega + \Im_p \omega_p + \Im_t \omega_t \tag{3.2}$$

where $R = r_p + r_t$, $\Im_p$ is the moment of inertia of the projectile and $\Im_t$ is the moment of inertia of the target. The quantity μ is the reduced mass which is given by

$$\mu = \frac{A_p A_t}{A_p + A_t} \tag{3.3}$$

where A_p and A_t are the projectile and target mass numbers. The intrinsic angular momenta of the target and projectile are $I_t = \Im_t \omega_t$ and $I_p = \Im_p \omega_p$ respectively.

The amount of angular momentum which is converted from the initial angular momentum of the system to the intrinsic angular momentum of the target and projectile nuclei depends upon the frictional forces between the two nuclei. There are three main models which can be used to estimate this. These are the *sliding*, *rolling*, and

sticking models which correspond to minimum, intermediate and maximum angular momentum dissipation.

Sliding

In the sliding model there is no intrinsic rotation and the angular momentum remains as relative motion. In this case $\omega_p = \omega_t = 0$ and $I_t = I_p = 0$.

Sticking

In this model the target and projectile stick together. Each nucleus rotates about the centre of mass with an angular speed ω. In this case, equation 3.2 becomes

$$L = \mu R^2 \omega + \Im_p \omega + \Im_t \omega. \tag{3.4}$$

One can then obtain the following expressions for the intrinsic rotational angular momentum for the target and projectile:

$$I_t = \frac{\Im_t}{\mu R^2 + \Im_p + \Im_t} L \tag{3.5}$$

and

$$I_p = \frac{\Im_p}{\mu R^2 + \Im_p + \Im_t} L \tag{3.6}$$

where $R = r_p + r_t$, $\Im_t = \frac{2}{5} A_t r_t^2$ and $\Im_p = \frac{2}{5} A_p r_p^2$. In chapter 6 of this thesis an experiment is described where high-spin states in target-like transfer-reaction products are populated using the reaction ^{232}Th + 833 MeV ^{136}Xe. The upper limit on the angular momentum for compound-nucleus formation, l_{crit}, was calculated to be $252\hbar$ using the following equation

$$l_{crit} = r_{crit} \sqrt{\frac{1}{20} \mu (E_{cm} - C_{cm})} \tag{3.7}$$

where r_{crit} was taken as $1.2(A_t^{1/3} + A_p^{1/3}) + 1$, E_{cm} is the centre-of-mass energy of the projectile and C_{cm} is Coulomb barrier energy in the centre-of-mass frame. Using equations 3.5 and 3.6 with $L = 252\hbar$ and $r = 1.2A^{1/3}$, estimates for I_t and I_p were

obtained for the reaction. These were $I_t = 56\hbar$ and $I_p = 23\hbar$.

Rolling

An intermediate situation between sliding and sticking can arise in the presence of strong frictional forces. In the case of the rolling limit, $\frac{2}{7}$ of the initial angular momentum is converted to the intrinsic spin of the target and projectile, while $\frac{5}{7}$ remains in relative motion [Moretto 81]. The intrinsic angular momenta of the target and projectile are

$$I_t = \frac{2}{7}\left(\frac{1}{1+\left(\frac{A_t}{A_p}\right)^{1/3}}\right)L \tag{3.8}$$

and

$$I_p = \frac{2}{7}\left(\frac{1}{1+\left(\frac{A_p}{A_t}\right)^{1/3}}\right)L. \tag{3.9}$$

For the ^{232}Th + ^{136}Xe reaction the intrinsic angular momenta are predicted to be $I_t = 39\hbar$ and $I_p = 33\hbar$. Of the three models, the rolling limit produces estimates which are most consistent with experimental data and it is this limit which is usually quoted in literature.

3.4 Gamma-ray Spectroscopy

In previous work, excited states in quasi-elastic transfer-reaction products have been studied using particle-γ coincidence techniques [Takai 88], [Wu 87], [Cresswell 95]. In these experiments, prompt gamma-ray emissions were collected with germanium detectors and transfer-reaction products were selected using particle detectors. The advent of high-efficiency Compton-suppressed germanium-detector arrays enabled the study of structures which are populated with low cross-sections. The increase in selectivity delivered by these devices prompted a different approach to the study of high-spin states in transfer-reaction products. In the early part of this decade, the

Kraków group pioneered these experiments which involved deep-inelastic collisions with heavy-ion beams and thick targets [Broda 90]. In this approach, particle detection is rendered unnecessary and efficient germanium-detector arrays are used to collect gamma-ray coincidence data: thick targets are used to stop all reaction products and gamma rays which are emitted from stationary nuclei appear as narrow peaks with no Doppler broadening component. Gamma rays from nuclei slowing down in the target contribute to a continuous background in the spectra. Gamma rays arising from contaminant processes such as Coulomb excitation of the target, compound-nucleus formation, fusion-fission and transfer-fission are present, as well as those which are attributed to many binary-reaction products. The resulting complexity of the spectra can be resolved using γ-γ coincidence techniques if the data set has sufficiently high statistics and good energy resolution. If enough gamma-ray information concerning the transfer-reaction products exists, this approach can allow precise product identification and yield measurements can be made [Broda 94], [Królas 94]. In favourable cases the mutual excitation of the two binary-reaction products may be directly observed through cross-coincidence of gamma rays from both reaction partners. Observation of this cross-coincidence provides immediate identification of both outgoing nuclei and establishes whether or not an emission of nucleons occurred in the process. A great deal of spectroscopic information concerning many projectile- and target-like binary reaction products has been obtained using this technique [Broda 95], [Fornal 94], [Mayer 94]. Such experiments have so far exploited the ability of these reactions to populate neutron-rich systems that are otherwise difficult to access.

Multinucleon transfer reactions have previously been used to populate nuclei in the actinide mass region of the nuclear chart. In 1986 Gäggeler *et al.* [Gäggeler 86] identified many light-actinide nuclei as products of deep-inelastic transfer from a ^{248}Cm target. Products were identified using radiochemical techniques. In the present work, multinucleon transfer reactions are used to populate light-actinide nuclei in the octupole region (see section 2.3). The reactions involve heavy-ion beams and thick ^{232}Th

targets. Gamma-ray coincidence techniques are used to provide yield measurements for the nuclei which are populated and also to study excited states in target-like reaction products. The experiments are described in chapters 5 and 6.

Chapter 4

Gamma-ray Spectroscopy

4.1 Gamma-ray detection

4.1.1 Gamma-ray Interactions

There are three main types of interaction between a gamma ray and an absorbing medium.

Photoelectric Absorption

Photoelectric absorption involves the complete transfer of photon energy, $h\nu$, to a bound atomic electron in the absorber material. The electron is subsequently ejected from its atomic shell. The kinetic energy imparted to the electron, T, is given by

$$T = h\nu - E_{bind} \tag{4.1}$$

where E_{bind} is the binding energy of the electron. This process can only occur for bound electrons in order to conserve both energy and momentum. The probability of a photoelectric interaction, τ, is a rapidly-increasing function of the atomic number of the absorber, Z. An approximate dependence is given by

$$\tau = \text{constant} \times \frac{Z^n}{E_\gamma^{3.5}} \tag{4.2}$$

where E_γ is the energy of the incident gamma ray and $n \simeq 4$ or 5. The Z-dependence explains the use of high-Z materials for gamma-ray shielding, such as lead, and for gamma-ray detectors, such as germanium. The photoelectric effect is the most likely interaction for gamma rays with $E_\gamma < 200$ keV.

Compton Scattering

In the Compton scattering process, the incident gamma ray scatters off an electron in the absorbing material, transferring only part if its energy. This electron is known as the *recoil electron.* This process is shown in figure 4.1.

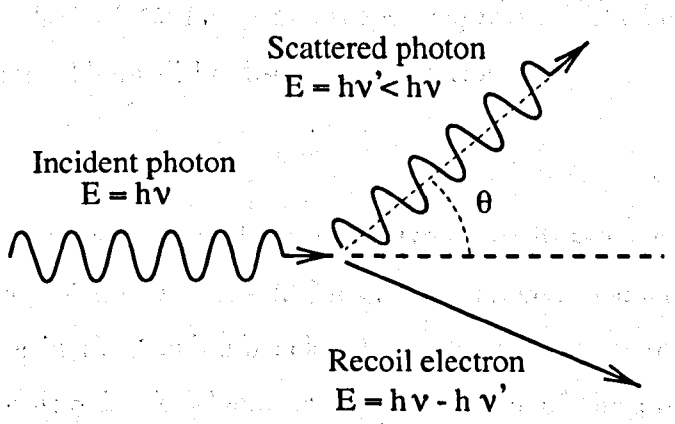

Figure 4.1: A schematic representation of the Compton scattering process.

By considering energy and momentum conservation, an expression can be derived for the energy of the scattered photon, $h\nu'$, in terms of the incident photon energy, $h\nu$, the scattering angle, θ, and the electron rest mass energy $m_o c^2$:

$$h\nu' = \frac{h\nu}{1 + \frac{h\nu}{m_o c^2}(1 - cos\theta)}. \tag{4.3}$$

For small scattering angles, $\theta \approx 0$, very little of the incident gamma-ray energy is transferred to the recoil electron. For $\theta = \pi$, maximum energy transfer occurs and the photon scatters backwards but still retains some of its energy.

Compton scattering is the most probable process for gamma rays with energies

in the range 200-1000 keV. The probability of this process occurring is dependent upon the number of electrons present in the absorbing material and thus increases with atomic number Z. For the gamma rays of interest in this work the most probable interaction is Compton scattering. However, this process poses a problem to the gamma-ray spectroscopist. If the full energy of the scattered gamma ray is to be measured by the detector, then it must undergo multiple Compton scatterings yet still remain inside the detector crystal. If the gamma ray scatters out of the detector having deposited only part of its energy then a false reading of the incident gamma-ray energy will be given. In this case the measured energy will increase the background by contributing to the *Compton continuum.* In order to reduce this background the method of *Compton* or *escape suppression* has been introduced to gamma-ray detection. This will be discussed in section 4.4.

Pair Production

A gamma ray can change into an electron-positron pair if its energy is greater than the rest-mass energy of the pair, 1.022 MeV. This process, called pair production, can only take place in the Coulomb field of an absorber atom so that energy and momentum are conserved. A schematic representation of the process is shown in figure 4.2.

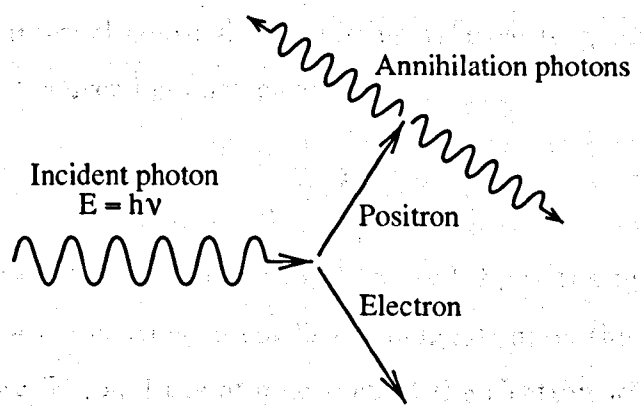

Figure 4.2: A schematic representation of the pair production process.

If the incident photon has an energy greater than $2m_oc^2$ then the residual energy,

$h\nu - 2m_oc^2$, is equally divided between the electron and positron as kinetic energy. This kinetic energy is lost as the two particles slow down in the absorbing material. When the positron has slowed down to the thermal velocity of the surrounding electrons it will annihilate with an atomic electron creating two back-to-back photons of energy 511 keV. Single- and double-escape peaks can arise in gamma-ray spectra at 511 keV and 1022 keV below photopeak energies, corresponding to the escape of one or both of the annihilation photons, respectively. Pair production is an important process for gamma rays with energies in the range 5-10 MeV. The probability of this process occurring varies as the square of the atomic number of the absorber material.

4.2 Internal Conversion

Internal conversion is an electromagnetic process that can compete with gamma-ray emission. In this process the excitation energy of the nucleus is given to an atomic electron, causing the electron to be emitted from the atom. The kinetic energy imparted to the electron, T_e, is the gamma-ray transition energy, E_γ, less the binding energy of the electron, B_e:

$$T_e = E_\gamma - B_e. \tag{4.4}$$

The probability of internal conversion occurring relative to gamma-ray emission is given by the internal-conversion coefficient, α:

$$\alpha = \frac{\lambda_e}{\lambda_\gamma} \tag{4.5}$$

where λ_e is the internal-conversion probability and λ_γ is the gamma-ray emission probability. The internal-conversion coefficient depends upon the atomic number, Z, the transition energy, E_γ, and the atomic shell of the electron which is given by the quantum number n (where n = 1, 2, 3, 4 corresponds to the atomic shells K, L, M, N). The approximate dependence is

$$\alpha = \text{constant} \frac{Z^3}{n^3 E_\gamma^{2.5}}. \tag{4.6}$$

The internal-conversion coefficient also depends upon the multipolarity of the gamma-ray transition and coefficients are larger for magnetic transitions than for electric transitions. Internal conversion competes with many of the gamma-ray transitions in nuclei studied in this work. The gamma-ray intensities of these transitions had to be corrected using calculated conversion coefficients in order to obtain the total transition intensities. If I_γ is the measured gamma-ray intensity, then the total gamma-ray intensity, I_T, is given by

$$I_T = I_\gamma(1 + \alpha). \tag{4.7}$$

Internal-conversion coefficients have been tabulated by many authors, for example Sliv and Band [Sliv 65], Hager and Seltzer [Hager 68], [Hager 69], Dragoun *et al.* [Dragoun 69], Trusov [Trusov 72] and Rösel, Alder, Fries and Pauli [Rösel 78]. The tables of Rösel, Alder, Fries and Pauli were used to correct the gamma-ray intensities which were measured in this work.

4.3 Germanium Detectors

Gamma-ray spectroscopy experiments utilise the high resolution offered by germanium detectors. Like other semiconductor detectors, germanium detectors consist of a reverse-biased p-n junction diode. When the n- and p-type semiconductor materials are brought together the electrons from the n-type material diffuse across the junction into the p-type material where they combine with holes. This migration of charge-carriers results in an absence of charge in the vicinity of the interface of the two materials. This *depletion region* is the active volume where the gamma radiation is detected and is required to be as large as possible. The region may be extended by applying a reverse-bias across the junction. The width of the depletion region is proportional to $(\frac{V}{N})^{\frac{1}{2}}$, where V is the bias voltage and N is the impurity concentra-

tion in the germanium. Even with a large bias applied, natural-purity germanium can withstand a depletion layer of no more than a few millimetres before electrical breakdown occurs. This amount of depletion is not sufficient for the detection of gamma rays with energies greater than 100 keV. This restriction necessitated the use of lithium-doped germanium (Ge(Li)) detectors and, more recently, the development of high-purity germanium (HPGe) crystals. HPGe crystals are pure enough to support a large depletion region without the need for dopants. Their purity is not effected by temperature and so they can be stored at room temperature, while Ge(Li) detectors must be stored at 77 K. An active volume of 10-30 cm^3 can be achieved with a planar HPGe crystal, but this can be increased to 400 cm^3 using a bulletized coaxial crystal design. This design is shown in figure 4.3. Bulletizing or 'rounding-

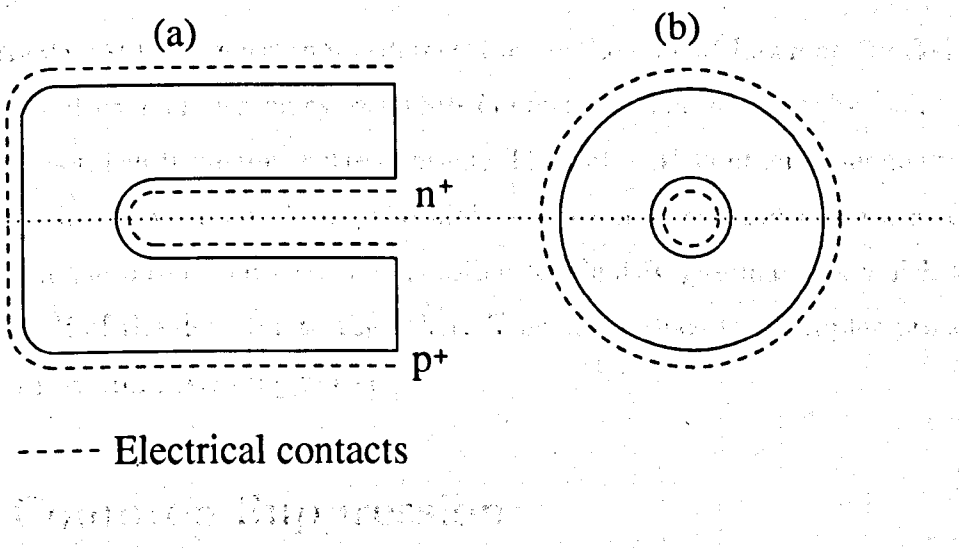

Figure 4.3: Crossections (a) parallel and (b) perpendicular to the cylindrical axis of a bulletized coaxial n-type germanium detector crystal.

off-the-corners' helps keep the electric field uniform inside the crystal. In an n-type crystal the n^+ contact is on the inside because it is much thicker than the p^+ contact. In this arrangement, attenuation of the incident radiation is kept to a minimum. This is one reason why n-type germanium detectors are used in gamma-ray spectroscopy experiments. Another reason is that p-type detectors are much more susceptible to

neutron damage. Although HPGe detectors can be stored at room temperature, they must be kept cold during operation. Cooling inhibits the thermal excitation of electrons across the band gap, thus reducing noise. The crystal is cooled by making a thermal contact between the crystal and a dewar of liquid nitrogen at 77 K using a copper rod called a *cold-finger*.

When a gamma-ray interacts with a HPGe crystal by one of the mechanisms described in section 4.1.1, it produces electron-hole pairs by ionising atoms in the depletion region of the detector crystal. The electron-hole pairs are swept towards the electrical contacts by the large reverse-bias where they constitute an electrical current. A comparatively low ionization energy, 3 eV, is required to create an electron-hole pair in germanium. This means that many pairs are created (~33000 ion pairs for a 1 MeV gamma ray) and statistical fluctuations are low, resulting in excellent energy resolution.

The GAMMASPHERE germanium-detector array [Lee 90] at Lawrence Berkeley National Laboratory includes many *segmented* detectors. The main high-resolution energy signal is taken from the centre contact. The outer p^+ contact is segmented into two parts [Macchiavelli 94]. Using the high-resolution signal and the low-resolution signals from the outer contacts, it is possible to identify gamma rays which scatter from one half of the detector to the other. This can reduce the Doppler broadening of gamma rays from recoiling nuclei.

4.4 Compton Suppression

Figure 4.4 shows the spectrum of gamma-rays produced following the β^- decay of ^{60}Co collected using a germanium detector with (thin-line spectrum) and without (thick-line spectrum) Compton suppression applied. Compton suppression reduces the Compton continuum (see section 4.1.1) and thereby increases the peak-to-total ratio. The peak-to-total ratio is the number of counts in the photo-peak divided by the total number of counts in the spectrum above 100 keV. This ratio should be as

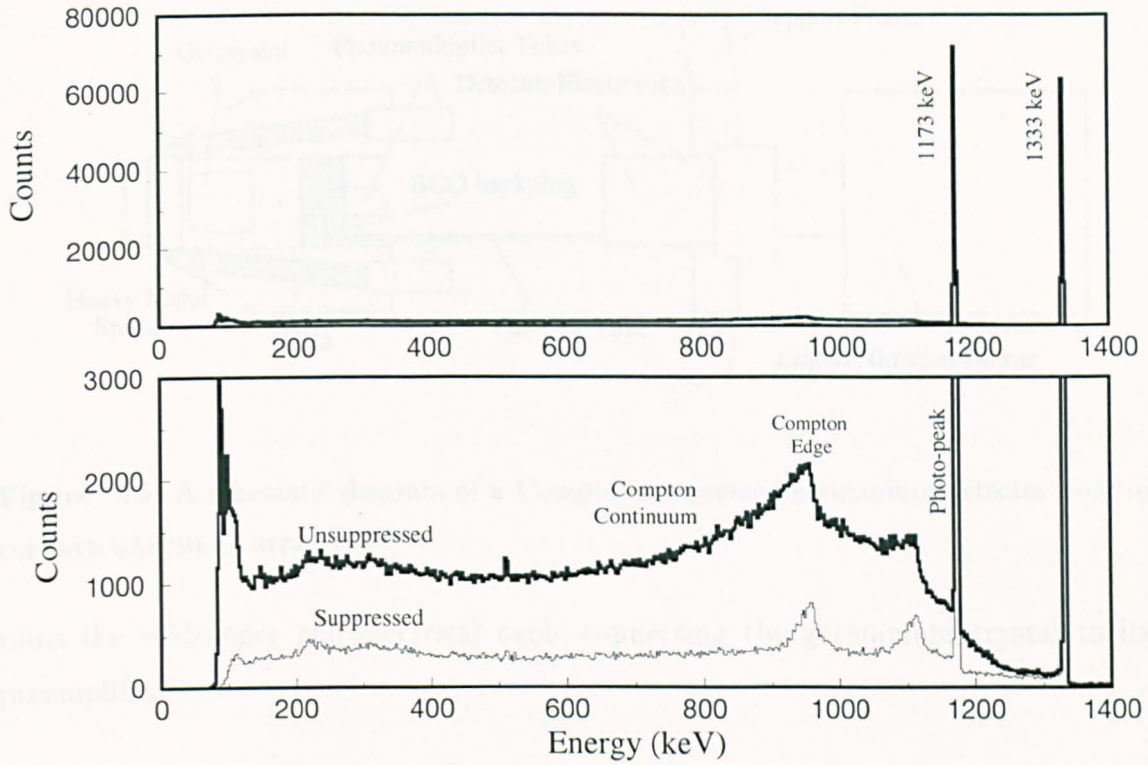

Figure 4.4: The gamma-ray spectra for a ^{60}Co source illustrating the effects of Compton suppression. The thick-line spectrum was obtained with an unsuppressed germanium detector and the thin-line spectrum was acquired with a Compton-suppressed germanium detector.

large as possible. Compton suppression is achieved by surrounding the germanium detector with detectors made from an inorganic-scintillator, usually bismuth germinate $Bi_4Ge_3O_{12}$ (BGO). The BGO detectors detect gamma rays that have Compton scattered from the germanium detector crystal. The coincidence between the signal in the germanium detector and the signal in the BGO detector is then rejected electronically. The good timing properties of BGO suit this application. Also, BGO has a high density (7.3 g/cm^3) and therefore has a high probability of stopping gamma rays so only a small amount of material is required.

Figure 4.5 shows an escape-suppressed HPGe detector used in the GAMMASPHERE array. This arrangement utilises a BGO backplug which is fitted behind the germanium detector to suppress forward-scattered gamma rays. The off-axis tube con-

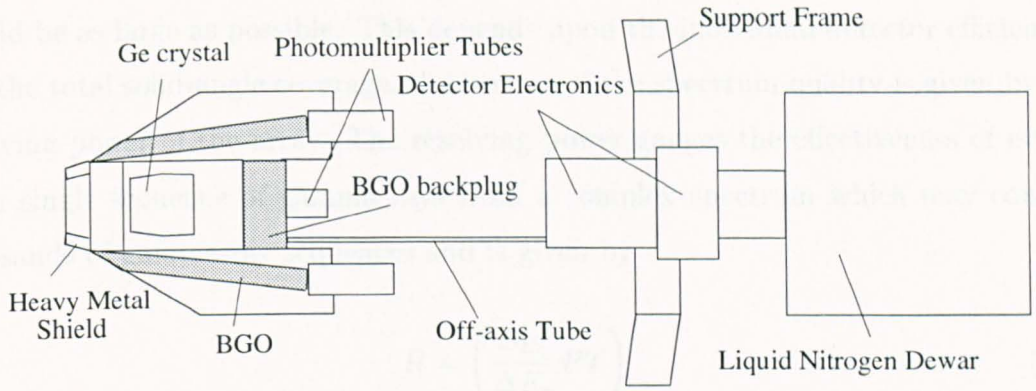

Figure 4.5: A schematic diagram of a Compton-suppressed germanium detector used in the GAMMASPHERE array.

tains the cold-finger and electrical cable connecting the germanium crystal to its preamplifier.

4.5 Germanium-Detector Arrays

Almost all existing germanium-detector arrays utilise BGO-suppressed HPGe detectors. They are designed to measure the properties of, and correlations between, gamma rays in large cascades which depopulate high-spin states. The second generation of germanium-detector arrays contained between twelve and thirty escape-suppressed germanium detectors with individual detector efficiencies of ~25% (relative to a 3 inch × 3 inch NaI(Tl) crystal). These arrays, which included the TESSA arrays [Nolan 85], were optimal for detecting two-fold gamma-ray coincidences. The third generation of germanium-detector arrays were optimised for higher-fold gamma-ray coincidence collection. These arrays include the EUROGAM arrays [Beausang 92], [Beck 92], [Nolan 90], Euroball [Gerl 92] and GAMMASPHERE [Lee 90]. They contain a large number of high-efficiency germanium detectors and include segmented detectors and cluster detectors. The third-generation arrays take advantage of the improvement in selectivity which is gained with high-fold data.

In order to maximise the performance of an array the total photopeak efficiency

should be as large as possible. This depends upon the individual detector efficiencies and the total solid-angle coverage. A measure of the spectrum quality is given by the resolving power of the array. The resolving power gauges the effectiveness of isolating a single sequence of gamma rays from a complex spectrum which may contain thousands of gamma-ray sequences and is given by

$$R = \left(\frac{S_{E_\gamma}}{\Delta E_\gamma} PT \right) \tag{4.8}$$

where ΔE_γ is the energy resolution (FWHM) of gamma rays in the detector spectrum, S_{E_γ} is the average separation of gamma rays in a cascade and PT is the peak-to-total ratio. The major contributing factors to the energy resolution of the system are:

- The intrinsic resolution of the detector, ΔE_{in};
- The Doppler broadening attributed to the detector opening angles, ΔE_D;
- The Doppler broadening attributed to the angular spread of the recoiling nuclei, ΔE_R;
- The Doppler broadening attributed to the velocity spread of the recoiling nuclei, ΔE_V.

These components add in quadrature:

$$\Delta E_\gamma^2 = \Delta E_{in}^2 + \Delta E_D^2 + \Delta E_R^2 + \Delta E_V^2. \tag{4.9}$$

The quantity ΔE_D depends on the size of the detectors used and their distance from the target. The amount of Doppler broadening can be reduced by using a cluster of smaller detectors, especially at 90° angles, thus increasing the *granularity* of the detector. In arrays with high granularity, the total solid angle coverage is made up of many detectors each subtending a small solid angle. The probability of a particular detector being hit by two coincident gamma rays is small in such an array, or equivalently, the *isolated hit probability* is large. An increase in isolated hit probability results in an increase in the PT value of an array.

In order to successfully detect a peak it must stand above the background and be

statistically significant. The minimum intensity of a gamma ray that can be detected by an array is known as the *limit of observation.* The limit of observation of an array, α_0, is dependent upon the total photopeak efficiency, ϵ_{PTOT}, and the resolving power, R. In figure 4.6, α_0 is plotted as a function of the number of coincident gamma rays (fold) for different values of ϵ_{PTOT} and R [Nolan 95]. The limit of observation as a function of resolving power was calculated using the following expression:

$$\left(\frac{N_p}{N_b}\right)_n = \alpha_0(0.76R)^n \tag{4.10}$$

where $\left(\frac{N_p}{N_b}\right)_n$ is the peak-to-background ratio for an n-fold coincidence spectrum. A value of $\left(\frac{N_p}{N_b}\right)_n = 0.2$ was assumed in these calculations. The observational limit as a function of photopeak efficiency was calculated assuming a minimum photopeak intensity of 100 counts, 10^{10} source events and a gamma-ray multiplicity of 30. A spectrum of fold F is obtained by setting F$-$1 gates on 10 transitions in a cascade. The limit of observation due to the resolving power improves rapidly with fold, while the observational limit due to the photopeak efficiency decreases with fold. The position of the second-generation TESSA3 array of sixteen 23%-efficient germanium detectors and 50-element BGO multiplicity filter is marked in the figure. The third-generation full-implementation GAMMASPHERE array of one hundred and ten 75%-efficient germanium detectors is also shown. The TESSA3 array has a resolving power of 9 and a total photopeak efficiency of 0.5%. This gives a limit of observation of 0.1% and an optimum fold of 2. The GAMMASPHERE array has a total photopeak efficiency of 9.4% and a resolving power of 9.4, giving a limit of observation of $5{\times}10^{-3}$% and an optimum fold of 4. That is, GAMMASPHERE has a much greater sensitivity than TESSA3. It is able to observe structures which are populated with much smaller intensities than those which are observable with TESSA3.

The preliminary work in this thesis involved three second-generation germanium-detector arrays. The frame of the TESSA3 array was used with twelve germanium detectors installed, four short of the full complement of sixteen. The Argonne-Notre Dame array of twelve 25%-efficient germanium detectors and the TARDIS array of

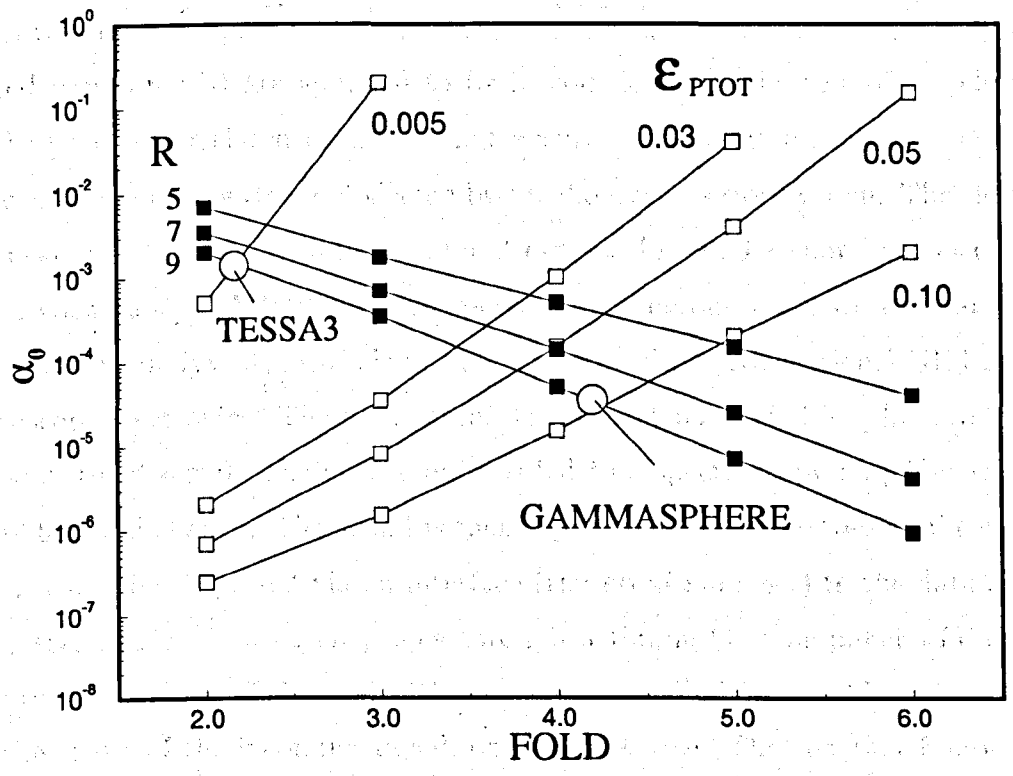

Figure 4.6: The limit of observation of an array as a function of fold for different resolving powers and total photopeak efficiencies.

twelve 23%-efficient germanium detectors were also used. The three arrays have similar properties to the sixteen-detector TESSA3 array. These second-generation arrays were used for mapping population distributions where only two-fold coincidences are required, but the third-generation (GAMMASPHERE) array was used for high-spin spectroscopy of octupole-deformed light-actinide nuclei. Each array is described in more detail in sections 5.1 and 6.1.

4.6 Signal Processing

During the course of this work, several different signal-processing electronic circuits have been utilised, but the general principles which are employed are the same in each case. The underlying philosophy of all gamma-ray coincidence experiments is that

gamma rays detected in different detectors within a small time interval (usually a few hundred nanoseconds) are assumed to be in coincidence. The role of the electronics is to process correlated events so that accurate information such as gamma-ray energy and gamma-ray time is collected by the data acquisition system. The electronics is also used to veto Compton-scattered events. Figure 4.7 shows the electronics setup used with the TARDIS escape-suppressed germanium-detector array at the K-130 laboratory in Jyväskylä, Finland. The system utilises conventional NIM nuclear spectroscopy electronics. The germanium detector output signal is split into an 'energy' and 'time' signal. The energy pulse is fed to a spectroscopy amplifier where it is amplified and shaped. The signal is then input to an analogue-to-digital converter (ADC) before being passed via an interface (the *event manager*) to the data acquisition system. The time signal passes through a timing-filter amplifier (TFA). The TFA provides an amplified signal with fast (nanosecond) timing and is not concerned with the shape of the incoming signal, only its presence. The constant-fraction discriminator (CFD) then rejects signals which are below a certain voltage threshold. This threshold is adjusted so that it is just above noise. The CFD also converts the analogue signal from the TFA into a logic pulse which can be read by the coincidence box. A signal from the BGO suppression shield of the germanium detector is also fed into this coincidence box. If the two signals are in coincidence the event is rejected, or vetoed, and there is no output. To accommodate the poor timing properties of the germanium crystals, the BGO signal is set to be much wider than the germanium signal. Simultaneously, a 'not-busy' signal is required from a spectroscopy (slow) amplifier. This rejects piled-up events, events which include more than one gamma ray arriving in the same detector at the same time. The decision whether to process an event or not is made by the event manager. If there is a signal from the master gate then the event will be processed. The master-gate condition can be changed by adjusting the settings on the multiplicity logic units (MLU). In the TARDIS setup, the units were set to ≥ 2. This means that an event was not processed unless at least two gamma rays were detected in coincidence. Time-to-analogue converter (TAC)

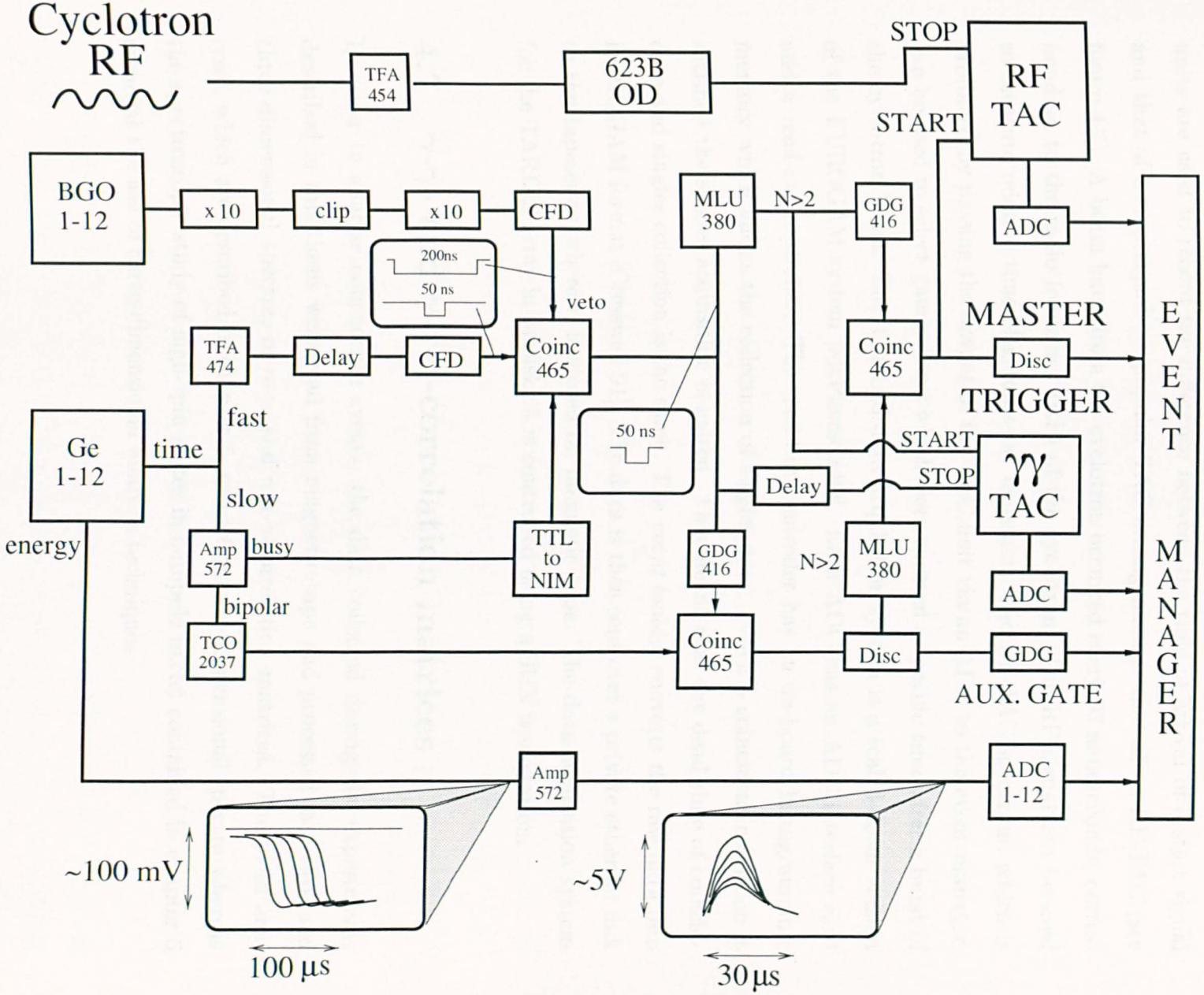

Figure 4.7: A block diagram of the TARDIS electronics.

units are used to record the difference between the time of arrival of a start signal and that of a stop signal. A popular TAC arrangement is that of an RF-TAC (see figure 4.7). A beam burst from the cyclotron occurred every 93 nanoseconds, corresponding to the radio frequency (RF) of the cyclotron. The RF signal can be used to measure relative time of gamma-ray emission. The RF-TAC spectrum, which is produced by passing the output of the TAC unit via an ADC to the event manager, can be used to select gamma rays which were emitted a specific time after a burst of the cyclotron beam. The TARDIS data acquisition system is a scaled-down version of the EUROGAM system [McPherson 92]. Each ADC has an ADC interface card and a *read-out controller*. The read-out controller has an on-board histogramming memory which allows the collection of singles data. When a coincident condition is satisfied the singles acquisition is halted. This means that the dead time of coincidence and singles collection is the same. The *event builder* converts the raw data into EUROGAM format [Cresswell 91]. The data is then sent over a private ethernet link to the tapeserver where it is stored on magnetic tape. The data acquisition system for the TARDIS array in Jyväskylä is controlled using a SUN workstation.

4.7 γ-γ- and γ-γ-γ-correlation matrices

In order to analyse coincidence events, the data collected during the experiments described in this thesis were read from magnetic tape and processed into two- and three-dimensional spectra, or γ-γ- and γ-γ-γ-correlation matrices. The yield analyses, which are described in chapter 5, came from two-dimensional spectra whereas the spectroscopic study of high-spin states in octupole nuclei contained in chapter 6 involved the use of three-dimensional analysis techniques.

γ-γ analysis

Two-dimensional spectra, or γ-γ-correlation matrices, are generated by first decomposing, or unfolding, each n-fold event into ${}_nC_2$ two-fold events. In the data-unfolding process, each m(>n)-fold event is decomposed into $\frac{m!}{(m-n)!n!}$ n-fold events. For example, there are $\frac{4!}{(4-2)!2!} = 6$ two-fold (or double) gamma-ray coincidence events in every four-fold event. Each unfolded two-fold event, representing the the detection of two gamma rays of energy $E_{\gamma 1}$ and $E_{\gamma 2}$ in coincidence, is incremented at $E_{\gamma 1}$, $E_{\gamma 2}$. There is also an increment at $E_{\gamma 2}$, $E_{\gamma 1}$ in order to symmetrise the matrix. If a narrow energy region (called a *gate*) is selected on the x-axis then gamma rays in coincidence with it can be projected onto the y-axis. If the gate is set on a transition in a rotational band, for example, one may observe other members of the rotational band and everything else that is in coincidence with the transition.

γ-γ-γ analysis

Three-dimensional analysis involves the use of γ-γ-γ-correlation matrices or '*cubes*'. This relatively new technique is more suitable for analysing high-fold data and allows the added selectivity of an extra gating condition. In the construction of cubes, each triple gamma-ray coincidence event is incremented at $E_{\gamma 1}$, $E_{\gamma 2}$, $E_{\gamma 3}$. The cube is symmetrised in a similar way to the γ-γ matrix. The extraction of a gamma-ray spectrum from the cube is a two-stage process. The first gate, set on the z-axis, projects a two-dimensional matrix in the $x - y$ plane. The second gate results in the projection of the gamma-ray spectrum. Three-dimensional analysis techniques are a necessary progression in the analysis of high-fold data from third-generation arrays. They were developed as a means of discovering long cascades of gamma rays associated with superdeformed bands.

The analysis of high-fold data in this thesis also involves the use of a gated cube. This was generated from unfolded quadruple gamma-ray coincidence events. When one of the gamma rays in an event passed a gating condition the other three gamma rays in the event were incremented into a cube.

Background Subtraction

Several methods of background subtraction have been used in the course of this work. The method used when studying γ-γ-γ coincidences was to 'define' the background in the total projection spectrum and write it to a file using the gf2 program [Radford 95]. Another method, used in the γ-γ coincidence analyses, was to subtract local background. That is done by taking the spectrum that is in coincidence with the gate and subtracting spectra which are in coincidence with background adjacent to the gate.

Chapter 5

Population of Reflection-Asymmetric Nuclei

5.1 Experimental Details

These experiments had two main objectives: to populate light-actinide nuclei in the octupole region using multinucleon transfer reactions and to obtain yield distributions for the populated nuclei. Three experiments were carried out, in which thick ^{232}Th targets were bombarded by heavy ions at energies just above the Coulomb barrier. The details of the experiments are summarised in table 5.1. Due to the significant target thickness, the effective bombarding energies varied from the incident beam energy down to the Coulomb barrier energy.

5.1.1 ^{56}Fe + ^{232}Th

This reaction was performed at the Accelerator Laboratory of the University of Jyväskylä in Finland. The ^{56}Fe beam was accelerated in charge state 13^+ to an energy of 362 MeV (20% above the Coulomb barrier energy) by the K-130 cyclotron. The beam, which was pulsed with a period of 93 nanoseconds, bombarded a ^{232}Th target of thickness 30 mg/cm^2. The beam was maintained at an intensity of 7-9 enA during

Reaction	Target (mg/cm^2)	Beam			Germanium Detector Array	Facility
		Nucleus	Energy (MeV)	%above CB		
I	^{232}Th (30)	^{56}Fe	362	20	12 TESSA-type (23%-efficient) detectors	K-130 cyclotron, JYFL, Jyväskylä
II	^{232}Th (30)	^{86}Kr	511	16	TESSA3 frame: 12 detectors + 50-element multiplicity filter	K-130 cyclotron, JYFL, Jyväskylä
III	^{232}Th (40)	^{136}Xe	830	15	Argonne–Notre Dame: 12 25%-efficient detectors + 50-element BGO ball	ATLAS, Argonne National Laboratory

Table 5.1: Summary of experimental details. The Coulomb barrier energy was calculated using $R = 1.2(A_p^{1/3} + A_t^{1/3} + 2)$ where A_p and A_t are the mass numbers of the target and projectile, respectively.

the experiment. The TARDIS array of twelve 23%-efficient germanium detectors was employed to collect gamma-ray coincidence events. The TARDIS (Tessa ARray Deployed at ISolde) array was originally designed for deployment at the ISOLDE online isotope separator facility at CERN for the detection of gamma-ray emissions from radioactive-decay products. It contains two rings of six detectors at a distance of 15 cm from the target position with a cone angle of 54.7°, as shown in figure 5.1. The signal processing and data acquisition of the TARDIS array is described in section 4.6. The germanium detector singles count rates were measured to be between 6000 and 8000 counts per second during the experiment. The master gate condition was set to be ≥ 2 suppressed germanium detectors. That is, two or more suppressed germanium-detector signals had to register before an event was processed. After a

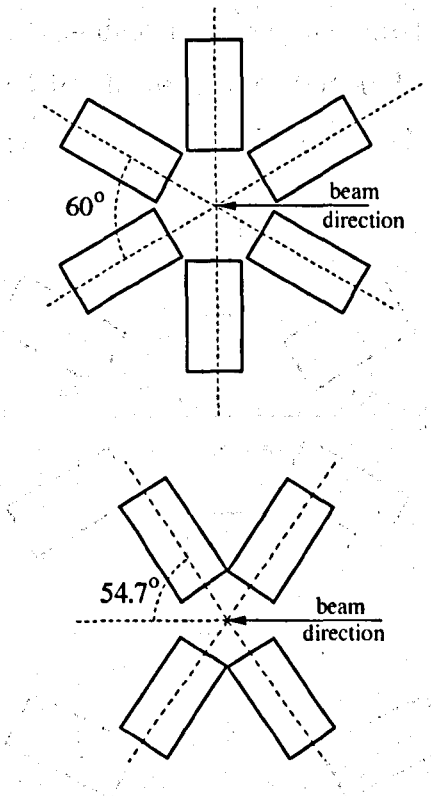

Figure 5.1: Schematic diagram of the germanium detector positions in the TARDIS array.

collection time of 54 hours, 1.1 × 10^8 double and 2.3 × 10^6 triple gamma-ray coincidence events were written to magnetic tape. The average fold of all data was 2.1. Subsequent unfolding of the data revealed a total of 1.9 × 10^8 suppressed double gamma-ray coincidence events. The raw and unfolded data distributions can be seen in figure 5.4(a).

5.1.2 ^{86}Kr + ^{232}Th

This reaction was also performed at the Accelerator Laboratory in Jyväskylä. The ^{86}Kr projectile was accelerated in charge state 18^+ to an energy of 511 MeV (16% above the Coulomb barrier energy). The beam was pulsed with a period of 93 nanoseconds and was delivered at an intensity of 2-4 enA onto a ^{232}Th target of 30 mg/cm^2 thickness. The TESSA3 germanium-detector array frame, which holds up to sixteen germanium detectors, was used. Twelve 23%-efficient germanium detectors were in-

stalled for the experiment. The detectors were mounted in two rings of six at ±19° to the horizontal plane and in planes at 30°, 90° and 150° to the beam direction, as shown in figure 5.2. The array also included a 50-element BGO inner ball. The

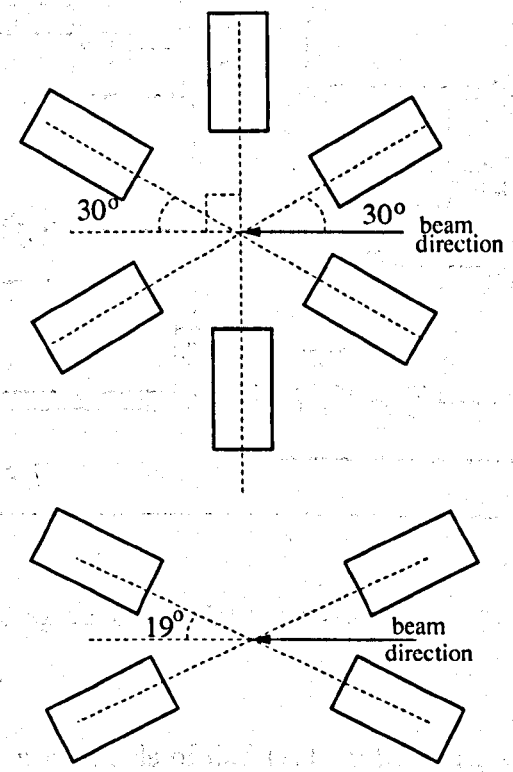

Figure 5.2: Schematic representation of the positions of the 12 germanium detectors in the TESSA3 array.

distance from the target to the germanium detectors was 23 cm and the germanium singles count rates were between 1500 and 2500 counts per second during the experiment. The signal processing for this system is similar to that for the TARDIS system, but the BGO multiplicity filter requires some additional electronics. Fig 5.3 shows the signal-processing electronics for the TESSA3 array with sixteen germanium detectors. The BGO electronics is used to produce 'sum energy' and 'fold' signals. The sum energy signal corresponds to the total energy deposited in the 50-element multiplicity filter. The fold signal corresponds to the number of gamma rays that are detected in coincidence by the device. The spectra which are produced using these signals can be

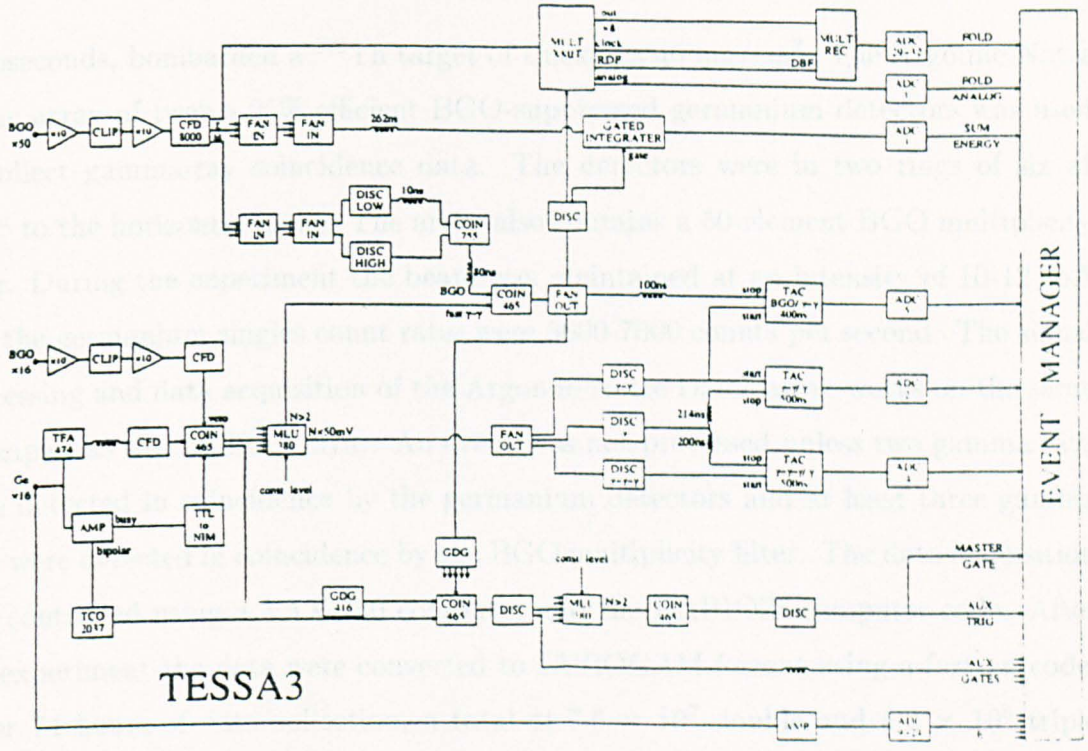

Figure 5.3: Schematic diagram of the signal processing electronics system of the TESSA3 array.

used to separate reaction channels of different multiplicities. The master gate condition was ≥ 2 suppressed germanium detectors. After a collection time of 46 hours, 1.7×10^7 double and 6.1×10^5 triple gamma-ray coincidence events were written to tape. The average fold of these data was 2.03. The number of unfolded double gamma-ray coincidences was 1.9×10^7. The raw and unfolded data distributions can be seen in figure 5.4(b).

5.1.3 ^{136}Xe + ^{232}Th

The third heavy-ion collision experiment was performed at Argonne National Laboratory. The ^{136}Xe beam was accelerated in charge state 38^+ to an energy of 830 MeV (15% above the Coulomb barrier) by the ATLAS (Argonne Tandem Linear Accelerator System) heavy-ion accelerator. The beam, which was pulsed with a period of 82

nanoseconds, bombarded a ^{232}Th target of thickness 40 mg/cm^2. The Argonne-Notre Dame array of twelve 25%-efficient BGO-suppressed germanium detectors was used to collect gamma-ray coincidence data. The detectors were in two rings of six at $\pm 19°$ to the horizontal plane. The array also contains a 50-element BGO multiplicity filter. During the experiment the beam was maintained at an intensity of 10-12 enA and the germanium singles count rates were 5000-7000 counts per second. The signal processing and data acquisition of the Argonne-Notre Dame array works on the same principles as the TESSA3 array. An event was not processed unless two gamma rays were detected in coincidence by the germanium detectors and at least three gamma rays were detected in coincidence by the BGO multiplicity filter. The data acquisition was controlled using a VAX 750 computer and the DAPHNE computer code. After the experiment the data were converted to EUROGAM format using a fortran code. After 74 hours of data collection, a total of 7.6×10^7 double and 4.2×10^6 triple gamma-ray coincidence events were written to tape. The average fold of the raw data was 2.1. A total of 1.0×10^8 double gamma-ray coincidences were obtained after unfolding the data. The raw and unfolded data distributions are shown in figure 5.4(c).

5.2 Data Analysis

The primary aim of the analysis was to discover which of the three systems populated nuclei in the octupole-deformed light-actinide region with the greatest intensity. In order to achieve this, measurements of the yield of the product nuclei were made for each of the three reactions.

Pulsed beams allowed both 'in-beam' and 'out-of-beam' coincidences to be collected in each experiment. For the purposes of the analysis, two γ-γ-correlation matrices were generated for each of the three reactions of table 5.1. An in-beam matrix was produced which contained all γ-γ events. By imposing a delayed time condition on gamma-rays, an out-of-beam matrix was also constructed. The condition on the

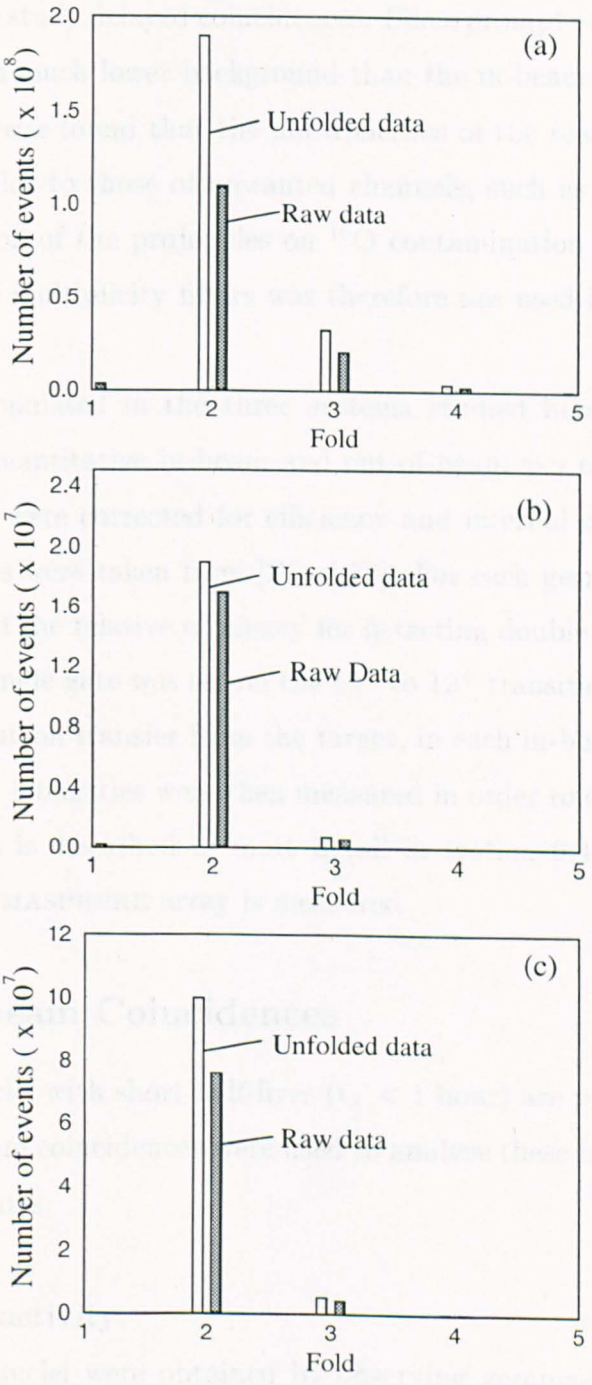

Figure 5.4: The raw and unfolded data distributions for (a) the ^{56}Fe + ^{232}Th reaction, (b) the ^{86}Kr + ^{232}Th reaction and (c) the ^{136}Xe + ^{232}Th reaction.

out-of-beam matrices was 10-80 nanoseconds after a beam burst. The out-of-beam matrices were used to study delayed coincidences. Since prompt events are suppressed, these matrices have a much lower background than the in-beam matrices. Using the multiplicity filters it was found that the multiplicities of the reaction channels of interest were very similar to those of unwanted channels, such as Coulomb excitation and fusion-evaporation of the projectiles on ^{16}O contamination in the targets. The information from the multiplicity filters was therefore not used in the final stages of the analysis.

For the nuclei populated in the three systems studied here, production yields were deduced from quantitative in-beam and out-of-beam γ-γ coincidence analyses, where the intensities were corrected for efficiency and internal conversion. Internal-conversion coefficients were taken from [Rösel 78]. For each germanium-detector array, a measurement of the relative efficiency for detecting double gamma-ray coincidences was made. A single gate was set on the 14^+ to 12^+ transition in ^{230}Th, which is populated by two-neutron transfer from the target, in each in-beam γ-γ matrix. The lower-lying transition intensities were then measured in order to extract the efficiency curves. This process is described in more detail in section 6.4, where the relative efficiency of the GAMMASPHERE array is measured.

5.2.1 Out-of-beam Coincidences

Many radioactive nuclei with short half-lives ($t_{\frac{1}{2}} < 1$ hour) are produced in the three reactions. Out-of-beam coincidences were used to analyse these nuclei and those with low-lying isomeric states.

Short-Lived Radioactivity

The yields of many nuclei were obtained by observing gamma-ray emission following short-lived radioactive decay. In each case the coincident yield for intense pairs of transitions in the daughter nucleus was determined. For specific decay branches, out-of-beam γ-γ coincidence intensities for transitions between non-yrast states were

measured and a yield value for the parent nucleus was calculated by normalising to a 100% decay branch. In some cases this could be done for more than one branch, so several independent yield values were extracted. A weighted mean of consistent yield values was then taken. In some cases the population from preceding decay had to be subtracted. The analysis requires detailed knowledge of the decay scheme of the daughter nucleus. That is, one must know how much of the decay proceeds through the two selected gamma-ray transitions. Level schemes were obtained from the latest Nuclear Data Sheets [NDS].

Figure 5.5 shows the level scheme of ^{78}Se (taken from [NDS 81]). This nucleus

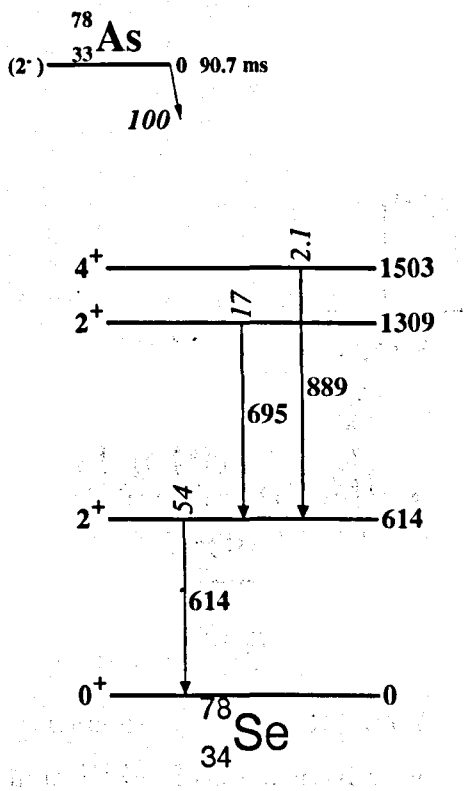

Figure 5.5: Level scheme of ^{78}Se showing the β^- decay of ^{78}As. Taken from reference [NDS 81].

and ^{78}As, which β^- decays to ^{78}Se, are projectile-like products of the ^{56}Fe + ^{232}Th reaction. The yield of ^{78}As was deduced using an out-of-beam matrix. A gate was set on the 614 keV (2^+ to 0^+) transition and the 695 keV gamma-ray peak was in-

tegrated. The intensity was then corrected for the relative efficiency of the TARDIS array. The decay path represents 17% of the total decay of ^{78}As so the coincidence yield was multiplied by $\frac{100}{17}$ in order to obtain the out-of-beam yield.

Nuclei With Isomeric States

Figure 5.6 shows an example of how the yield of a nucleus with a low-lying isomer was determined using out-of-beam coincidences. The figure shows an out-of-beam

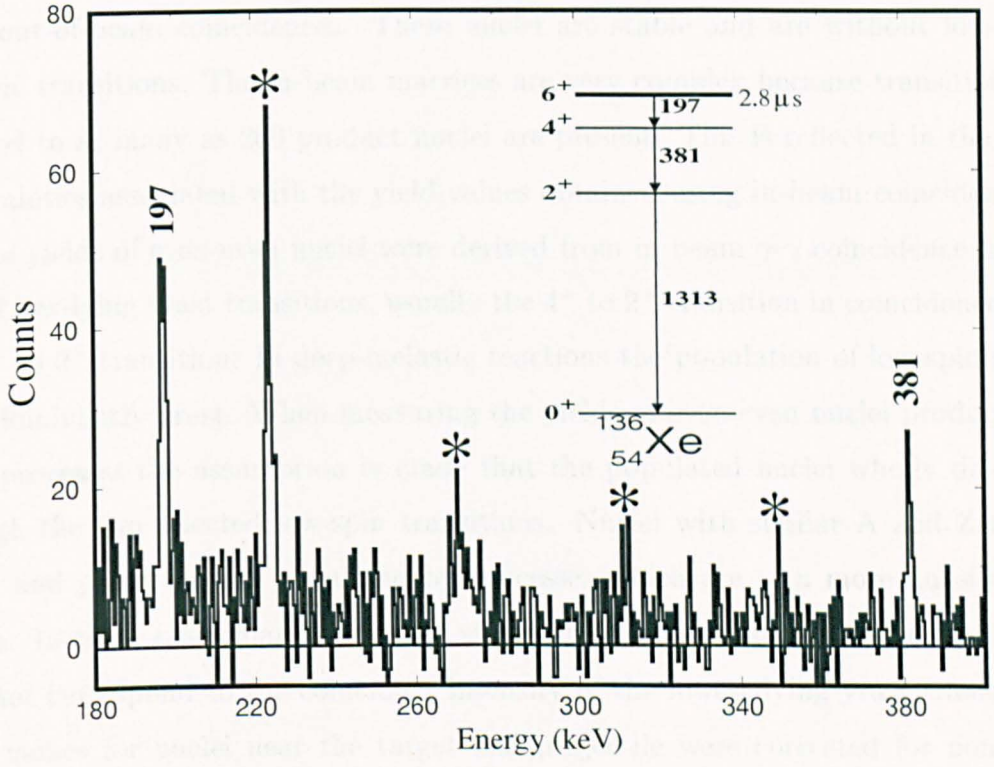

Figure 5.6: Out-of-beam spectrum gated on the 1313 keV (2^+ to 0^+) transition in ^{136}Xe. Peaks that are marked are from ^{136}Xe. Peaks marked with a $*$ are from ^{232}Th which is Coulomb-excited.

spectrum for ^{136}Xe along with a partial level scheme of the nucleus. The nucleus is populated with a low cross-section by fission. The spectrum was produced by gating on the 1313 keV (2^+ to 0^+) transition in the out-of-beam matrix. The low background allows the 4^+ to 2^+ and 6^+ to 4^+ transitions to be observed. Peaks marked with a

* are contaminant lines which are attributed to Coulomb-excited ^{232}Th. Two values of the out-of-beam yield for ^{136}Xe were obtained by integrating the 197 keV and 381 keV gamma-ray peaks and correcting the intensities to compensate for the relative detection efficiency of the TARDIS array.

5.2.2 In-beam Coincidences

The in-beam analysis was applied to products whose yields could not be determined using out-of-beam coincidences. These nuclei are stable and are without low-lying isomeric transitions. The in-beam matrices are very complex because transitions attributed to as many as 200 product nuclei are present. This is reflected in the large uncertainties associated with the yield values obtained using in-beam coincidences.

The yields of even-even nuclei were derived from in-beam γ-γ coincidence intensities of low-lying yrast transitions, usually the 4^+ to 2^+ transition in coincidence with the 2^+ to 0^+ transition. In deep-inelastic reactions the population of low-spin states is predominantly yrast. When measuring the yields of even-even nuclei produced by these processes the assumption is made that the populated nuclei wholly de-excite through the two selected low-spin transitions. Nuclei with similar A and Z to the target and projectile are populated by processes which are of a more quasi-elastic nature. In these cases many non-yrast states are also populated and the total yield does not correspond to the coincident intensity of the lowest-lying yrast transitions. Yield values for nuclei near the target and projectile were corrected for non-yrast population. Figure 5.7 shows an in-beam spectrum of transitions in ^{230}Th which is produced by the transfer of two neutrons from the target to the projectile. Also shown is a partial level scheme for the nucleus. The gate is set on the 6^+ to 4^+ 183 keV transition. The 121 keV 4^+ to 2^+ transition could not be used as a gate as it is contaminated. The total yield does not correspond to the intensity of the 8^+ to 6^+ 238 keV transition, and the intensity of the 5^- to 6^+ and 7^- to 6^+ transitions must also be measured. In order to obtain a yield value for this nucleus the 238 keV, 330 keV and 496 keV peaks were integrated, the three intensities were corrected for

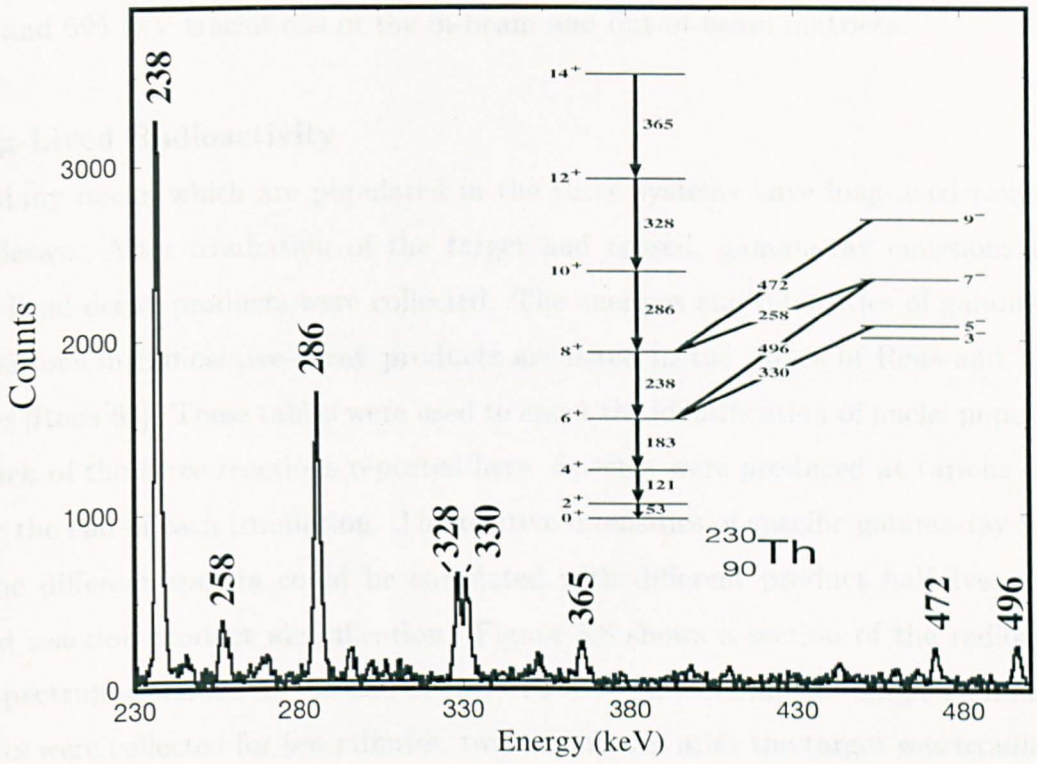

Figure 5.7: In-beam spectrum gated on the 183 keV (6^+ to 4^+) transition in ^{230}Th. Peaks which are marked in the spectrum are from ^{230}Th.

relative efficiency and internal conversion and then summed.

Normalisation

The normalisation factor which enables the direct comparison of in-beam and out-of-beam coincidence intensities was determined by the width of the out-of-beam time window selected from the total time range. This factor was calculated by studying several cases of isomeric decay and gamma-ray emission following radioactive decay for which the intense coincident gamma-ray transitions had no fast in-beam component. The factor was obtained by measuring the coincidence intensity in both the in-beam and out-of-beam matrices. In ^{78}Se (see figure 5.5) it is reasonable to assume that there is negligible in-beam population of the 1309 keV 2^+ level. A value for the normalisation factor was deduced by measuring the coincidence intensity of the 614

keV and 695 keV transitions in the in-beam and out-of-beam matrices.

Long-Lived Radioactivity

Many nuclei which are populated in the three systems have long-lived radioactive decay. After irradiation of the target had ceased, gamma-ray emissions from long-lived decay products were collected. The energies and intensities of gamma-ray transitions in radioactive-decay products are listed in the tables of Reus and Westmeier [Reus 83]. These tables were used to assist the identification of nuclei populated in each of the three reactions reported here. Spectra were produced at various times after the end of each irradiation. The relative intensities of specific gamma-ray peaks in the different spectra could be correlated with different product half-lives which aided reaction-product identification. Figure 5.8 shows a section of the radioactivity spectrum obtained at the end of the ^{56}Fe +^{232}Th experiment. Single gamma-ray events were collected for ten minutes, twenty minutes after the target was irradiated. Characteristic gamma-ray peaks are labelled with the energy of the transition the name of the identified parent nucleus. The 216 keV peak is attributed to a long-lived nucleus which was produced in an in-beam experiment that was performed prior to the ^{56}Fe +^{232}Th experiment.

The yields of many nuclei without low-lying isomers or with complex radioactive decays could not be determined. Also, some determinations were not possible because of contamination. In general, the obtained yield maps were sufficiently complete to give an overall picture of the populated regions of nuclei which are discussed in the next section.

5.3 Results

Figure 5.9(a) shows a section of the total projection of all data collected during the heavy-ion collision study of ^{136}Xe + ^{232}Th. The spectrum is dominated by transitions

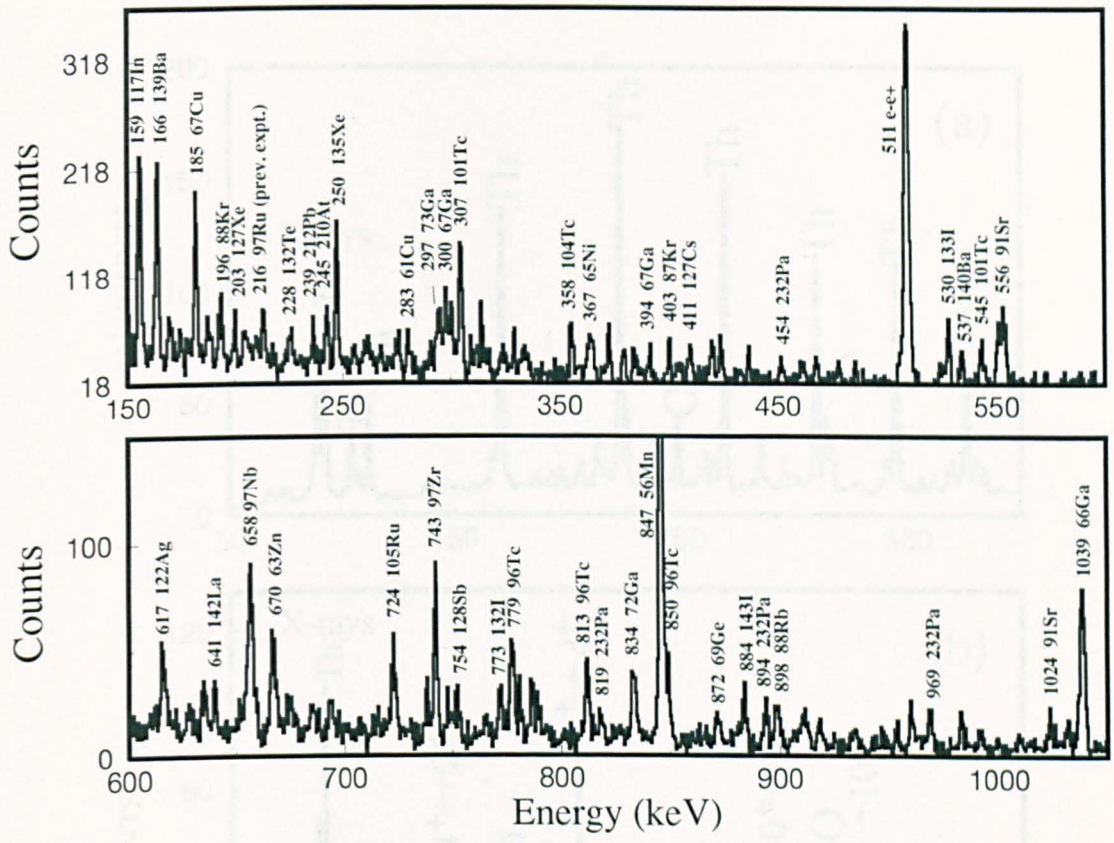

Figure 5.8: A section of the spectrum collected from the radioactive decay of products in the ^{232}Th target after 54 hours of irradiation with the ^{56}Fe beam. Single gamma-ray events were collected for 10 minutes at a time 20 minutes after the beam had been switched off. Products were identified using the gamma rays emitted by the daughter nuclei.

arising from Coulomb excitation (transitions marked 'Th') and fusion-evaporation of ^{136}Xe and ^{16}O in the target (transitions marked 'O'). Figure 5.9(b) shows a typical in-beam spectrum generated from these data. The spectrum shows gamma rays in coincidence with the 8^+ to 6^+ transition in ^{226}Ra. Known gamma-ray transitions in ^{226}Ra and radium X-rays which are in coincidence with the gating transition are identified. Transitions arising from the contaminant processes also appear in the spectrum. Figure 5.10 shows the distribution of target-like nuclei populated in the ^{56}Fe + ^{232}Th reaction. The numbers marked in the figure represent production yields for particular nuclei; those marked with a black dot were recognised in the data set

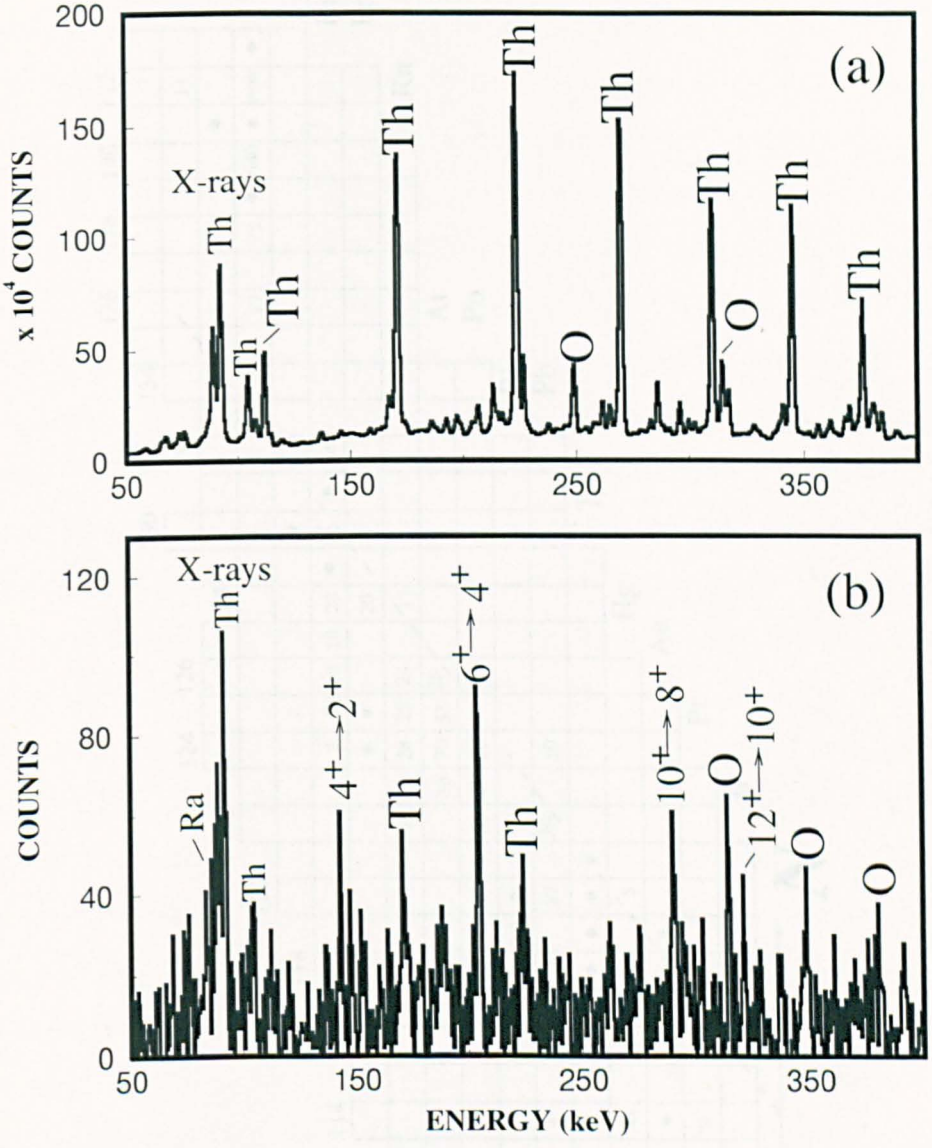

Figure 5.9: (a) Total projection of data collected during the ^{136}Xe + ^{232}Th experiment. The dominant gamma-ray peaks belong to Coulomb-excited ^{232}Th (marked 'Th') and nuclei produced in fusion-evaporation of ^{136}Xe and ^{16}O in the target (marked 'O'). (b) Gamma-ray spectrum showing transitions in ^{226}Ra produced in the ^{136}Xe + ^{232}Th reaction. The spectrum is in coincidence with the 8^+ to 6^+ transition in ^{226}Ra. Transitions from the ground state band in ^{226}Ra are marked in the figure. Contaminant transitions are also present.

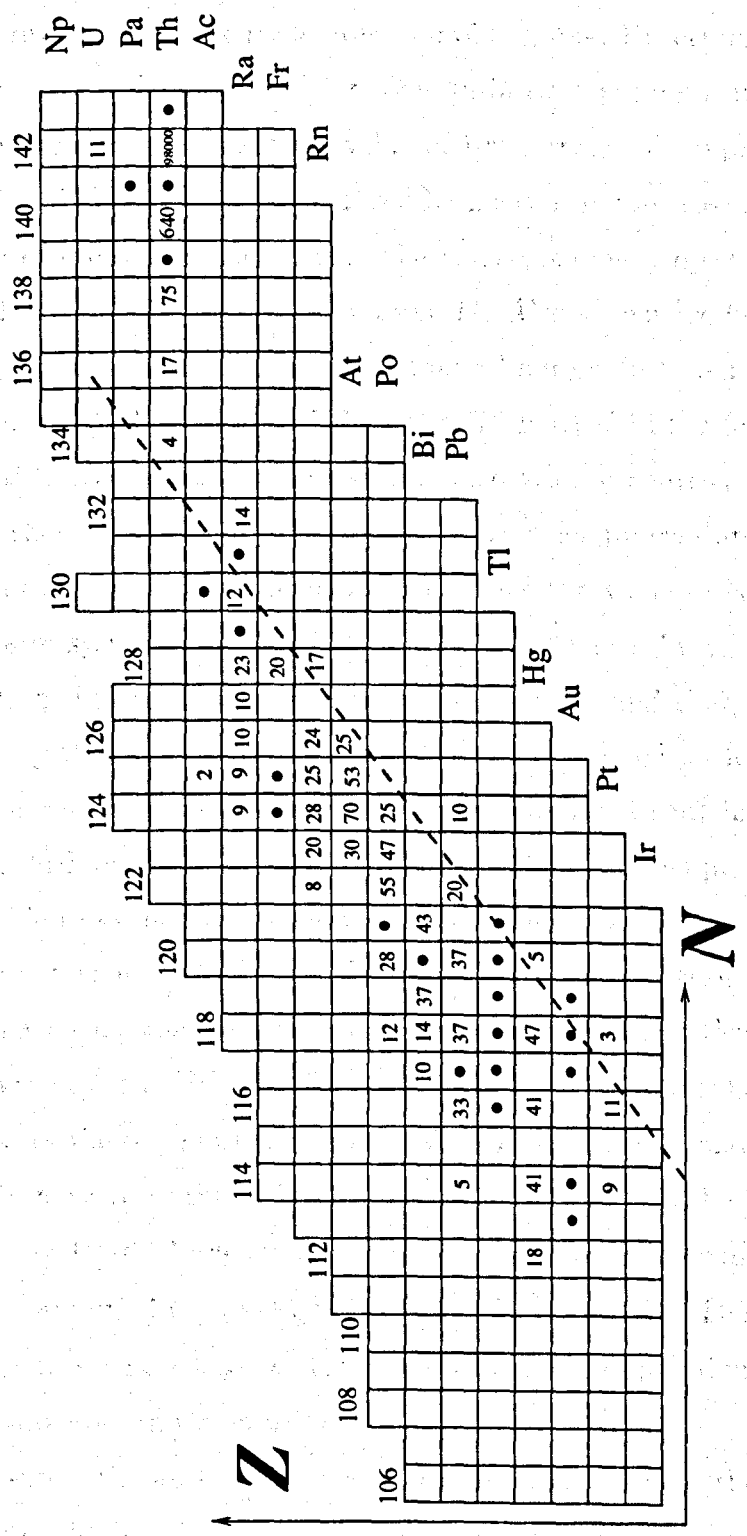

Figure 5.10: Target-like nuclei populated in the ^{56}Fe + ^{232}Th reaction. Numbers marked in the figure represent production yields (a value of 100 approximately corresponds to a cross-section of 1 millibarn). Nuclei marked with black dots were recognised in the data set but yields for these nuclei could not be determined.

but yield measurements for these nuclei were not obtainable. Uncertainties associated with these values are as large as 40% for some in-beam measurements and 25% for the out-of-beam measurements. A yield value of 100 corresponds approximately to a cross-section of 1 millibarn. This was deduced by measuring the cross-section of Coulomb excitation of the 2^+ level in ^{232}Th. The corresponding projectile-like transfer products and their yields are shown in Figure 5.11. Also shown are fission products. Nuclei shaded grey are populated by the compound-nucleus reaction of ^{56}Fe on ^{16}O contamination in the ^{232}Th target and the letter 'P' marked in the figure represents the ^{56}Fe projectile. The solid, thick, black line displays the neutron-rich edge of β-stability which shows that many products of the transfer process are neutron-rich. The dashed lines on figure 5.10 and figure 5.11 mark the value of N/Z of the ^{56}Fe + ^{232}Th composite system ($= \frac{288}{116}$). The population of nuclei by the deep-inelastic transfer of nucleons in this system is dictated by the mass and charge equilibration processes, whereby the neutron-to-proton ratio of the populated nuclei tends to that of the composite system [Freiesleben 84]. One may observe a shift in population to the left of the dashed lines due to neutron evaporation from excited primary products.

It is reasonable to assume that most of the yield for the nuclei in the $32 \lesssim Z \lesssim 60$ region arises from fission. For these products the extracted yields of nuclei deduced from out-of-beam measurements were found to be systematically three times larger than those for even-even nuclei obtained from in-beam measurements. No such discrepancy existed in the region of the transfer products. It is reasonable to conclude from this that in measuring the in-beam coincidence intensity of the low-lying yrast transitions (usually 4^+ to 2^+ and 2^+ to 0^+) we are neglecting approximately $\frac{2}{3}$ of the production cross-section of even-even nuclei in the fission region. This suggests that the fission products are populated at low spin, with direct population of the ground or first excited states being the most common excitation path.

Figure 5.12 shows the mass distribution of nuclei populated in the ^{56}Fe + ^{232}Th reaction. This was obtained by summing production yields for each mass number and performing a linear interpolation between values for isobars with yields that were un-

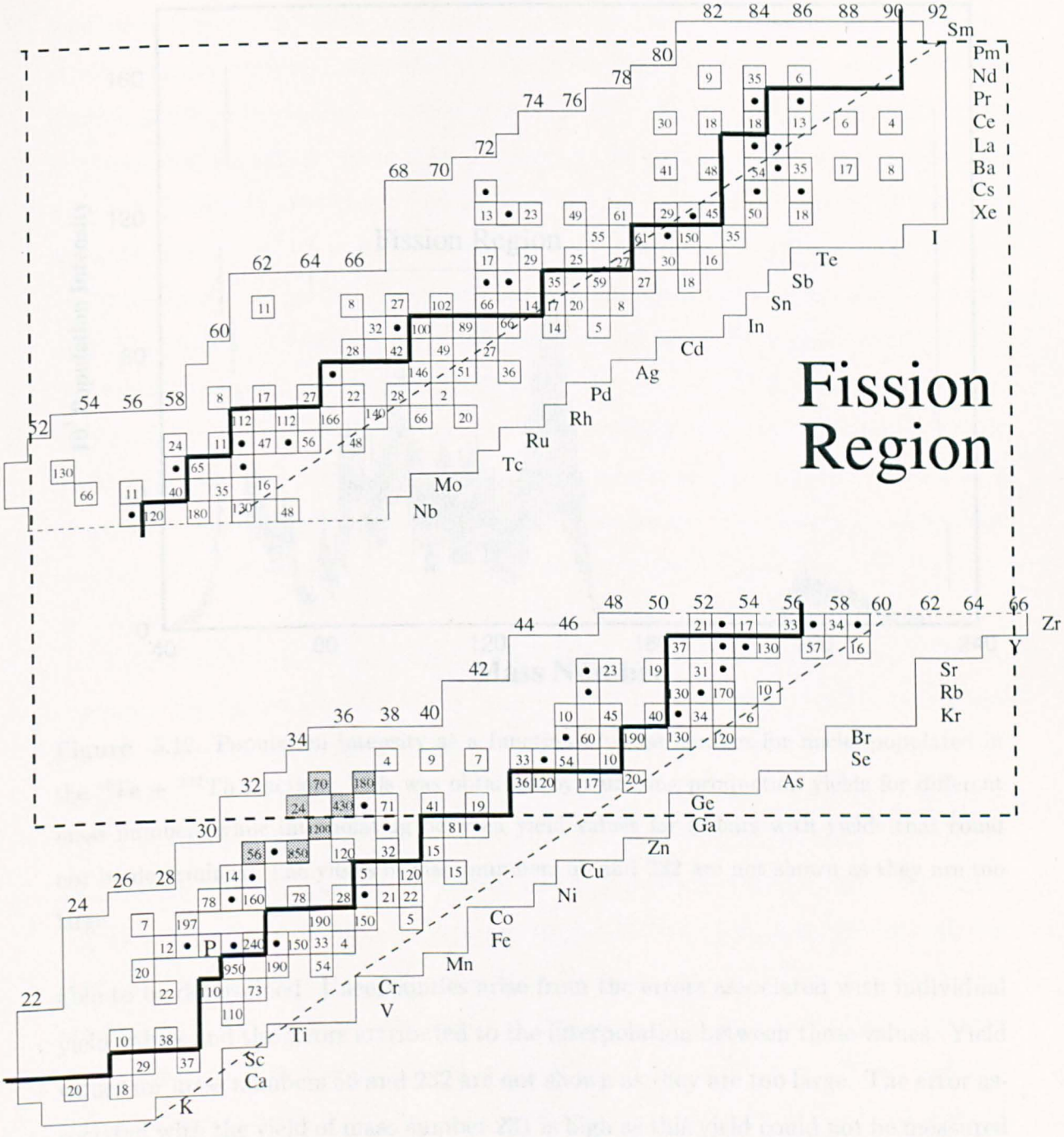

Figure 5.11: Projectile-like products of the ^{56}Fe + ^{232}Th reaction. Also shown (in the 32 $\lesssim$ Z $\lesssim$ 60 region) are the products of fission. The solid, thick, black line in the figure marks the neutron-rich edge of β-stability indicating that many products of transfer processes are neutron-rich. The letter 'P' marks the position of the ^{56}Fe projectile. Nuclei shaded grey are populated by fusion-evaporation of ^{56}Fe and ^{16}O contamination in the ^{232}Th target.

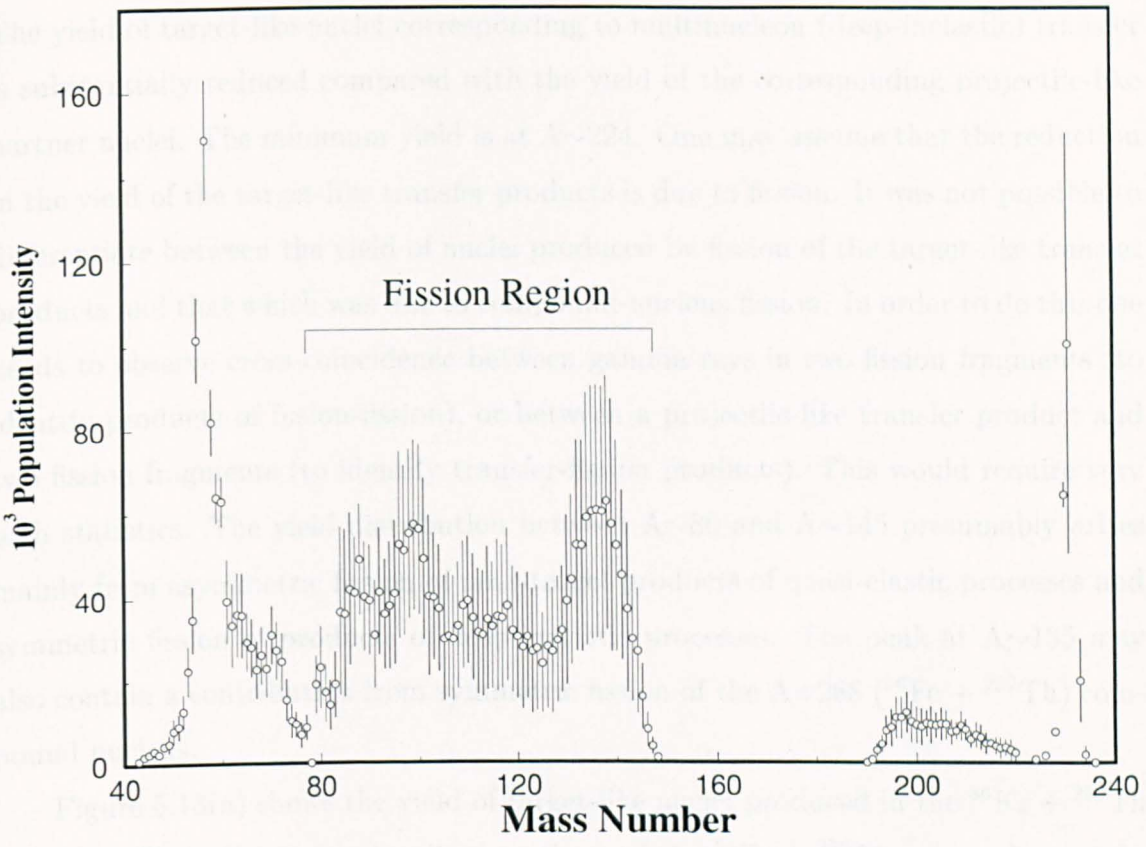

Figure 5.12: Population intensity as a function of mass number for nuclei populated in the ^{56}Fe + ^{232}Th reaction. This was obtained by summing production yields for different mass numbers while interpolating between yield values for isobars with yields that could not be determined. The yields of mass numbers 56 and 232 are not shown as they are too large.

able to be determined. Uncertainties arise from the errors associated with individual yield values and the errors attributed to the interpolation between these values. Yield values for mass numbers 56 and 232 are not shown as they are too large. The error associated with the yield of mass number 231 is high as this yield could not be measured and there is a large uncertainty associated with the interpolation between the yields of ^{230}Th and ^{232}Th. The yields of even-even nuclei in the fission region were multiplied by three. Near the projectile and target we can see a significant yield of nuclei which are presumably produced by the transfer of neutrons in quasi-elastic processes.

The yield of target-like nuclei corresponding to multinucleon (deep-inelastic) transfer is substantially reduced compared with the yield of the corresponding projectile-like partner nuclei. The minimum yield is at A$\sim$224. One may assume that the reduction in the yield of the target-like transfer products is due to fission. It was not possible to differentiate between the yield of nuclei produced by fission of the target-like transfer products and that which was due to compound-nucleus fission. In order to do this one needs to observe cross-coincidence between gamma rays in two fission fragments (to identify products of fusion-fission), or between a projectile-like transfer product and two fission fragments (to identify transfer-fission products). This would require very high statistics. The yield distribution between A$\sim$80 and A$\sim$145 presumably arises mainly from asymmetric fission of near-target products of quasi-elastic processes and symmetric fission of products of deep-inelastic processes. The peak at A$\sim$135 may also contain a contribution from symmetric fission of the A=288 (^{56}Fe + ^{232}Th) compound nucleus.

Figure 5.13(a) shows the yield of target-like nuclei produced in the ^{86}Kr + ^{232}Th reaction. The values are normalised to those of the ^{56}Fe + ^{232}Th system by matching the yields of the Coulomb-excited 2^+ states in ^{232}Th. Figure 5.13(b) shows the target-like nuclei produced in the heavy-ion collision ^{136}Xe + ^{232}Th along with their normalised population intensities. In both population distributions solid, thick, black lines display the boundary of population by compound-nucleus reactions with stable beams and targets. In both systems we see significant yield of nuclei beyond this boundary and we have observed radium and radon isotopes which are predicted to be octupole deformed but are only known at low spin. As there was very little existing data on ^{222}Ra it was not recognised in these data but, as ^{220}Ra and ^{224}Ra were observed in both systems, we expect that it is populated. As in the ^{56}Fe + ^{232}Th system, the population of nuclei by deep-inelastic transfer is governed by the mass and charge equilibration processes. The shift in population to lower mass due to neutron evaporation is also observed in both these systems. Production yields for projectile-like transfer products are not shown for the ^{86}Kr + ^{232}Th and ^{136}Xe + ^{232}Th systems as

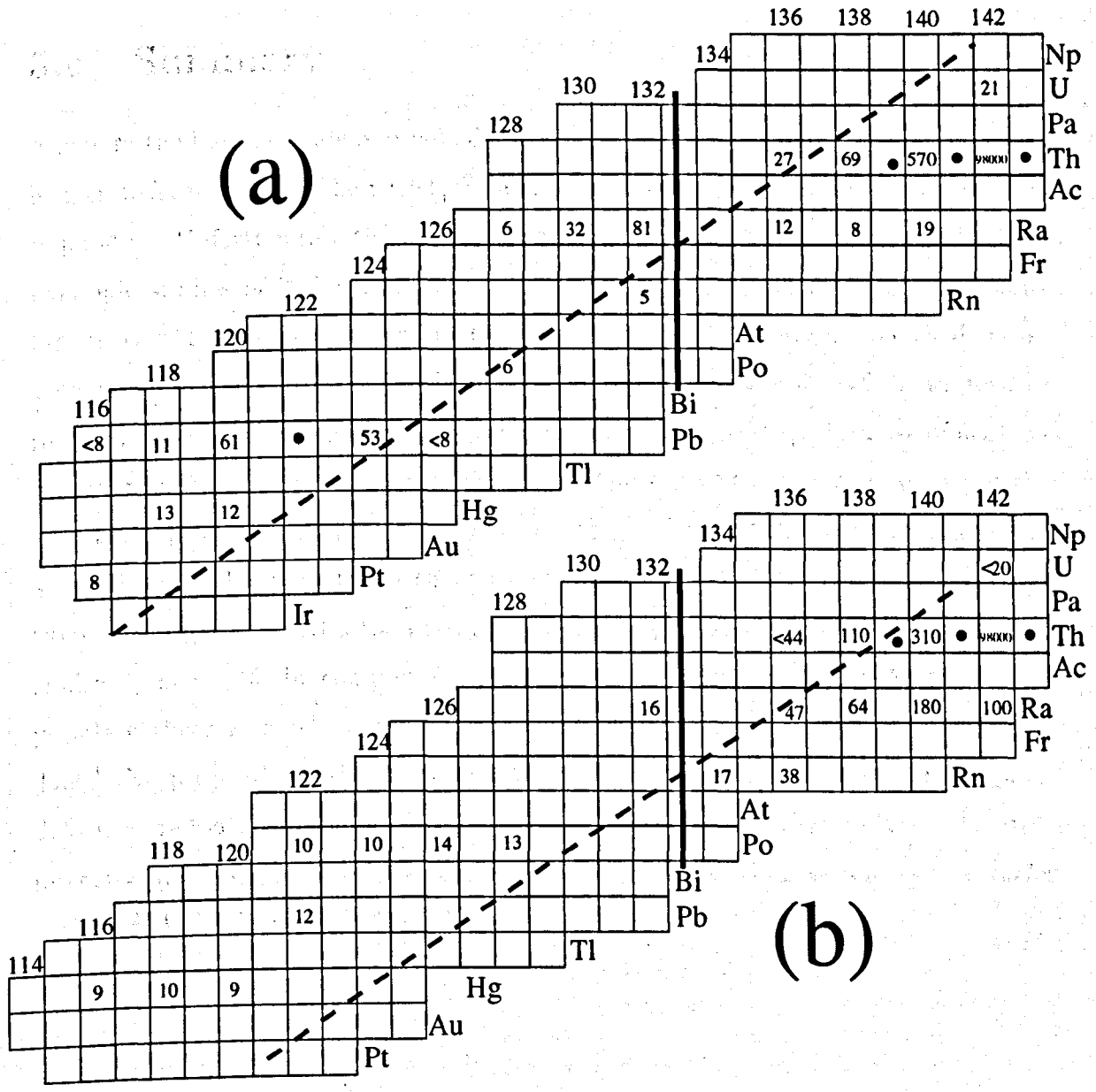

Figure 5.13: Target-like products of (a) the ^{86}Kr + ^{232}Th reaction and (b) the ^{136}Xe + ^{232}Th reaction. The solid, thick, black line marked in both reaction product distributions indicates the boundary of populating the light-actinide region using fusion-evaporation reactions with stable beams and targets.

the yields of these nuclei are obscured by those of nuclei populated by fission.

5.4 Summary

Nuclei in the light-actinide octupole-deformed region were populated using multinucleon transfer reactions. The nuclei ^{220}Rn and ^{222}Rn were identified and ^{222}Ra was also populated. Unfortunately the acquired statistics were not sufficient to enable spectroscopic studies of high-spin states in these nuclei. The production cross-sections for individual nuclei are rather low (~100 microbarns) and production yield measurements indicate that there is substantial competition from fission of the target-like reaction partner. There is also large fractionation of these systems because of neutron evaporation from primary reaction products. Figure 5.14 shows a summary of the target-like product yields for the reactions ^{56}Fe + ^{232}Th, ^{86}Kr + ^{232}Th and ^{136}Xe + ^{232}Th. The least neutron-rich of the projectiles, ^{56}Fe, picks up most neutrons from the target and shifts the distribution of heavy products into the region which is already accessible by compound-nucleus reactions. The ^{86}Kr and ^{136}Xe projectiles populate the region which cannot be accessed using fusion-evaporation reactions. The ^{136}Xe projectile, with the largest neutron-to-proton ratio, populates octupole-deformed radon and radium isotopes in the light-actinide region with the greatest intensity and provides the best opportunity to study previously inaccessible nuclei such as ^{222}Ra, ^{220}Rn and ^{222}Rn.

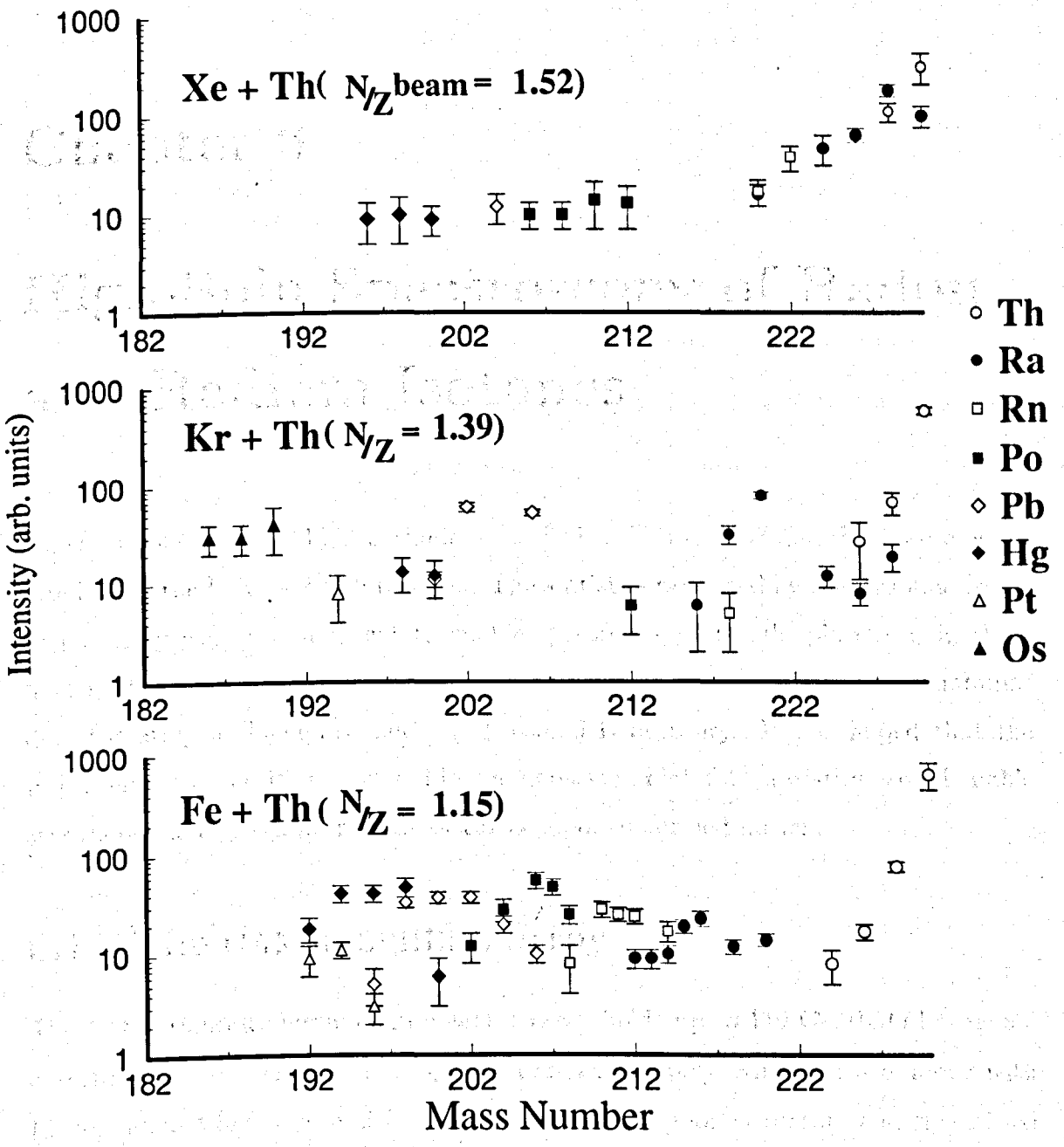

Figure 5.14: A comparison of the yields of target-like nuclei produced in the ^{56}Fe + ^{232}Th, ^{86}Kr + ^{232}Th and ^{136}Xe + ^{232}Th reactions.

Chapter 6

High-Spin Spectroscopy of Radon and Radium Isotopes

The octupole-deformed light-actinide nuclei ^{220}Rn, ^{222}Rn, ^{222}Ra and ^{224}Ra were populated using the ^{136}Xe + ^{232}Th reaction. The statistics produced by the Argonne-Notre Dame array were not sufficient to enable spectroscopy of high-spin states in these nuclei. The reaction was therefore repeated using the GAMMASPHERE germanium-detector array at Lawrence Berkeley National Laboratory. It was hoped that the improvement in sensitivity, offered by an increase in high-fold statistics, would enable studies of the high-spin structure of the octupole-deformed nuclei.

6.1 The GAMMASPHERE array

The GAMMASPHERE germanium-detector array holds up to 110 Ge/BGO hexagonal detector modules. These modules tile a 122-element polyhedron surface, along with 12 pentagons which are used for beam access, the support structure and specialised detectors. A close-up photograph of the array with one quarter of the detectors installed is shown in figure 6.1. At the time of the experiment the array consisted of 73 high-purity BGO-suppressed germanium detectors [Baxter 92], [Carpenter 94], 28 of which were segmented [Macchiavelli 94]. The specifications of the array are

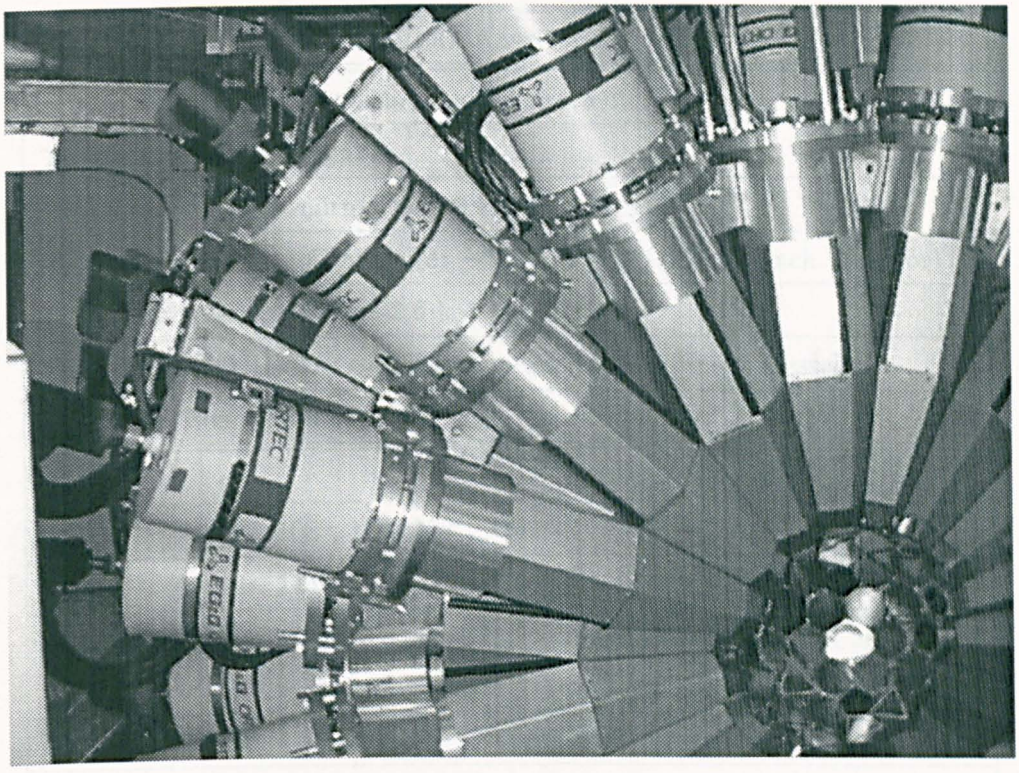

Figure 6.1: The GAMMASPHERE array.

summarised in table 6.1.

6.1.1 Signal Processing and Data Acquisition

The GAMMASPHERE signal-processing system works on the same principles as that of the TARDIS array which is described earlier in this work (see section 4.6). The large number of channels involved, however, renders the use of NIM electronics impractical. The GAMMASPHERE system is based on the VXI bus (VME eXtension for Instrumentation) standard. The standard uses electronic cards which contain high-density analogue signal processing and digital circuitry. A block diagram of the electronics for the full-implementation GAMMASPHERE array is shown in figure 6.2. The VXI crates host the front-end electronics with electronic cards for the detector modules. There are six VXI crates which each contain the electronics to process the signals from nine or ten detector modules. The Ge and BGO electronics are on the

GAMMASPHERE Array Specifications[1]	
N°. of detectors: 45 normal and 28 segmented	
Type: high-purity n-type	
Efficiency: ~78%[2] normal and ~75%[2] segmented	
Total Solid-Angle Coverage: ~30.5%[2] (~0.418% for each detector)	
Detector Resolution[3]: ~2.6 keV	
Peak-to-Total Ratio: ~55% suppressed, ~25% unsuppressed	
Detector Positions:	
θ	ϕ
31.7°	36°, 108°, 180, 252°, 324°
37.4°	72°, 144°, 216°, 288°, 360°
50.1°	22.8°, 49.2°, 94.8°, 121.2°, 166.8°, 193.2°, 238.8°, 265.2°, 310.8°, 337.2°
58.3°	72°, 144°*, 216°
69.8°	53.5°*, 125.5°, 197.5°*, 234.5°*, 306.5°*
79.2°	144°*, 216°*, 360°*
80.7°	36°*
90.0°	54°, 126°*, 162°*, 198°*, 234°*, 306°*
99.3°	144°*, 216°*, 360°*
100.8°	36°*
110.2°	17.5°*, 161.5°
121.7°	36°, 108°*, 180°*, 252°*, 324°*
129.9°	13.2°, 58.8°, 85.2°, 130.8°, 157.2°*, 202.8° , 229.2°*, 274.8°*, 301.2°*, 346.8°*
142.6°	36°, 108°, 180°, 252°, 324°
148.3°	72°, 144°, 216°, 288°, 360°
162.7°	36°, 108°, 252°, 324°

Table 6.1: The GAMMASPHERE germanium-detector array specifications. The superscripts are described as follows: [1] 17-20th November 1995; [2] relative to a 3 inch × 3 inch NaI(Tl) crystal; [3] FWHM for 1.33 MeV gamma rays; * segmented detectors.

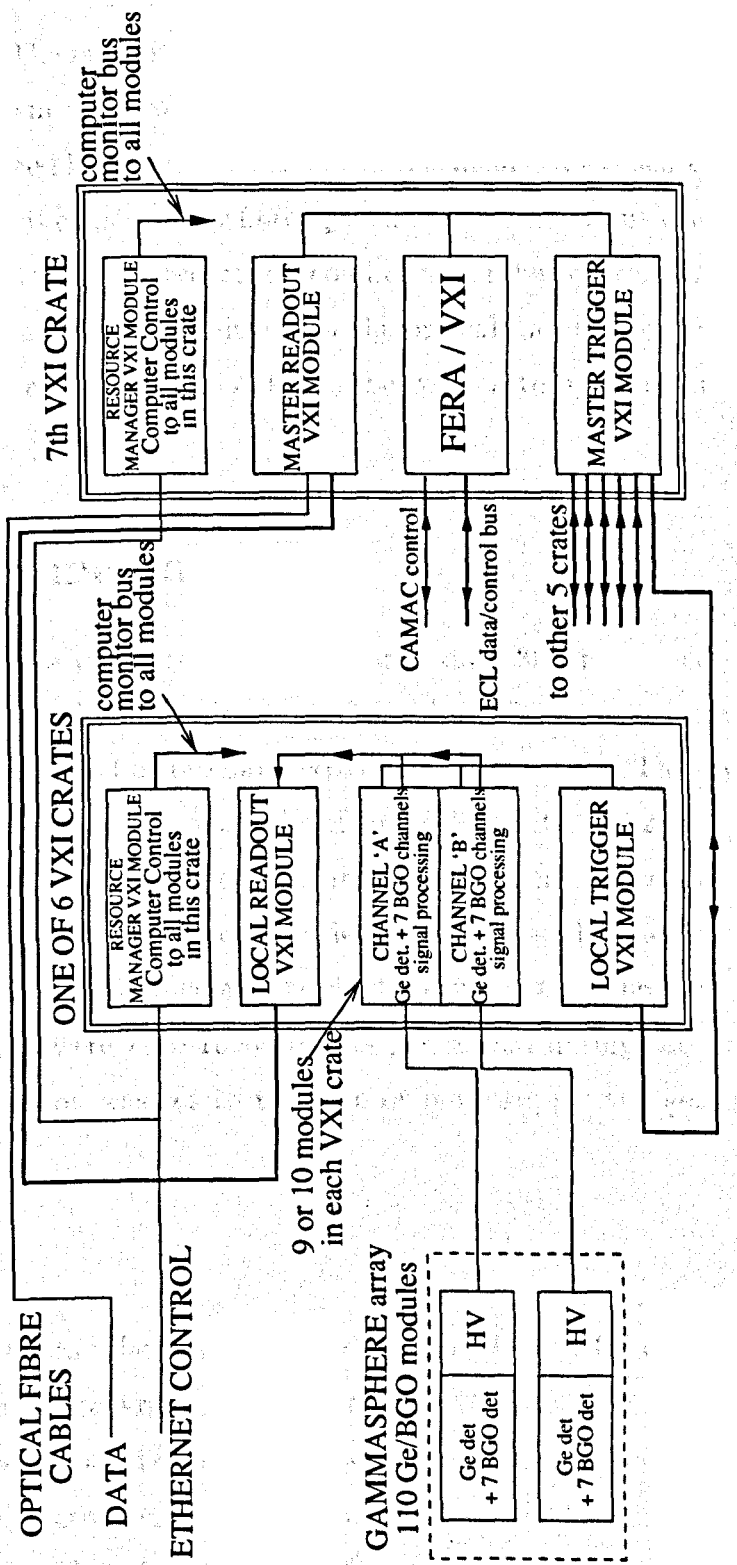

Figure 6.2: Block diagram of the GAMMASPHERE signal-processing electronics.

same VXI card. The master trigger, histogrammer, event builder and the data storage interface system are also contained on electronic cards. The Ge and BGO high voltages are supplied by an interface unit which is attached to each Ge/BGO module. The whole system is connected by fibre-optic link to workstations where the electronic parameters, such as the master trigger condition, can be controlled. Structured data from the event builder is transmitted via the optical link to the tapeserver where it is stored on magnetic tape. The data can be written to up to eight magnetic tapes simultaneously.

6.2 Experimental Details

The ^{136}Xe projectile was accelerated in charge state 30^+ to an energy of 833 MeV (16 % above the Coulomb barrier energy) by the 88" cyclotron. The beam, which was pulsed with a period of 180 nanoseconds, bombarded a ^{232}Th target of thickness 36 mg/cm^2. The beam was maintained at an intensity of 12-14 enA throughout the experiment. Copper and tantalum absorbers of total thickness $\frac{5}{1000}$ inches were placed on the front of the germanium detectors to absorb unwanted xenon X-rays which would unnecessarily increase the singles count rates. The germanium-detector singles count rates were 7000-10000 counts per second during the experiment. The master gate condition was set to be three or more suppressed germanium-detector signals.

6.2.1 Data

After 49 hours of data collection, 1.4×10^9 triple and 6.0×10^8 quadruple gamma-ray coincidence events were written to magnetic tape. The average fold of these data was 3.7. The raw and unfolded data distributions can be seen in figure 6.3. Unfolding the high-fold events greatly increases the amount of lower-fold statistics. After unfolding, there were 1.1×10^{10} triple and 6.8×10^9 quadruple gamma-ray coincidence events. It is interesting to compare these statistics with those obtained for the same reaction

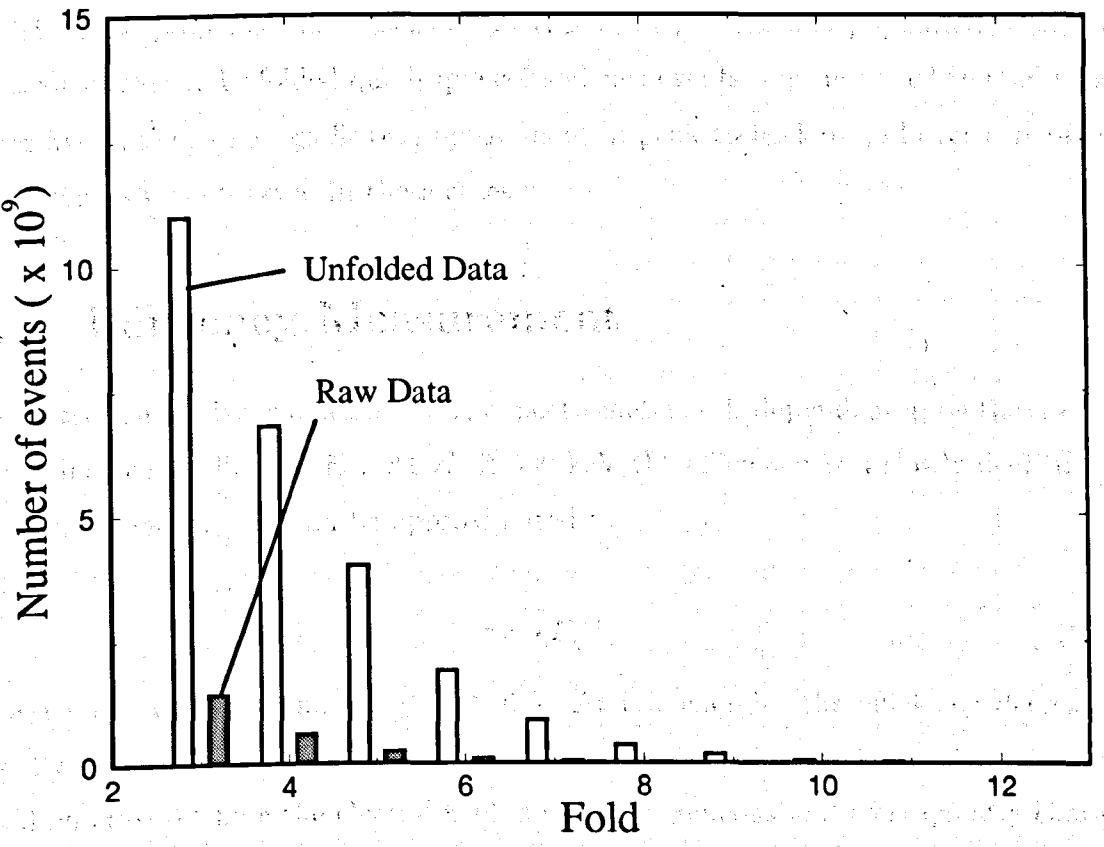

Figure 6.3: Raw and unfolded data distributions for the ^{136}Xe + ^{232}Th reaction using the GAMMASPHERE array.

with the Argonne-Notre Dame array at Argonne National Laboratory. With the GAMMASPHERE array, 2000 times more unfolded triple and 30000 more unfolded quadruple gamma-ray coincidences were collected.

6.3 Data Analysis

The data were read into γ-γ-γ-correlation matrices or 'cubes' (see section 4.7). The first, which shall be referred to as the 'ungated cube', contained all the unfolded triple gamma-ray coincidences with no gating condition applied. The second, the '^{224}Ra-gated cube', was incremented if any gamma-ray in an unfolded four-fold event passed an energy gate on the 4^+ to 2^+ (166.5 keV) transition in ^{224}Ra. Of the six

nuclei whose properties are discussed in this thesis, ^{224}Ra was populated with the greatest intensity. Unfolded quadruple coincidence events were not used to study the other five nuclei as no significant improvement in peak-to-background over three-fold coincidences was observed in these cases.

6.4 Efficiency Measurement

The detection efficiency of a gamma-ray spectrometer, ε, is dependent upon the energy of the incident radiation, E_γ. At $E_\gamma \gtrsim 300$ keV the efficiency is a slowly-decreasing function of energy that can be approximated to

$$\varepsilon = cE_\gamma^{-x} \tag{6.1}$$

where c is a constant and $0.5 \leq x \leq 0.6$. At low energies the efficiency decreases rapidly because low-energy gamma-rays are stopped quickly in the front of the germanium crystal where the electric field is not homogeneous and consequently charge collection is poor. Also, the efficiency for detecting coincidences is lower than that for single events at low gamma-ray energies. The low-energy events can fall outside the coincident time window because their smaller rise time means the electronic processing is less reliable than for those with energies above 200 keV. This effect necessitates the use of coincidence data in efficiency measurements.

Figure 6.4 shows an efficiency measurement of the GAMMASPHERE array. The solid curve shows the relative efficiency for detecting single gamma-ray events. This was produced by placing ^{56}Co, ^{133}Ba, ^{152}Eu, ^{182}Ta and ^{243}Am sources in the target position after the in-beam experiment. Transition intensities were measured in the singles spectra and were compared with the known actual relative intensities using the EFFIC Oak Ridge computer code. The dashed curve shows the relative efficiency for detecting triple gamma-ray coincidence events. This was produced using transitions in the ground state rotational band in ^{230}Th. A double-gate was placed on the 18^+ to 16^+ and 16^+ to 14^+ transitions in the ungated cube and the intensities of the

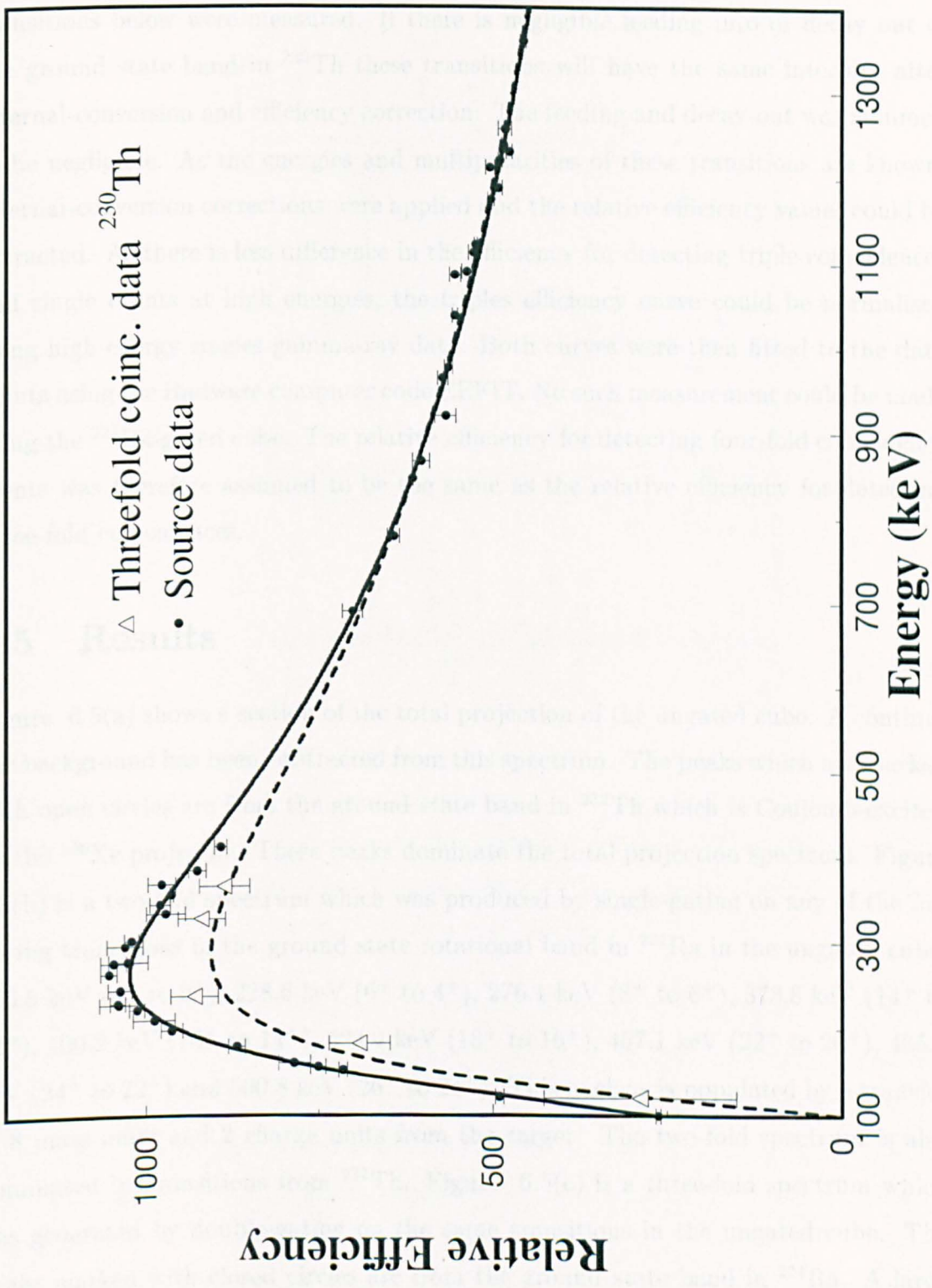

Figure 6.4: Efficiency curves for the GAMMASPHERE array with 73 large HPGe detectors, 28 of which are segmented (see section 4.3). The solid curve is produced from singles data and the dashed curve is from triple gamma-ray coincidence events.

transitions below were measured. If there is negligible feeding into or decay out of the ground state band in ^{230}Th these transitions will have the same intensity after internal-conversion and efficiency correction. The feeding and decay-out was assumed to be negligible. As the energies and multipolarities of these transitions are known, internal-conversion corrections were applied and the relative efficiency values could be extracted. As there is less difference in the efficiency for detecting triple coincidences and single events at high energies, the triples efficiency curve could be normalised using high-energy singles gamma-ray data. Both curves were then fitted to the data points using the Radware computer code EFFIT. No such measurement could be made using the ^{224}Ra-gated cube. The relative efficiency for detecting four-fold coincidence events was therefore assumed to be the same as the relative efficiency for detecting three-fold coincidences.

6.5 Results

Figure 6.5(a) shows a section of the total projection of the ungated cube. A continuous background has been subtracted from this spectrum. The peaks which are marked with open circles are from the ground state band in ^{232}Th which is Coulomb-excited by the ^{136}Xe projectile. These peaks dominate the total projection spectrum. Figure 6.5(b) is a two-fold spectrum which was produced by single-gating on any of the following transitions in the ground state rotational band in ^{224}Ra in the ungated cube: 166.5 keV (4^+ to 2^+), 228.6 keV (6^+ to 4^+), 276.1 keV (8^+ to 6^+), 373.8 keV (14^+ to 12^+), 400.2 keV (16^+ to 14^+), 424.4 keV (18^+ to 16^+), 467.1 keV (22^+ to 20^+), 485.1 keV (24^+ to 22^+) and 500.8 keV (26^+ to 24^+). This nucleus is populated by a transfer of 8 mass units and 2 charge units from the target. The two-fold spectrum is also dominated by transitions from ^{232}Th. Figure 6.5(c) is a three-fold spectrum which was generated by double-gating on the same transitions in the ungated cube. The peaks marked with closed circles are from the ground state band in ^{224}Ra. A large increase in the selectivity of the transfer-reaction channel is observed when three-fold

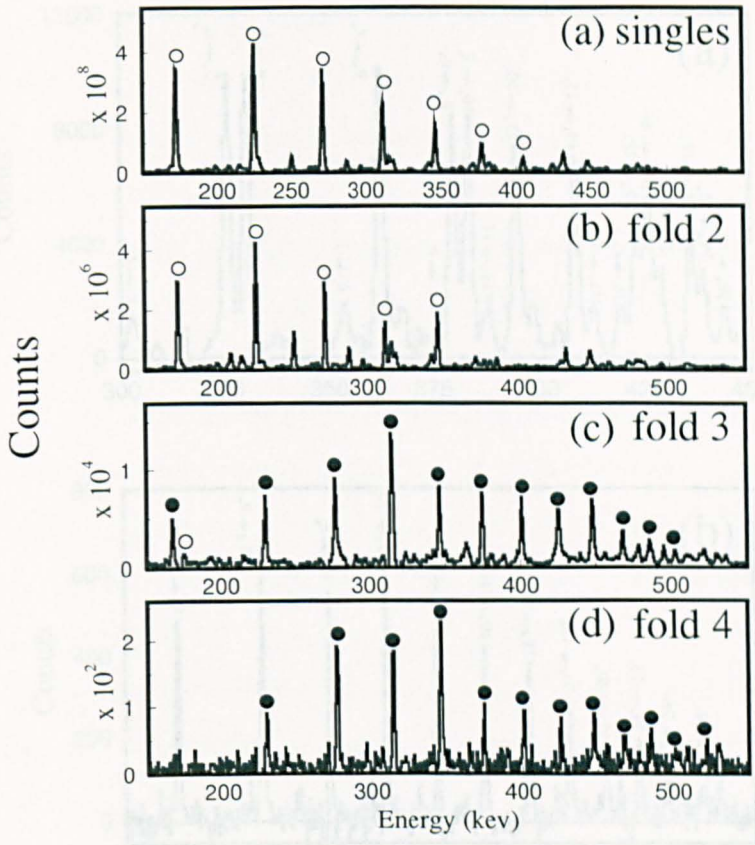

Figure 6.5: (a) Total projection of the ungated cube with a smooth background subtracted; (b) two-fold spectrum generated using the ungated cube; (c) three-fold spectrum generated using the ungated cube; (d) four-fold spectrum generated using the ^{224}Ra-gated cube. Peaks marked with open circles are from Coulomb-excited ^{232}Th and peaks labelled with closed circles are attributed to ^{224}Ra. See text for gating transitions.

coincidences are used. The large amount of triple gamma-ray coincidences acquired in this experiment enables the spectroscopy of high-spin states in this nucleus and many other transfer-reaction products. Figure 6.5(d) shows a four-fold spectrum which was produced by double-gating on the same transitions in the ^{224}Ra-gated cube. There is further improvement in the peak-to-background ratio over the three-fold coincidence spectrum.

The typical spectra shown in figure 6.6 serve to illustrate the quality of these data. Figure 6.6(a) is a three-fold gamma-ray spectrum which shows transitions in ^{218}Rn.

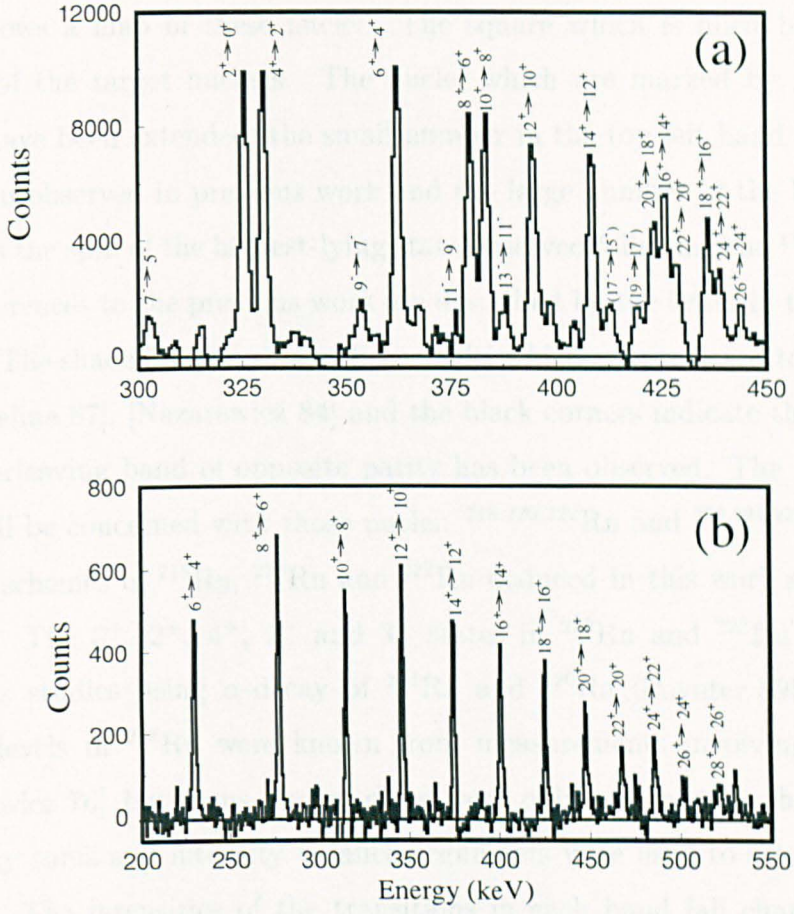

Figure 6.6: (a)Three-fold gamma-ray spectrum showing transitions in ^{218}Rn. (b) Four-fold gamma-ray spectrum showing transitions in ^{224}Ra. Gating transitions are described in the text.

The spectrum was generated by double-gating in the ungated cube on all transitions between the positive-parity states which are shown in the spectrum. Figure 6.6(b) is a four-fold spectrum which shows gamma-ray transitions above and including the 6^+ to 4^+ transition in the ground state rotational band of ^{224}Ra. This was generated by double-gating in the ^{224}Ra-gated cube on all transitions marked in the spectrum. The structural differences between radon and radium isotopes are discussed in section 6.6.3.

High-spin states in many transfer-reaction products have been observed following the ^{136}Xe + ^{232}Th reaction and the level schemes of several nuclei have been extended.

Figure 6.7 shows a map of these nuclei. The square which is filled black denotes the position of the target nucleus. The nuclei which are marked by numbers are those which have been extended; the small number in the top-left hand corner is the maximum spin observed in previous work and the large number in the bottom-right hand corner is the spin of the highest-lying state observed following the $^{136}Xe + ^{232}Th$ reaction. References to the previous work are described by the letter in the top right-hand corner. The shaded region shows those nuclei which are predicted to be octupole deformed [Sheline 87], [Nazarewicz 84] and the black corners indicate those nuclei in which an interleaving band of opposite parity has been observed. The remainder of this thesis will be concerned with those nuclei: $^{218,220,222}Rn$ and $^{222,224,226}Ra$.

The level schemes of ^{218}Rn, ^{220}Rn and ^{222}Rn deduced in this work are presented in figure 6.8. The 0^+, 2^+, 4^+, 1^- and 3^- states in ^{220}Rn and ^{222}Rn were known from previous studies using α-decay of ^{224}Ra and ^{226}Ra [Poynter 89b]. The five lowest-lying levels in ^{218}Rn were known from measurements involving α-decay of ^{222}Ra [Kurcewicz 76] but spins and parities were only assigned to the 0^+ and 2^+ states. Energy sums and intensity balance arguments were used to establish the decay schemes. The intensities of the transitions in each band fall characteristically with increasing spin (see appendix A). The transitions which are in strong coincidence with the known 4^+ to 2^+ and 2^+ to 0^+ transitions have been assigned positive parity. The band of regularly-spaced transitions based on the known $I^\pi = 3^-$ state (tentatively assigned in ^{218}Rn) has been assigned negative parity. This is a reasonable assumption, particularly in the case of ^{220}Rn where the transition to the known 3^- state from the candidate 5^- state has been observed. While this transition is not observed in the adjacent radon isotopes, the spin and parity assignments in figure 6.8 lead to very systematic behaviour with increasing mass for the radon isotopes. The level schemes of ^{222}Ra, ^{224}Ra and ^{226}Ra deduced in this work are shown in figure 6.9. The 0^+, 2^+, 4^+, 1^- and 3^- states in ^{222}Ra were known from previous measurements using α-decay of ^{226}Th [Ruchowska 92]. Information concerning excited states up to $I^\pi = 12^+$ in ^{224}Ra existed from previous studies involving α-decay of ^{228}Th and

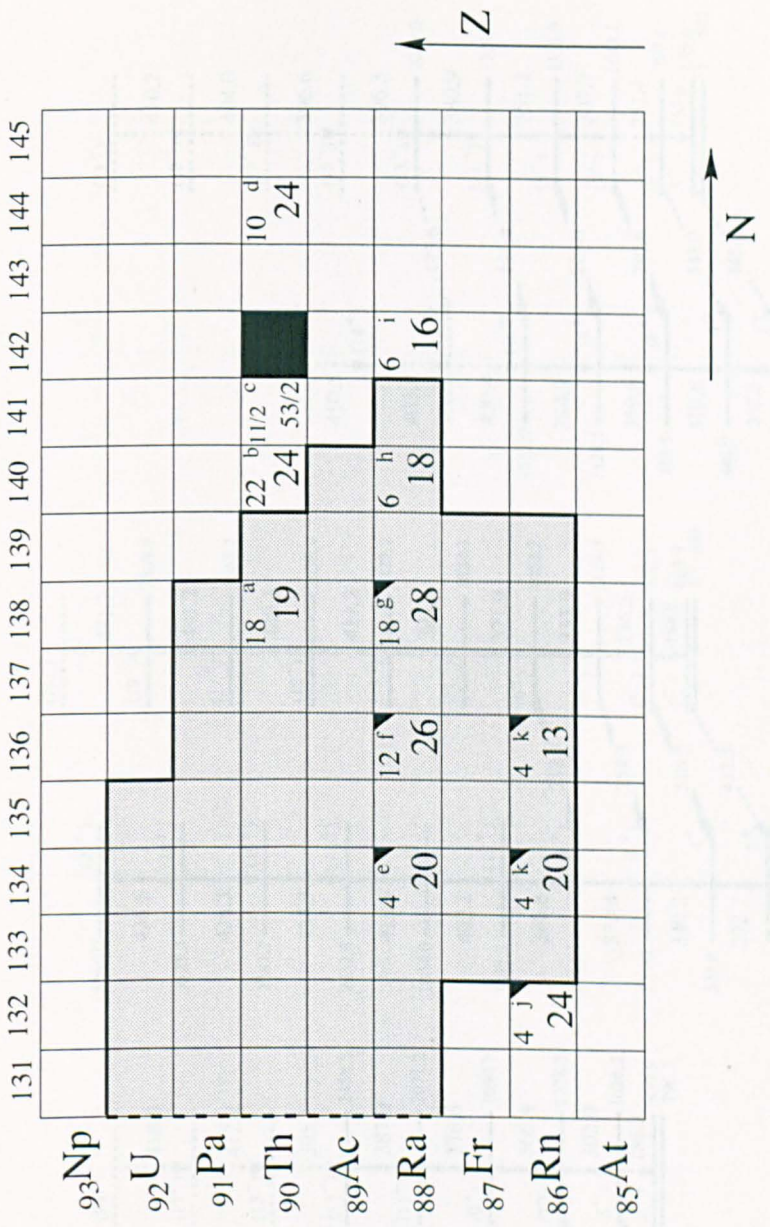

Figure 6.7: Map of nuclei whose level schemes have been extended in this work. The shaded area is the calculated region of octupole deformation [Sheline 87], [Nazarewicz 84]. The small number in the top-left hand corner of nuclei is the maximum spin observed in previous work and the large number in the bottom-right corner is the maximum spin observed following the ^{136}Xe + ^{232}Th reaction. The black corners indicate the observation of interleaving opposite-parity bands. The black square indicates the position of the target nucleus. The letters in the top-right corner of nuclei represent references to the previous work. These are: [a][Ackermann 93]; [b][Kulessa 89]; [c][White 87]; [d][Gerl 89]; [e][Ruchowska 92]; [f][Poynter 89a]; [g][Wollersheim 93]; [h][Ruchowska 82]; [i][Kurcewicz 87]; [j][Kurcewicz 76]; [k][Poynter 89b].

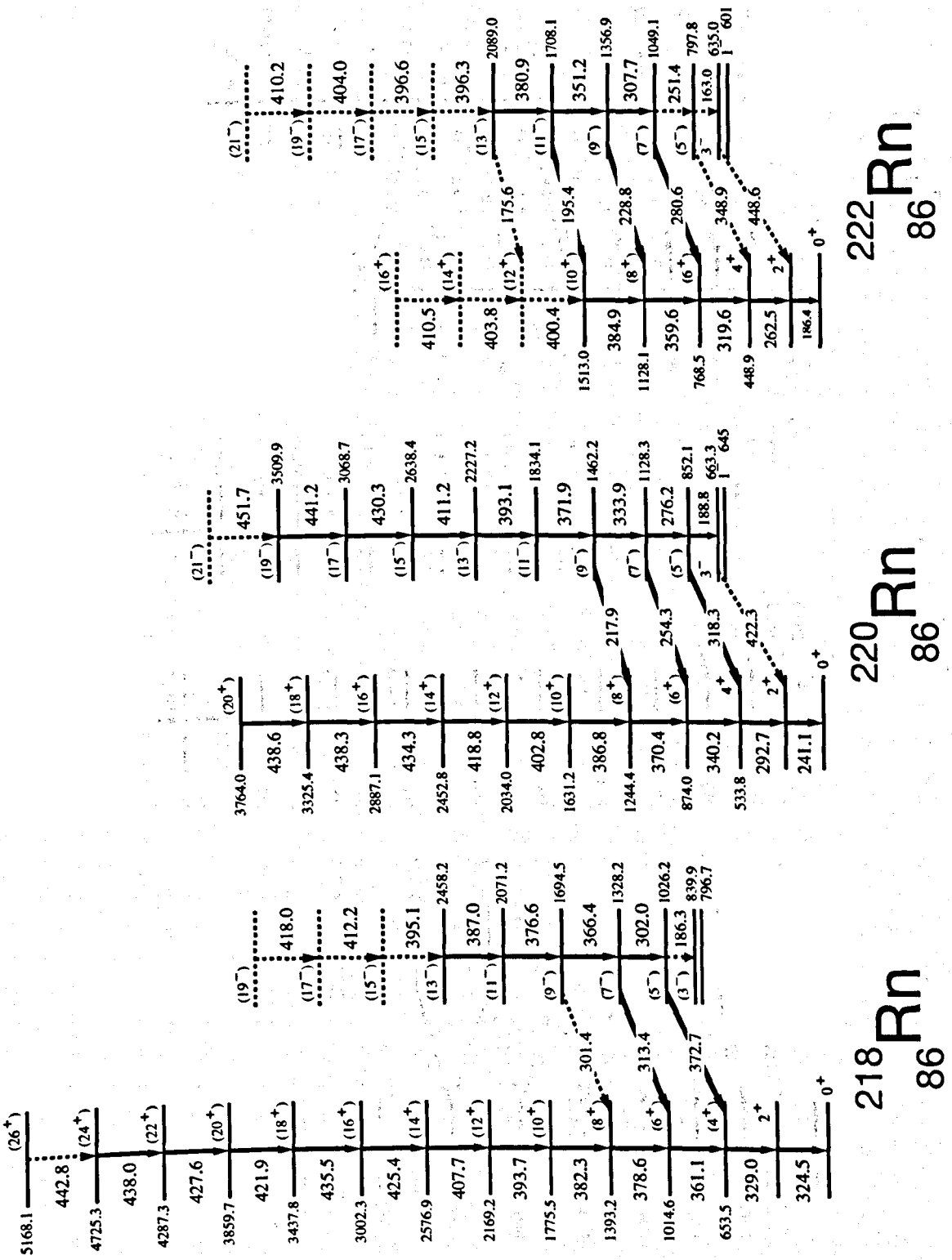

Figure 6.8: Level schemes of ^{218}Rn, ^{220}Rn and ^{222}Rn, produced using energy sums and intensity balance arguments. The transition energies have errors which range from 0.2 keV for low-lying transitions in the positive-parity bands to 0.5 keV for 5^- to 3^- and 7^- to 5^- transitions and transitions between the highest spin states observed.

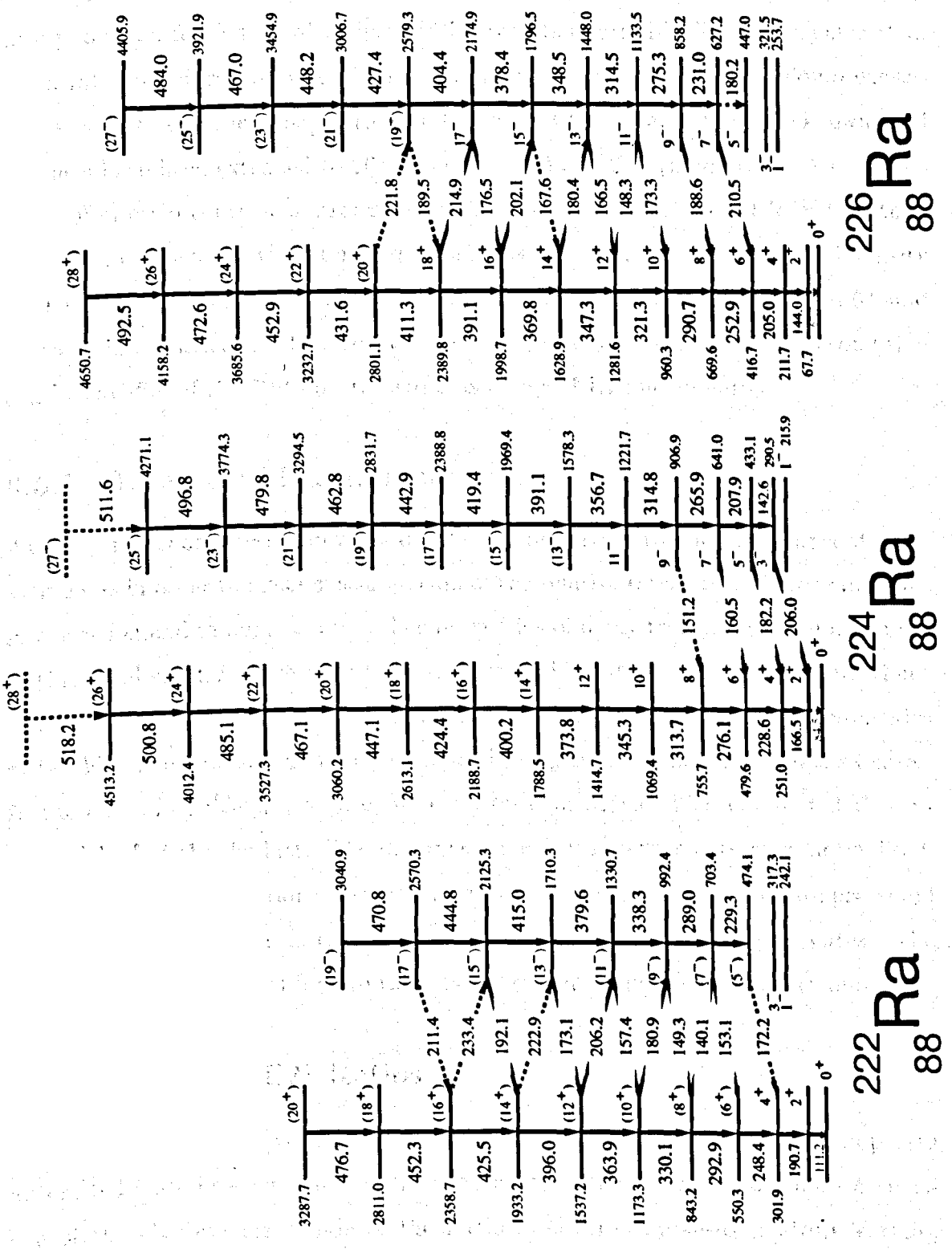

Figure 6.9: Level schemes of ^{222}Ra, ^{224}Ra and ^{226}Ra, produced using energy sums and intensity balance arguments. The transition energies have errors which range from 0.2 keV for low-lying transitions in the positive-parity bands to 0.5 keV for 5^- to 3^- and 7^- to 5^- transitions and transitions between the highest spin states observed.

heavy-ion transfer and $(\alpha, \alpha' 2n)$ using ^{226}Ra targets [Marten-Tölle 90], [Poynter 89a]. Also, information regarding excited states in ^{226}Ra, obtained from Coulomb excitation studies [Wollersheim 93], existed to $I^{\pi} = 18^{+}$. In ^{224}Ra and ^{226}Ra the known level schemes have been extended to 26^{+} (possibly 28^{+}) and 28^{+} respectively. A consideration of internal conversion strongly supports the assignment of electric, rather than magnetic, character to the interband transitions in ^{222}Ra. For example, the intensity of the 6^{+} to 4^{+} transition must be greater or equal to the sum of the 7^{-} to 6^{+} and 8^{+} to 6^{+} intensities after efficiency and internal-conversion correction. This condition can be satisfied if the 7^{-} to 6^{+} transition is assigned E1 multipolarity.

6.5.1 Intensity Measurements

As many nuclei are present in these data it was important to find clean, uncontaminated gates in order to make measurements of the relative intensities of the transitions in the radon and radium isotopes. The intensities of many transitions were measured in three-fold spectra which were generated by double-gating on low-lying transitions, usually the 6^{+} to 4^{+} and 4^{+} to 2^{+} transitions, in the ungated cube. The intensities of the high-spin transitions were determined using higher-lying transitions as gates. In the case of doublets, γ-γ gates were set on transitions which eliminated the unwanted half of the doublet. The different intensity measurements were normalised. The intensities of transitions between the excited states in each nucleus are presented in appendix A. The errors on these values depend upon the choice of gates. The introduction of normalisations to these measurements increased the uncertainties.

6.5.2 B(E1)/B(E2) Ratios

By measuring the relative intensity of the $E1$ and $E2$ transitions which depopulate an excited state in a reflection-asymmetric nucleus, it is possible to obtain a measure of the absolute magnitude of the intrinsic electric dipole-to-quadrupole ratio, $|D_0/Q_0|$. Values of $B(E1)/B(E2)$ can be calculated from $E1$ and $E2$ transition energies and intensities using the rotational model [Butler 91]. The required expression

was presented in chapter 1 as equation 1.26:

$$\frac{B(E1)}{B(E2)} = 7.70 \times 10^{-7} \frac{E_{E2}^5}{E_{E1}^3} \frac{I_{E1}}{I_{E2}}. \tag{6.2}$$

Values for the intrinsic electric dipole-to-quadrupole ratio can be determined using the following expression which is obtained by rearranging equation 1.28:

$$\left|\frac{D_0}{Q_0}\right| = \sqrt{\frac{5}{16} \frac{(2I_i - 2)}{(2I_i - 1)} \frac{B(E1)}{B(E2)}}. \tag{6.3}$$

The I_{E1}/I_{E2} branching ratio for a particular excited state was obtained by double-gating on transitions above the state in the ungated cube. In many cases it was possible to obtain more than one measurement of I_{E1}/I_{E2} by using different transitions as gates. A weighted mean of the individual values was taken in order to obtain the final value. The error on this value was taken to be the standard error on the individual measurements. A value of $|D_0/Q_0|$ was then determined using equations 6.2 and 6.3. In figure 6.9 one can see that interband E1 transitions depopulate states up to $I^\pi = 15^-$ (possibly 17^-) in ^{222}Ra and $I^\pi = 18^+$ (20^+) in ^{226}Ra but although the yrast band in ^{224}Ra has been observed up to $I^\pi = 26^+$ (28^+), no interband E1 transitions have been observed above $I^\pi = 7^-$ (9^-) in this nucleus. Upper limits of $|D_0/Q_0|$ for states between 9^- and 23^- in ^{224}Ra were obtained using the ^{224}Ra-gated cube. These were obtained using two standard deviations in the background count as the intensity of the $E1$ transitions. Figure 6.10 shows values of $|D_0/Q_0|$ measured for excited states in the three isotopes of radium. For ^{222}Ra and ^{226}Ra the values of $|D_0/Q_0|$ are much larger than for ^{224}Ra. However, for all three nuclei the $|D_0/Q_0|$ values remain almost constant over the full spin range. If the electric quadrupole moment does not vary with spin, as observed for ^{226}Ra [Wollersheim 93], then for these radium isotopes the value of D_0 also does not vary. This implies that the small difference in the centre of charge and the centre of mass, which gives rise to the electric dipole moment, is not varying appreciably with spin, and the nuclei have a reflection-asymmetric charge distribution which is rather stable under rotation.

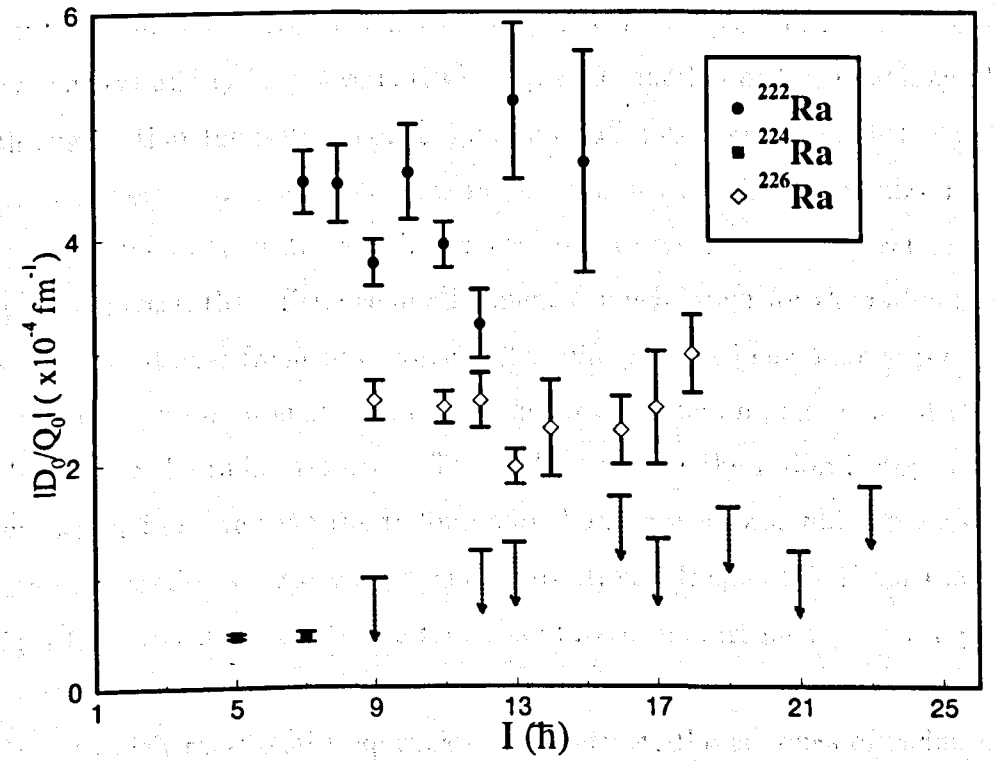

Figure 6.10: Plot of the absolute magnitude of the intrinsic electric dipole-to-quadrupole ratio ($|D_0/Q_0|$) as a function of spin for states in ^{222}Ra, ^{224}Ra and ^{226}Ra. Values of $|D_0/Q_0|$ were derived from $B(E1)/B(E2)$ branching ratios. Upper limits for high-spin states in ^{224}Ra were obtained using two standard deviations in the background count as the intensity of the $E1$ transitions.

6.5.3 Alignment Effects

Figure 6.11 shows the experimental alignment, i_x, as a function of rotational frequency for the positive-parity band in three sets of isotones in the light-actinide region. The plots were produced using experimental data for ^{218}Rn, ^{220}Rn, ^{222}Rn, ^{222}Ra and ^{224}Ra from the present work and ^{220}Ra, ^{222}Th, ^{224}Th and ^{226}Th from previous work [Smith 95], [Ackermann 93]. The rotational frequencies and aligned angular momenta were obtained using equations 1.13 and 1.16. A variable moment of inertia reference with Harris parameters of $J_0 = 31\ \hbar^2\text{MeV}^{-1}$ and $J_1 = 26\ \hbar^4\text{MeV}^{-3}$ has been subtracted (see section 1.5). The Harris parameters were deduced using the

low-spin transitions in ^{222}Ra. The insets in figure 6.11 are plots of the difference in i_x (positive parity) and i_x (negative parity), Δi_x, as a function of $\hbar\omega$. One may observe from the figure that the isotopes of radium and radon exhibit similar behaviour. For these nuclei there is a small difference in the amount of aligned angular momenta for the opposite-parity states which reduces to zero with increasing rotational frequency. In contrast, the difference in alignment is much larger for the radon isotopes, over a wide rotational frequency range. The difference in behaviour is presumably due to the three units of angular momentum provided by an alignment of the octupole phonon for the radon isotopes. This indicates that the radon isotopes are of a more vibrational nature than the radium and thorium isotopes, which possess stable octupole deformation over a wide range of rotational frequency. From the plot of the aligned angular momentum as a function of rotational frequency for the positive-parity states one may observe that the isotopes of thorium and radium exhibit smooth behaviour to high rotational frequencies. In contrast, the isotopes of radon display sudden changes in alignment at $\hbar\omega \approx 0.20$ MeV. ^{218}Rn and ^{220}Rn display additional alignment effects at $\hbar\omega \approx 0.22$ MeV. Cranked shell model calculations were performed for ^{218}Rn, ^{220}Rn and ^{222}Rn in order the discover which orbitals are involved in these alignment effects. These calculations are described in section 6.6.2. Similar alignment effects have previously been observed in octupole-deformed nuclei in the lanthanide region. Interactions between the octupole bands and aligned reflection-symmetric two-quasiparticle bands have been seen in ^{146}Ba [Urban 96], [Zhu 95] and ^{150}Sm [Urban 87]. Figure 6.12 shows the level scheme of ^{150}Sm from [Urban 87]. The octupole band develops at $I \sim 7\hbar$ but disappears at $I \sim 15\hbar$ due an interaction with the aligned reflection-symmetric band.

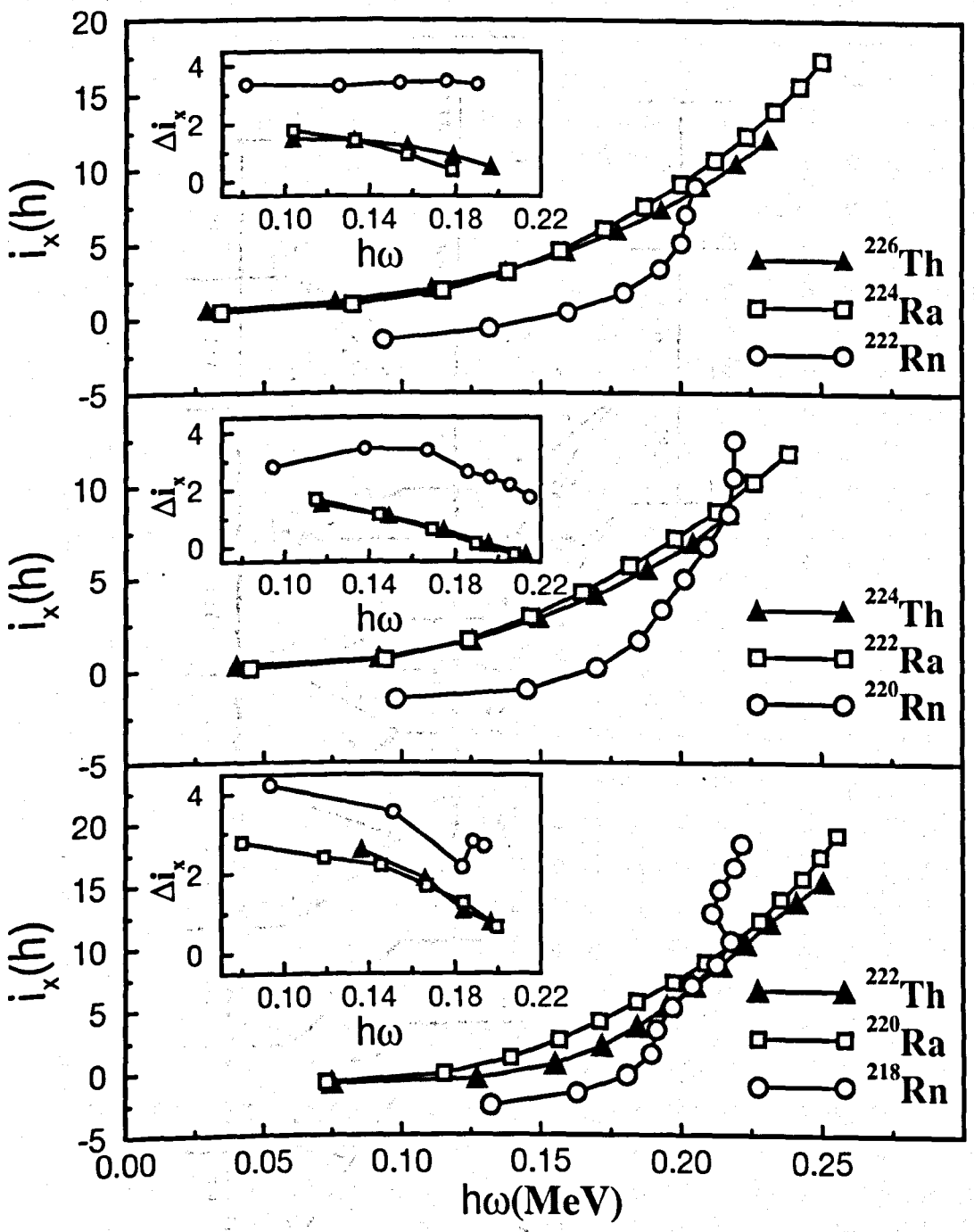

Figure 6.11: Plot of aligned angular momentum i_x as a function of rotational frequency $\hbar\omega$ for states of positive parity in three sets of isotones with N = 132, 134 and 136 for Z = 86, 88 and 90. The insets are plots of the difference in alignment, Δi_x, between the positive- and negative-parity bands as a function of $\hbar\omega$. The value of Δi_x was calculated by subtracting from the value of i_x for each negative-parity state an interpolated, smoothed value for the positive-parity states at the same value of $\hbar\omega$.

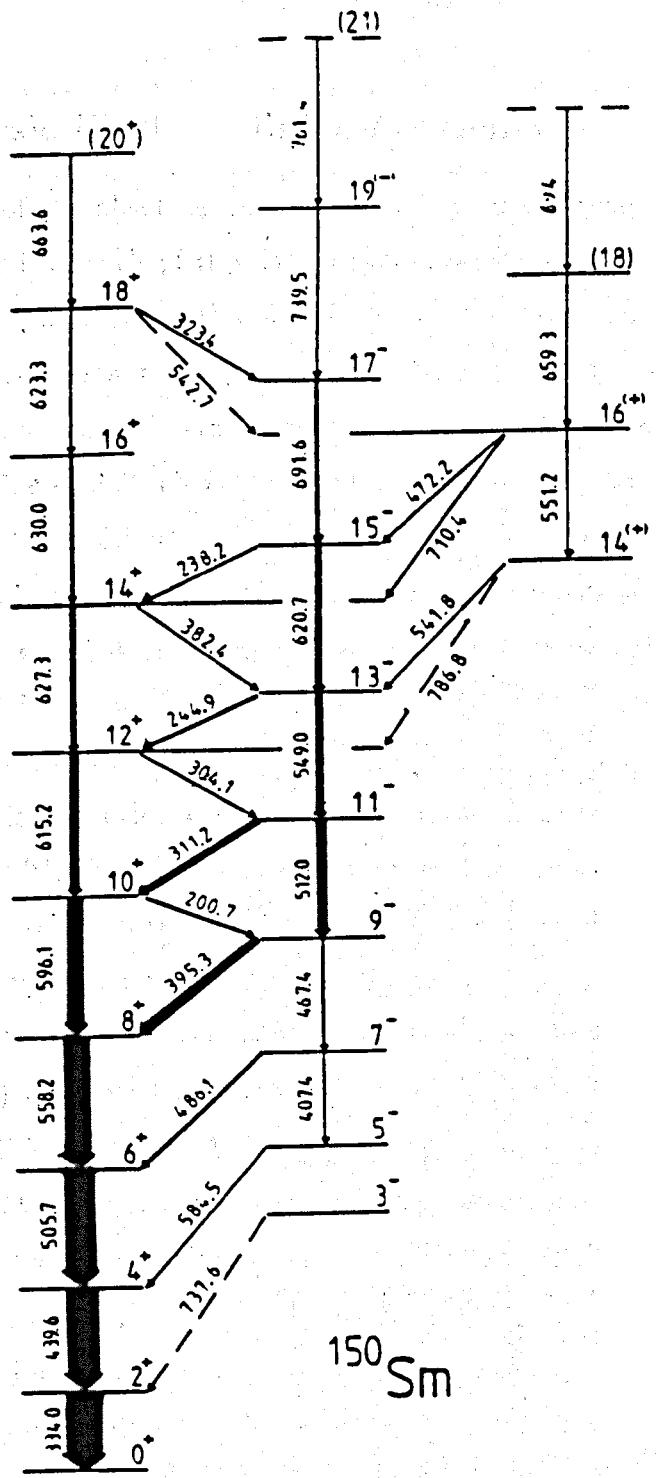

Figure 6.12: The level scheme of ^{150}Sm showing an interaction between the octupole band and a reflection-symmetric band. Taken from [Urban 87]

6.6 Discussion

6.6.1 Intrinsic Electric Dipole Moments

A measurement of the absolute magnitude of the intrinsic electric dipole moment, $|D_0|$, was obtained for each of the six octupole nuclei using weighted-mean $|D_0/Q_0|$ values and published values of the intrinsic quadrupole moment Q_0 [Raman 87], assuming that Q_0 is constant with spin. As an intrinsic electric quadrupole moment has not been measured for ^{218}Rn, Grodzins' principle [Grodzins 62] was used to determine a Q_0 value of 3.59 eb for this nucleus. Also, the (almost constant) values of Q_0 for different transitions in ^{226}Ra were taken from [Wollersheim 93]. Table 6.2 compares $|D_0|$ values measured in this work with those measured in previous work and values which were deduced using macroscopic-microscopic calculations [Butler 91] and, where available, self-consistent theory [Robledo 87], [Egido 91]. Also shown is the $|D_0|$ value previously measured for ^{220}Ra [Smith 95a]. At low spin, Butler and Nazarewicz [Butler 91] calculated a very small value of the intrinsic electric dipole moment, D_0, for ^{224}Ra by treating it as the sum of a macroscopic (droplet) component and a microscopic (shell correction) term. The shell correction contribution is negative and increases in magnitude with increasing mass, almost cancelling out the positive droplet contribution in the case of ^{224}Ra. Self-consistent calculations also reproduce the small $B(E1)$ value for this nucleus [Egido 91]. These calculations used the constrained HF+BCS model with Gogny density-dependent interaction. The measured upper limit of $|D_0|$ for ^{224}Ra indicates that the small value persists to high spin in this nucleus. Values of $|D_0|$ extracted for the radon isotopes appear to be in good agreement with the macroscopic-microscopic values where the small D_0 value arises from the small value of β_2 for these nuclei. In contrast, the self-consistent calculation gives a large negative value for D_0 in ^{222}Rn. The average values of $|D_0|$ measured in the present work for ^{224}Ra and ^{226}Ra are consistent with previous measurements at lower spin [Poynter 89a], [Marten-Tölle 90], [Ackermann 93]. The theoretically-predicted reduction in $|D_0|$ as one moves from ^{220}Ra to ^{224}Ra is observed experi-

Nucleus	Experiment				Theory			
	This Work		Previous Work		Macro-micro[f]		Self-consistent	
	I range	$\|D_0\|$ (e.fm)	I range	$\|D_0\|$ (e.fm)	I range	D_0 (e.fm)	I range	D_0 (e.fm)
^{218}Rn	7	0.035(3)	-	-	0	0.04	-	-
^{220}Rn	5-9	0.04(1)	-	-	0	−0.04	-	-
^{222}Rn	9-11	0.10(2)	-	-	0	−0.10	0	−0.36[g]
^{220}Ra	-	-	6-26	0.34(4)[a]	0	0.17	0	0.23[h*]
					4	0.18		
^{222}Ra	7-15	0.27(4)	3	0.38(6)[b]	0	0.09	0	0.13[h*]
					5-7	0.11		
^{224}Ra	5-7	0.030(1)	3-5	0.028(4)[c]	0	0.01	0	0.05*
	12-23	<0.09	7-9	<0.11[c]	6	0.01		
			1-5	0.06-0.10[d]	0	−0.09	0	0.10[h*]
^{226}Ra	9-18	0.19(3)	7-12	0.12-0.21[d]	7-12	−0.09		
			7-11	0.16(1)[e]				

Table 6.2: A comparison of the experimental intrinsic electric dipole moments measured in this work with those measured in previous work. Also shown are the values which were calculated using macroscopic-microscopic theory and self-consistent theory. The superscripts represent the following references: [a][Smith 95a]; [b][Ruchowska 92]; [c][Poynter 89a]; [d][Wollersheim 93]; [e][Ackermann 93]; [f][Butler 91]; [g][Robledo 87]; [h][Egido 91]. Experimental $|D_0|$ values are derived from weighted mean values of $|D_0/Q_0|$ and Q_0 values from reference [Raman 87], except for ^{218}Rn where Q_0 was determined using Grodzins' principle and ^{226}Ra where values were taken from reference [Wollersheim 93]. The errors associated with experimental values measured in the present work are one standard deviation in values measured for different excited states. The superscript * means that sign of the value is not given.

mentally. However, the values measured in this work for ^{222}Ra and ^{226}Ra and the previously-measured value for ^{220}Ra [Smith 95a] are a factor of two or more greater in magnitude than both sets of theoretical values.

6.6.2 Comparison With Cranked Shell Model Calculations

Cranked shell model (CSM) calculations were performed with the Woods-Saxon deformed shell model potential [Dudek 79] with "universal" parameterisation [Dudek 81] and deformation parameters of ^{218}Rn and ^{220}Rn taken from reference [Butler 91]. Using $(\beta_2, \beta_3, \beta_4) = (0.085, 0.092, 0.060)$ for ^{218}Rn, $(0.102, 0.096, 0.068)$ for ^{220}Rn and $(\beta_2, \beta_3, \beta_4) = (0.116, 0.094, 0.071)$ for ^{222}Rn, the calculations predict a strong interaction between the ground band and an aligned $j_{15/2}$ neutron band at a rotational frequency of $\hbar\omega \approx 0.25$ MeV and a weak interaction with an aligned $i_{13/2}$ proton band at $\hbar\omega \approx 0.25$ MeV for each nucleus. The results of the calculations for ^{220}Rn are shown in figures 6.13(a) (neutron Routhians) and 6.13(b) (proton Routhians). The dashed lines represent orbitals with positive simplex and negative-simplex orbitals are shown as dot-dash lines. The $i_{13/2}$ proton orbitals slope down steeply, indicating a large amount of alignment, and come close together at $\hbar\omega \approx 0.25$ MeV. This represents a weak interaction with an aligned $i_{13/2}$ proton band. The $j_{15/2}$ neutron orbitals remain far apart and interact at $\hbar\omega \approx 0.22$ MeV. This strong interaction is presumably responsible for the upbend in the experimental alignment plots at $\hbar\omega \approx 0.20$ MeV, while the weak interaction between the proton orbitals causes the additional alignment effects at $\hbar\omega \approx 0.22$ MeV.

6.6.3 Contrasting Behaviour

The opposite-parity bands of radium and thorium possess a similar amount of aligned angular momentum at low frequencies. The difference in the amount of aligned angular momentum for the states of opposite parity tends towards zero with increasing frequency. In contrast, the difference in alignment is much larger for the radon isotopes because the negative-parity states have a greater amount of alignment. The

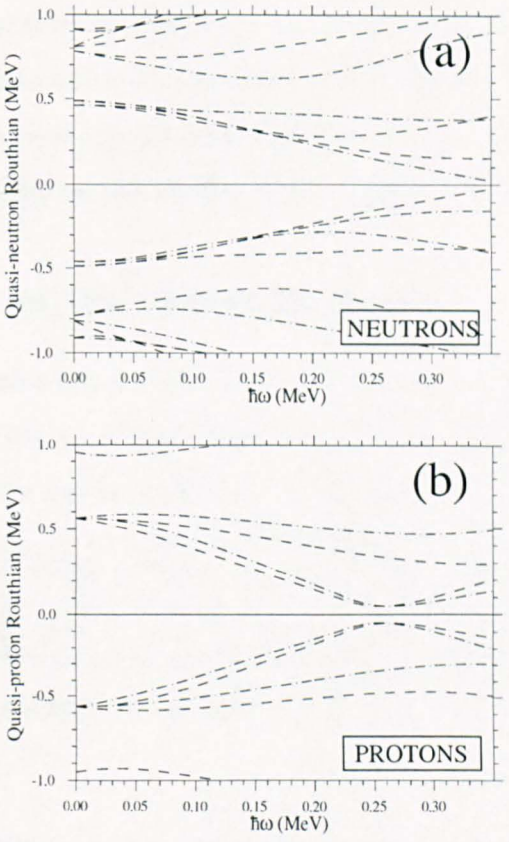

Figure 6.13: The results of cranked shell model calculations with the deformed Woods-Saxon potential with parameterisation taken from [Dudek 81]. Quasi-neutron Routhians are shown in part (a) and quasi-proton Routhians are presented in part (b). See text for deformation parameters.

additional alignment is presumably due to the octupole phonon. This indicates that the radon isotopes are vibrational over a wide range of frequencies, while the radium and thorium isotopes possess more stable octupole shapes. Strong alignment effects were observed for the radon isotopes in this work. Such rapid changes in alignment were not observed in the radium isotopes where regular structures are maintained to the highest spins observed. Similarly, the yrast sequences in thorium isotopes exhibit smooth behaviour over a wide range of N [Butler 96]. The sudden increases in alignment are not seen in the radium and thorium isotopes because of the effect of the stronger octupole interaction between high- and low-spin orbitals in these nuclei

[Nazarewicz 85]. This argument would be consistent with the observation of small $|D_0|$ values for the radon isotopes (see table 6.2) and both self-consistent calculations [Robledo 87] and macroscopic-microscopic calculations [Nazarewicz 84] which predict a shallower octupole energy minimum for ^{222}Rn than for ^{222}Ra and ^{224}Ra.

6.6.4 Properties of the Octupole Bands

A purely-vibrational even-even nucleus has its 4^+ state at approximately twice the energy of its 2^+ state. That is, $E(4^+)/E(2^+) \approx 2$. For a rotational nucleus this value is 3.33. The values for the nuclei studied in this work are given in table 6.3.

Nucleus	^{218}Rn	^{220}Rn	^{222}Rn	^{222}Ra	^{224}Ra	^{226}Ra
$\frac{E(4^+)}{E(2^+)}$	2.0	2.2	2.4	2.7	3.0	3.1

Table 6.3: Ratios of the energies of the lowest-lying 2^+ and 4^+ states for the six nuclei studied in this work.

The values indicate that the radon isotopes are more vibrational than the radium isotopes at low spin, and that the isotopes become more rotational with increasing mass number.

Nazarewicz and Olanders [Nazarewicz 85] defined two quantities which describe the high-spin behaviour of octupole nuclei: the frequency ratio and parity splitting. The quantities, which are defined in section 2.2.2, are plotted in figures 6.14 and 6.15 for ^{218,220,222}Rn and ^{222,224,226}Ra. Also shown are the limits for nuclei with stable octupole deformation: zero parity splitting and a frequency ratio of unity. In figure 6.14 the bands of ^{222}Ra and ^{224}Ra cross the octupole-deformed limit at $\sim 9\hbar$, while ^{226}Ra, ^{220}Ra and ^{222}Rn cross the boundary at $\sim 12\hbar$. ^{218}Rn lies above the boundary for all spin states. This may indicate that ^{218}Rn has a more vibrational nature, even at high spins. The parity splitting for the radon isotopes is much larger than for the radium isotopes in the 0 - $5\hbar$ region. This is because the radon isotopes are of a more vibrational nature at low spin. In figure 6.15 the radon isotopes are close to

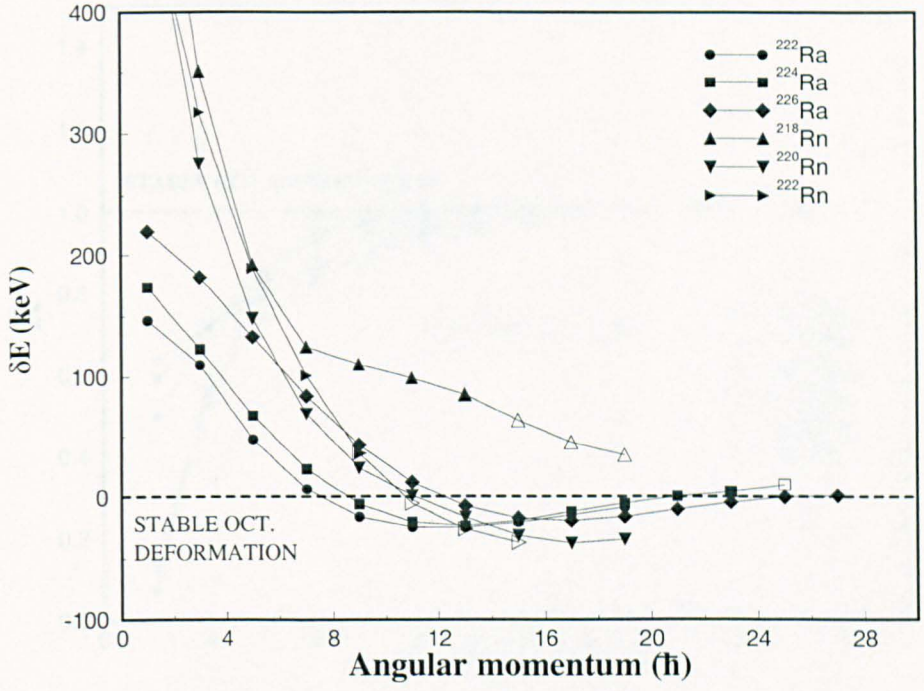

Figure 6.14: The energy displacement between the positive- and negative-parity states, δE, as a function of spin in the octupole bands of the nuclei studied in this work. The quantity δE tends to zero for an octupole-rotor. The open symbols represent values deduced using transitions between tentatively-assigned levels.

the octupole-vibrational limit at low spins but approach the limit of stable octupole deformation at $\sim 14\hbar$. The radium isotopes reach the limit at $\sim 11\hbar$.

6.7 Summary

It has been shown that multinucleon transfer reactions with thick targets and high-efficiency germanium-detector arrays are a viable means of populating high-spin states in light-actinide nuclei which are hard to access by other mechanisms. Interleaving bands of alternating-parity states have been observed to high spin in ^{224}Ra, ^{226}Ra and, for the first time, in ^{222}Ra, ^{218}Rn, ^{220}Rn and ^{222}Rn. In ^{222}Ra and ^{226}Ra the extracted value of $|D_0/Q_0|$ is approximately independent of spin, while in ^{224}Ra the value indicates that the cancellation of contributions to the intrinsic electric dipole

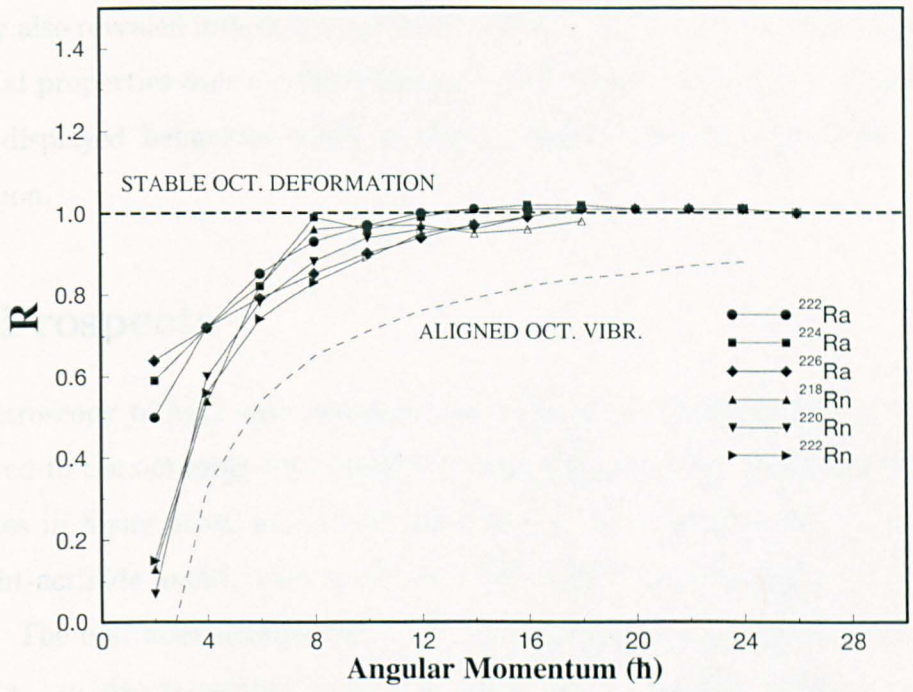

Figure 6.15: The rotational frequency ratio, R, as a function of spin for the octupole bands of the nuclei studied in this work. The ratio should be equal to unity for an octupole-rotor, that is the rotational frequencies of the opposite parity bands should be the same. The open symbols represent values deduced using transitions between tentatively-assigned levels.

moment persists to high spins. The observation of the behaviour of D_0 implies that the reflection-asymmetric charge distribution is hardly affected by rotations in the radium isotopes where detailed measurements are available. Intrinsic electric dipole moments measured for the radon isotopes were much smaller than those for ^{222}Ra and ^{226}Ra. Also, plots of experimental alignment as a function of rotational frequency revealed sudden onsets in alignment effects in the positive parity bands in the three radon isotopes. The results of CSM calculations suggested that these effects are due to alignments of $i_{13/2}$ protons and $j_{15/2}$ neutrons. No such effects are observed in the radium isotopes, nor indeed in any previously-studied isotopes of radium and thorium. The difference in behaviour may be due to weaker octupole mixing of high-spin orbitals with lower-spin orbitals for the radon isotopes. Plots of the difference in alignment for the positive- and negative-parity states as a function of rotational

frequency also revealed interesting structure differences. The radon isotopes exhibited vibrational properties over a wide frequency range, while the isotopes of radium and thorium displayed behaviour which is characteristic of nuclei with stable octupole deformation.

6.8 Prospects

The spectroscopy of high-spin states in light-actinide nuclei described in this thesis was limited to the octupole-deformed even-even isotopes of radon and radium. High-spin states in many other nuclei are populated in the reaction and the analysis of other light-actinide nuclei, such as ^{234}Th, ^{228}Ra and ^{230}Ra (see figure 6.7), is still in progress. The odd-mass neighbours of the radium and radon isotopes, such as ^{223}Ra and ^{225}Ra, are also populated in this reaction. Parity-doublet bands are predicted in many of these odd-A nuclei. Analysis of these nuclei is also ongoing. The yield analysis of chapter 5 will be repeated using the high-fold statistics collected with the GAMMASPHERE array. More accurate measurements of the yield of the populated nuclei will be possible using three-dimensional analysis techniques. Spectroscopic studies concerning the projectile-like transfer products are also in progress.

APPENDIX A

^{222}Ra intensities

$J_i^{\pi_i}$	$J_f^{\pi_f}$	Mult.	Energy (keV)	Intensity	Intensity (int-conv corrected)
2^+	0^+	E2	111.2	28(12)	205(91)
4^+	2^+	E2	190.7	100(19)	171(32)
6^+	4^+	E2	248.4	86(17)	110(21)
7^-	6^+	E1	153.1	72(23)	84(27)
7^-	5^-	E2	229.3	13(4)	18(5)
8^+	6^+	E2	292.9	61(5)	72(6)
8^+	7^-	E1	140.1	66(12)	80(14)
9^-	8^+	E1	149.3	50(8)	58(10)
9^-	7^-	E2	289.0	44(5)	52(6)
10^+	8^+	E2	330.1	43(4)	49(5)
10^+	9^-	E1	180.9	57(13)	64(15)
11^-	10^+	E1	157.4	27(4)	31(4)
11^-	9^-	E2	338.3	42(4)	46(6)
12^+	10^+	E2	363.9	42(4)	46(4)
12^+	11^-	E1	206.2	27(5)	30(6)
13^-	12^+	E1	173.1	28(4)	32(5)
13^-	11^-	E2	379.6	34(3)	36(4)
14^+	12^+	E2	396.0	30(4)	32(4)
15^-	14^+	E1	192.1	23(10)	25(11)
15^-	13^-	E2	415.0	34(4)	35(4)
16^+	14^+	E2	425.5	24(4)	25(4)
17^-	15^+	E2	444.8	32(6)	34(6)
18^+	16^+	E2	452.3	17(4)	17(4)
19^-	17^-	E2	470.8	15(4)	16(4)
20^+	18^+	E2	476.7	10(4)	11(4)

^{224}Ra intensities

$J_i^{\pi_i}$	$J_f^{\pi_f}$	Mult.	Energy (keV)	Intensity	Intensity (int-conv corrected)
3^-	2^+	E1	206.0	54(12)	59(13)
4^+	2^+	E2	166.5	100(5)	218(11)
5^-	4^+	E1	182.2	28(8)	31(9)
5^-	3^-	E2	142.6	39(11)	124(35)
6^+	4^+	E2	228.6	146(28)	200(38)
7^-	6^+	E1	160.5	15(4)	17(5)
7^-	5^-	E2	207.9	113(21)	171(32)
8^+	6^+	E2	276.1	156(19)	188(23)
9^-	7^-	E2	265.9	94(26)	115(32)
10^+	8^+	E2	313.7	151(15)	171(17)
11^-	9^-	E2	314.8	98(22)	111(25)
12^+	10^+	E2	345.3	121(4)	133(4)
13^-	11^-	E2	356.7	83(15)	91(16)
14^+	12^+	E2	373.8	87(4)	94(4)
15^-	13^-	E2	391.1	55(14)	59(15)
16^+	14^+	E2	400.2	77(8)	82(9)
17^-	15^+	E2	419.4	37(9)	39(10)
18^+	16^+	E2	424.4	57(8)	60(8)
19^-	17^-	E2	442.9	29(9)	31(9)
20^+	18^+	E2	447.1	31(6)	33(6)
21^-	19^-	E2	462.8	24(7)	25(7)
22^+	20^+	E2	467.1	23(5)	24(5)
23^-	21^-	E2	479.8	21(7)	22(7)
24^+	22^+	E2	485.1	17(5)	18(5)
25^-	23^-	E2	496.8	7(3)	7(3)
26^+	24^+	E2	500.8	4(2)	4(2)

^{226}Ra intensities

$J_i^{\pi_i}$	$J_f^{\pi_f}$	Mult.	Energy (keV)	Intensity	Intensity (int-conv corrected)
4^+	2^+	E2	144.0	100(6)	310(19)
6^+	4^+	E2	205.0	164(21)	253(33)
7^-	6^+	E1	210.5	44(6)	48(6)
8^+	6^+	E2	252.9	160(21)	202(27)
9^-	8^+	E1	188.6	90(5)	99(6)
9^-	7^-	E2	231.0	30(7)	41(10)
10^+	8^+	E2	290.7	141(10)	165(12)
11^-	10^+	E1	173.3	72(4)	82(5)
11^-	9^-	E2	275.3	75(14)	90(17)
12^+	11^-	E1	148.3	29(5)	34(6)
12^+	10^+	E2	321.3	98(3)	110(3)
13^-	12^+	E1	166.5	22(4)	25(5)
13^-	11^-	E2	314.5	83(16)	94(18)
14^+	13^-	E1	180.4	23(5)	26(6)
14^+	12^+	E2	347.3	78(18)	86(20)
15^-	13^-	E2	348.5	69(14)	76(15)

continued on next page

$J_i^{\pi_i}$	$J_f^{\pi_f}$	Mult.	Energy (keV)	Intensity	Intensity (int-conv corrected)
16^+	15^-	E1	202.1	16(2)	17(2)
16^+	14^+	E2	369.8	55(3)	60(3)
17^-	16^+	E1	176.5	13(3)	15(3)
17^-	15^-	E2	378.4	62(13)	67(14)
18^+	17^-	E1	214.9	18(2)	19(2)
18^+	16^+	E2	391.1	42(3)	45(3)
19^-	17^-	E2	404.4	53(14)	57(15)
20^+	18^+	E2	411.3	21(3)	22(3)
21^-	19^-	E2	427.4	17(5)	18(5)
22^+	20^+	E2	431.6	11(2)	12(2)
23^-	21^-	E2	448.2	11(4)	12(4)
24^+	22^+	E2	452.9	12(3)	13(3)
25^-	23^-	E2	467.0	8(3)	8(3)
26^+	24^+	E2	472.6	3(2)	3(2)
27^-	25^-	E2	484.0	4(3)	4(3)
28^+	26^+	E2	492.5	2(1)	2(1)

^{218}Rn intensities

$J_i^{\pi_i}$	$J_f^{\pi_f}$	Mult.	Energy (keV)	Intensity	Intensity (int-conv corrected)
2^+	0^+	E2	324.5	100(19)	111(21)
4^+	2^+	E2	329.0	96(18)	106(20)
5^-	4^+	E1	372.7	34(5)	35(5)
6^+	4^+	E2	361.1	83(5)	90(5)
7^-	6^+	E1	313.4	17(4)	18(4)
7^-	5^-	E2	302.0	33(5)	38(6)
8^+	6^+	E2	378.6	68(13)	73(14)
9^-	7^-	E2	366.4	34(5)	37(5)
10^+	8^+	E2	382.3	49(7)	52(7)
11^-	9^-	E2	376.6	38(13)	41(14)
12^+	10^+	E2	393.7	39(7)	42(7)
13^-	11^-	E2	387.0	24(8)	26(9)
14^+	12^+	E2	407.7	30(3)	32(3)
16^+	14^+	E2	425.4	21(3)	22(3)
18^+	16^+	E2	435.5	13(3)	14(3)
20^+	18^+	E2	421.9	10(3)	11(3)
22^+	20^+	E2	427.6	7(3)	7(3)
24^+	22^+	E2	438.0	5(3)	5(3)

^{220}Rn intensities

$J_i^{\pi_i}$	$J_f^{\pi_f}$	Mult.	Energy (keV)	Intensity	Intensity (int-conv corrected)
2^+	0^+	E2	241.1	100(20)	128(26)
4^+	2^+	E2	292.7	94(9)	108(10)
5^-	4^+	E1	318.3	53(8)	55(8)
5^-	3^-	E2	188.8	13(4)	22(7)
6^+	4^+	E2	340.2	84(8)	92(9)
7^-	6^+	E1	254.3	17(4)	18(4)
7^-	5^-	E2	276.2	41(8)	48(9)
8^+	6^+	E2	370.4	78(19)	84(20)
9^-	8^+	E1	217.9	10(3)	11(3)
9^-	7^-	E2	333.9	72(11)	79(12)
10^+	8^+	E2	386.8	71(12)	76(13)
11^-	9^-	E2	371.9	70(12)	75(13)
12^+	10^+	E2	402.8	52(12)	55(13)
13^-	11^-	E2	393.1	66(8)	70(9)
14^+	12^+	E2	418.8	44(11)	46(12)
15^-	13^-	E2	411.2	51(10)	54(11)
16^+	14^+	E2	434.3	36(12)	38(13)
17^-	15^-	E2	430.3	26(10)	27(11)
18^+	16^+	E2	438.3	-	-
19^-	17^-	E2	441.2	20(13)	21(14)
20^+	18^+	E2	438.6	-	-

^{222}Rn intensities

$J_i^{\pi_i}$	$J_f^{\pi_f}$	Mult.	Energy (keV)	Intensity	Intensity (int-conv corrected)
2^+	0^+	E2	186.4	100(15)	169(25)
4^+	2^+	E2	262.5	134(20)	162(10)
6^+	4^+	E2	319.6	118(26)	132(29)
7^-	6^+	E1	280.6	25(7)	26(7)
8^+	6^+	E2	359.6	75(14)	81(15)
9^-	8^+	E1	228.8	23(13)	24(14)
9^-	7^-	E2	307.7	31(13)	35(15)
10^+	8^+	E2	384.9	40(11)	43(11)
11^-	10^+	E1	195.4	22(14)	24(15)
11^-	9^-	E2	351.2	46(14)	50(15)
13^-	11^-	E2	380.9	15(8)	16(9)

References

[Ackermann 93] B. Ackermann *et al.*, Nucl. Phys. **A559** 61 (1993)

[Ahmad 88] S. A. Ahmad, W. Klempt, R. Neugart, E. W. Otten, P.-G. Reinhard, G. Ulm and K. Wendt, Nucl. Phys. **A483** 244 (1988)

[Ahmad 93] I. Ahmad and P. A. Butler, Annu. Rev. Nucl. Part. Sci. **43** 71 (1993)

[Aïche 94] M. Aïche *et al.*, Nucl. Phys. **A567** 685 (1994)

[Aïche 88] M. Aïche, A. Chevallier, J. Chevallier, S. Hulne, S. Khazrouni, N. Schulz and J. C. Sens, J. Phys. G: Nucl. Part. Phys. **14** 1191 (1988)

[Artukh 73] A. G. Artukh, G. F. Gridnev, V. L. Mikheev, V. V. Volkov and J. Wilczynski, Nucl. Phys. **A215** 91 (1973)

[Asaro 53] F. Asaro, F. Stephens Jr. and I. Perlman, Phys. Rev. **92** 1495 (1953)

[Aufmuth 87] P. Aufmuth, K. Heilig and A. Steudel, At. Data. Nucl. Data Tables **37** 455 (1987)

[Bardeen 57] J. Bardeen, L. N. Couper and J. R. Schreifer, Phys. Rev. **108** 1175 (1957)

[Baxter 92] A. M. Baxter, T. L. Khoo, M. E. Bleich, M. P. Carpenter, I. Ahmad, R. V. F. Janssens, E. F. Moore, I. G. Bearden, J. R. Beene and I. Y. Lee, Nucl. Instrum. Methods Phys. Res., Sect. A **317**, 101 (1992)

[Beausang 92] C. W. Beausang *et al.*, Nucl. Instr. Meth. In Phys. Res. A **313** 37 (1992)

[Beck 92] F. A. Beck *et al.*, Prog. Part. Nucl. Phys. **28** 443 (1992)

[Bengtsson 85] R. Bengtsson and G. D. Garrett, Int. Rev. Nucl. Phys. **1** World Scientific (1985)

[Blatt 52] J. M. Blatt and V. F. Weisskopf, *Theoretical Nuclear Physics*, John Wiley and Sons Inc., New York (1952)

[Bohr 52] A. Bohr, K. Dan. Vidensk. Selsk. Mat.-Fys. Medd. Mat. **26** No. 14 (1952)

[Bohr 57] A. Bohr and B. R. Mottelson, Nucl. Phys. **4** 529 (1957)

[Bohr 58] A. Bohr and B. R. Mottelson, Nucl. Phys. **9** 687 (1958)

[Bohr 75] A. Bohr and B. R. Mottelson, *Nuclear Structure Volume II: Nuclear Deformations*, W. A. Benjamin Inc., New York (1975)

[Bonin 83] W. Bonin, M. Dahlinger, S. Glienke, E. Kankeleit, M. Krämer, D. Habs, B. Schwartz and H. Backe, Z. Phys. A **310** 249 (1983)

[Bonin 85] W. Bonin, H. Backe, M. Dahlinger, S. Glienke, D. Habs, E. Henelt, E. Kankeleit amd B. Schwartz, Z. Phys. A **322** 59 (1985)

[Borchers 87] W. Borchers, R. Neugart, E. W. Otten, H. T. Duong, G. Ulm and K. Wendt, Hyperfine Interactions **34** 25 (1987)

[Brack 72] M. Brack, J. Damgård, A. S. Jensen, H. C. Pauli, V. M. Strutinsky and C. Y. Wong, Rev. Mod. Phys. 44 320 (1972)

[Broda 90] R. Broda, M. A. Quader, P. J. Daly, R. V. F. Janssens, T. L. Khoo, W. C. Ma, M. W. Drigert, Phys. Lett. **B251** 245 (1990)

[Broda 94] R. Broda, C. T. Zhang, P. Kleinheinz, R. Menegazzo, K. H. Maier, H. Grawe, M. Schramm, R. Schubart, M. Lach, S. Hofmann, Phys. Rev. C **49**, R575 (1994).

[Broda 95] R. Broda *et al.*, Phys. Rev. Lett. **74**, 868 (1995)

[Broda 96] R. Broda, private communication

[Butler 91] P. A. Butler and W. Nazarewicz, Nucl. Phys. **A533** 249 (1991)

[Butler 96] P. A. Butler and W. Nazarewicz, Rev. Mod. Phys **68** 349 (1996)

[Carpenter 94] M. P. Carpenter *et al.*, Nucl. Instrum. Methods Phys. Res., Sect. A **353**, 234 (1994)

[Casten 90] R. F. Casten, *Nuclear Structure from a Simple Perspective*, Oxford University Press, Oxford (1990)

[Cocks 96] J. F. C. Cocks *et al.* to be submitted to Phys. Rev. Lett.

[Cresswell 91] J. R. Cresswell, "Event Format [Sorting + Storage]", http://nnsa.dl.ac.uk/Eurogam/documents/edoc073 (1991)

[Cresswell 95] A. J. Cresswell *et al.*, Phys. Rev. C **52**, 1934 (1995)

[Cristancho 94] F. Cristancho *et al.*, Phys. Rev. C **49** 663 (1994)

[Ćwiok 87] S. Ćwiok, J. Dudek, W. Nazarewicz, J. Skalski and T. Werner, Com. Phys. Comm. **46** 379 (1987)

[Dahlinger 88] M. Dahlinger, E. Kankeleit, D. Habs, D. Schwalm, R. S. Simon, J. D. Burrows and P. A. Butler, Nucl. Phys. **A484** 337 (1988)

[Davydov 65] A. S. Davydov, *Quantum Mechanics*, Pergamon Press, Oxford (1965)

[Debray 90] M. E. Debray *et al.*, Phys. Rev. C **41** R1895 (1990)

[Debray 94] M. E. Debray *et al.*, Nucl. Phys. **A568** 141 (1994)

[De Shalit 74] A. De Shalit and H. Feshbach, *Theoretical Nuclear Physics Volume 1: Nuclear Structure*, John Wiley and Sons Inc., New York (1974)

[Dorso 86] C. O. Dorso, W. D. Myers and W. J. Swiatecki, Nucl. Phys. **A451** 189 (1986)

[Dragoun 69] O. Dragoun, H. C. Pauli, F. Schmutzler, Nucl. Data Tables A **6** 235 (1969)

[Dudek 79] J. Dudek, A. Majhofer, J. Skalski, T. Werner, S. Ćwiok and W. Nazarewicz, J. Phys. G. **5**, 1359 (1979)

[Dudek 81] J. Dudek, Z. Szymanski and T. Werner, Phys. Rev. C **23** 920 (1981)

[Egido 91] J. L. Egido and E. R. Robledo, Nucl. Phys. **A524** 65 (1991)

[Ennis 91] P. J. Ennis, C. L. Lister, W. Gelletly, H. G. Price, B. J. Varley, P. A. Butler, T. Hoare, S. Ćwiok and W. Nazarewicz, Nucl. Phys. **A535** 392; *erratum* ibid. **A560** 1079 (1991)

[Fernández-Niello 82] J. Fernández-Niello, H. Puchta, F. Riess and W. Trautmann, Nucl. Phys. **A391** 221 (1982)

[Fernández-Niello 91] J. Fernández-Niello, C. Mittag, F. Riess, E. Ruchowska and M. Stallknecht, Nucl. Phys. **A531** 164 (1991)

[Fogelberg 94] B. Fogelberg, M. Hellström, D. Jerrestam, H. Mach, J. Blomqvist, A. Kerek, L. O. Norlin and J. P. Omtvedt, Phys. Rev. Lett. **73** 2413 (1994)

[Fornal 94] B. Fornal *et al.*, Phys. Rev. C **49**, 2413 (1994)

[Freiesleben 84] H. Freiesleben and J.V. Kratz, Phys. Rep. **106**, 1 (1984)

[Galin 70] J. Galin, D. Guerreau, M. Lefort, J. Peter, X. Tarrango, and R. Basile, Nucl. Phys. **A159** 461 (1970)

[Gäggeler 86] H. Gäggeler *et al.*, Phys. Rev. C **33**, 1983 (1986)

[Gerl 89] J. Gerl, Ch. Ender, D. Habs, W. Korten, E. Schultz and D. Schwalm, Phys. Rev. C **39** 1145 (1989)

[Gerl 92] J. Gerl and R. M. Lieder, Euroball III. GSI Darmstadt report (1992)

[Grodzins 62] L. Grodzins, Phys. Lett. **2** 88 (1962)

[Haenni 77] D. R. Haenni and T. T. Sugihara, Phys. Rev. C **16** 120 (1977)

[Hager 68] R. S. Hager and E. C. Seltzer, Nucl. Data Tables A**4** 1 (1968); A**4** 397 (1968)

[Hager 69] R. S. Hager and E. C. Seltzer, Nucl. Data Tables A**6** 1 (1969)

[Hanappe 74] F. Hanappe, M. Lefort, C. Ngô, J. Peter and B. Tamain, Phys. Rev. Lett **32** 738 (1974)

[Harris 65] S. M. Harris, Phys. Rev. B **138** 509 (1965)

[Hill 53] D. L. Hill and J. A. Wheeler, Phys. Rev **89** 1102 (1953)

[Hofer 93] D. Hofer *et al.*, Nucl. Phys. **A551** 173 (1993)

[Horen 93] D. J. Horen *et al.*, Phys. Rev. C **48** R2131 (1993)

[Hughes 90] J. R. Hughes *et al.*, Nucl. Phys. **A512** 275 (1990)

[Inglis 54] D. R. Inglis, Phys. Rev. **96** 1059 (1954)

[Inglis 56] D. R. Inglis, Phys. Rev. **103** 1786 (1956)

[Kaufmann 59] R. Kaufmann and R. Wolfgang, Phys. Rev. Lett. **3** 232 (1959)

[Krane 88] K. S. Krane, *Introductory Nuclear Physics*, John Wiley and Sons, New York (1988)

[Kratz 74] J. V. Kratz, A. E. Norris and G. T. Seaborg, Phys. Rev. Lett. **33** 502 (1974)

[Królas 94] W. Królas *et al.*, Acta Phys. Pol. **B25**, 687 (1994)

[Kulessa 89] R. Kulessa *et al.*, Z. Phys. **A334** 299 (1989)

[Kurcewicz 76] W. Kurcewicz, N. Kaffrell, N. Trautmann, A. Płochocki, J. Żylicz, K. Stryczniewicz and I. Yutlandov, Nucl. Phys. **A270**, 175 (1976)

[Kurcewicz 87] W. Kurcewicz, E. Ruchowska, P. Hill, N. Kaffrell, G. Nyman, Nucl. Phys. **A464**, 1 (1987)

[Leander 82] G. A. Leander, R. K. Sheline, P. Möller, P. Olanders, I. Ragnarsson and A. J. Sierk, Nucl. Phys. **A388** 452 (1982)

[Leander 84] G. A. Leander and R. K. Sheline, Nucl. Phys. **A413** 375 (1984)

[Leander 86] G. A. Leander, W. Nazarewicz, G. F. Bertsch and J. Dudek, Nucl. Phys. **A453** 58 (1986)

[Lee 90] I. Y. Lee, Nucl. Phys. **A520** 641c (1990)

[Macchiavelli 94] A. O. Macchiavelli, I. Y. Lee, B. Cederwall, R. M. Clark, M. A. Delaplanque, R. M. Diamond, P. Fallon and F. S. Stephens, Proceedings of Conference on Physics from Large γ-ray Detector Arrays, Berkeley LBL35687, CONF 940888, UC 413.Page 149 (1994)

[Marten-Tölle 90] M. Marten-Tölle *et al.*, Z. Phys. **A336** 27 (1990)

[Mayer 94] R. H. Mayer *et al.*, Phys. Lett. B **336**, 308 (1994)

[McPherson 92] G. M. McPherson *et al.*, IEEE Trans. Nucl. Sci. **39** 886 (1992)

[Möller 81] P. Möller and J. R. Nix, Nucl. Phys. **A361** 117 (1981)

[Moretto 81] L. G. Moretto and R. P. Schmitt, Rep. Prog. Phys. **44** 533 (1981)

[Myers 69] W. D. Myers and W. J. Swiatecki, Ann. Phys. (N.Y) **55** 395 (1969)

[Nazarewicz 84] W. Nazarewicz, P. Olanders, I. Ragnarsson, J. Dudek, G. A. Leander, P. Möller and E. Ruchowska, Nucl. Phys. **A429** 269 (1984)

[Nazarewicz 85] W. Nazarewicz and P. Olanders, Nucl. Phys. **A441** 420 (1985)

[Nazarewicz 87] W. Nazarewicz, G. A. Leander and J. Dudek, Nucl. Phys. **A467** 437 (1987)

[Nazarewicz 87a] W. Nazarewicz, Proc. of the Internat. Conf. on Nucl. Structure through Static and Dynamic Moments, Melbourne (1987) ed. H. H. Bolotin, (Conf. Proc. Press Melbourne 1987) p. 180

[NDS] Nuclear Data Sheets, Produced by The National Nuclear Data Center, edited by M. J. Martin and J. K. Tuli, Academic Press, New York and London

[NDS 81] Nuclear Data Sheets, Produced by The National Nuclear Data Center, edited by M. J. Martin and J. K. Tuli, Academic Press, New York and London, Volume **33**, Number 2 (1981)

[Neergård 70] K. Neergård and P. Vogel, Nucl. Phys. **A145** 420 (1970)

[Neergård 70a] K. Neergård and P. Vogel, Nucl. Phys. **A149** 209 (1970)

[Neergård 70b] K. Neergård and P. Vogel, Nucl. Phys. **A149** 217 (1970)

[Nolan 85] P. J. Nolan, D. W. Gifford and P. J. Twin, Nucl. Inst. Meth. In Phys. Res. A **236** 95 (1985)

[Nolan 90] P. J. Nolan, Nucl. Phys. **A520** 657c (1990)

[Nolan 95] P. J. Nolan, F. A. Beck and D. B. Fossan, Annu. Rev. Nucl. Part. Sci. **45** 561 (1994)

[Phillips 86] W. R. Phillips, I. Ahmad, H. Emling, R. Holzmann, R. V. F. Janssens, T. L. Khoo and M. W. Drigert, Phys. Rev. Lett. **57** 3257 (1986)

[Poynter 89a] R. J. Poynter *et al.*, Phys. Lett. B **232** 447 (1989)

[Poynter 89b] R. J. Poynter, P. A. Butler, G. D. Jones, R. J. Tanner, C. A. White, J. R. Hughes, S. M. Mullins, R. Wadsworth, D. L. Watson and J. Simpson, J. Phys. G. **15**, 449 (1989)

[Radford 95] D. C. Radford, Nucl. Inst. Methods Phys. Res., Sect. A **361** 306 (1995)

[Raman 87] S. Raman, C. H. Malarkey, W. T. Milner, C. W. Nestor Jr. and P. H. Stelson, At. Data Nucl. Data Tables **36**, 1 (1987)

[Raman 91] S. Raman, C. W. Nestor Jr., S. Kahane, K. H. Blatt, Phys. Rev. C **43** 556 (1991)

[Reus 83] U. Reus and W. Westmeier, At. Data Nucl. Data Tables **29**, 1 (1983)

[Ring 80] P. Ring and P. Schuck, *The Nuclear Many-body Problem*, Springer-Verlag (1980)

[Robledo 87] L. M. Robledo, J. L. Egido, J. F. Berger and M. Girod, Phys. Lett. B **187** 223 (1987)

[Rohoziński 88] S. G. Rohoziński, Rep. Prog. Phys. **51** 541 (1988)

[Rösel 78] F. Rösel, H. M. Fries, K. Alder and H. C. Pauli, At. Data Nucl. Data Tables **21** 91 (1978)

[Roy 94] N. Roy, D. J. Decman, H. Kluge, K. H. Maier, A. Maj, C. Mittag, J. Fernández-Niello, H. Puchta and F. Riess, Nucl. Phys. **A462** 379 (1984)

[Ruchowska 82] E. Ruchowska, W. Kurcewicz, N. Kaffrell, T. Bjornstad, G. Nyman, Nucl. Phys. **383**, 1 (1982)

[Ruchowska 92] E. Ruchowska, J. Żylicz, C. F. Liang, P. Paris and Ch. Briancon, J. Phys. G. **18**, 131 (1992)

[Rudolf 79] G. Rudolf, A. Gobbi, H. Stelzer, U. Lynen, A. Olmi, H. Sann, R. G. Stokstad and D. Pelte, Nucl. Phys. **A330** 243 (1979)

[Schulz 91] N. Schulz *et al.*, Z. Phys. A **339** 325 (1991)

[Sheline 87] R. K. Sheline, Phys. Lett. B **197** 500 (1987)

[Sliv 65] L. A. Sliv and I. M. Band, *Alpha-, Beta- and Gamma-ray Spectroscopy* (ed. K. Siegbahn) p.1639 North-Holland, Amsterdam (1965)

[Smith 95] J. F. Smith *et al.*, Phys. Rev. Lett. **75** 1050 (1995)

[Smith 95a] J. F. Smith. Ph. D. thesis, University of Liverpool (1995)

[Spear 90] R. H. Spear and W. N. Catford, Phys. Rev. C **41** R1351 (1990)

[Stephens 54] F. S. Stephens Jr., F. Asaro and I. Perlman, Phys. Rev. **96** 1568 (1954)

[Stephens 55] F. S. Stephens Jr., F. Asaro and I. Perlman, Phys. Rev. **100** 1543 (1955)

[Strutinsky 56] V. M. Strutinsky, Atomnaya Energiya **1** 50 (1956); J. Nucl. Energy **1** 611 (1956)

[Strutinsky 67] V. M. Strutinsky, Nucl. Phys. **A95** 420 (1967)

[Sujkowski 77] Z. Sujkowski, D. Chmielewska, M. J. A. De Voigt, J. F. W. Jansen and O. Scholten, Nucl. Phys. **A291** 365 (1977)

[Takai 88] H. Takai *et al.*, Phys. Rev. C **38**, 1247 (1988)

[Trusov 72] V. F. Trusov, Nucl. Data Tables **10** 477 (1972)

[Urban 87] W. Urban, R. M. Lieder, W. Gast, G. Hebbinghaus, A. Krämer-Flecken, K. P. Blume and H. Hübel, Phys. Lett. B **185** 331 (1987)

[Urban 96] W. Urban *et al.*, submitted to Nucl. Phys. **A**

[Vogel 68] P. Vogel, Nucl. Phys. **A112** 583 (1968)

[Ward 83] D. Ward, G. D. Dracoulis, J. R. Leigh, R. J. Charity, D. J. Hinde and J. O. Newton, Nucl. Phys. **A406** 591 (1983)

[White 87] D. H. White *et al.*, Phys. Rev. C **35** 81 (1987)

[Wieland 92a] M. Wieland *et al.*, Phys. Rev. C **45** 1035 (1992)

[Wieland 92b] M. Wieland *et al.*, Phys. Rev. C **46** 2628 (1992)

[Wolf 74] K. L. Wolf, J. P. Unik, J. R. Huizenga, J. R. Birkelund, H. Freiesleben and V. E. Viola, Phys. Rev. Lett. **33** 1105 (1974)

[Wollersheim 93] H. J. Wollersheim *et al.*, Nucl. Phys. **A556** 261 (1993)

[Wu 87] C.Y. Wu *et al.*, Phys. Lett. B **188**, 25 (1987)

[Zhu 95] S. J. Zhu *et al.*, Phys. Lett. B **357** 273 (1995)